Bioactive Hydrophobic Components from Hericium erinaceus Fruiting Body and Their Mechanism of Anti-inflammatory and Neuroprotective Activities

阮, 暘

Bioactive Hydrophobic Components from *Hericium erinaceus* Fruiting Body and Their Mechanism of Anti-inflammatory and Neuroprotective Activities

RUAN YANG

Graduate School of Bioresource and Bioenvironmental Sciences

Kyushu University

2024

九州大学
KYUSHU UNIVERSITY

Graduate School of Bioresource and Bioenvironmental Sciences

This is to certify that this is the original Ph.D. thesis of Mr. **RUAN YANG.**

Thesis Title:

"Bioactive Hydrophobic Components from *Hericium erinaceus* Fruiting Body and Their Mechanism of Anti-inflammatory and Neuroprotective Activities"

Associate Prof. Kuniyoshi Shimizu

Prof. Atsushi Kume

Prof. Yuji Tsutsumi

Dean of the faculty

Prof. Miki Nakao

The Ph.D. Thesis “Bioactive Hydrophobic Components from *Hericium erinaceus* Fruiting Body and Their Mechanism of Anti-inflammatory and Neuroprotective Activities” by RUAN YANG has been examined on July 29th, 2024 and the revision has been approved by the following Examination Committee:

Kuniyoshi SHIMIZU

Associate Professor, Chair

Atsushi KUME

Professor

Yuji TSUTSUMI

Professor

FRONTISPIECE

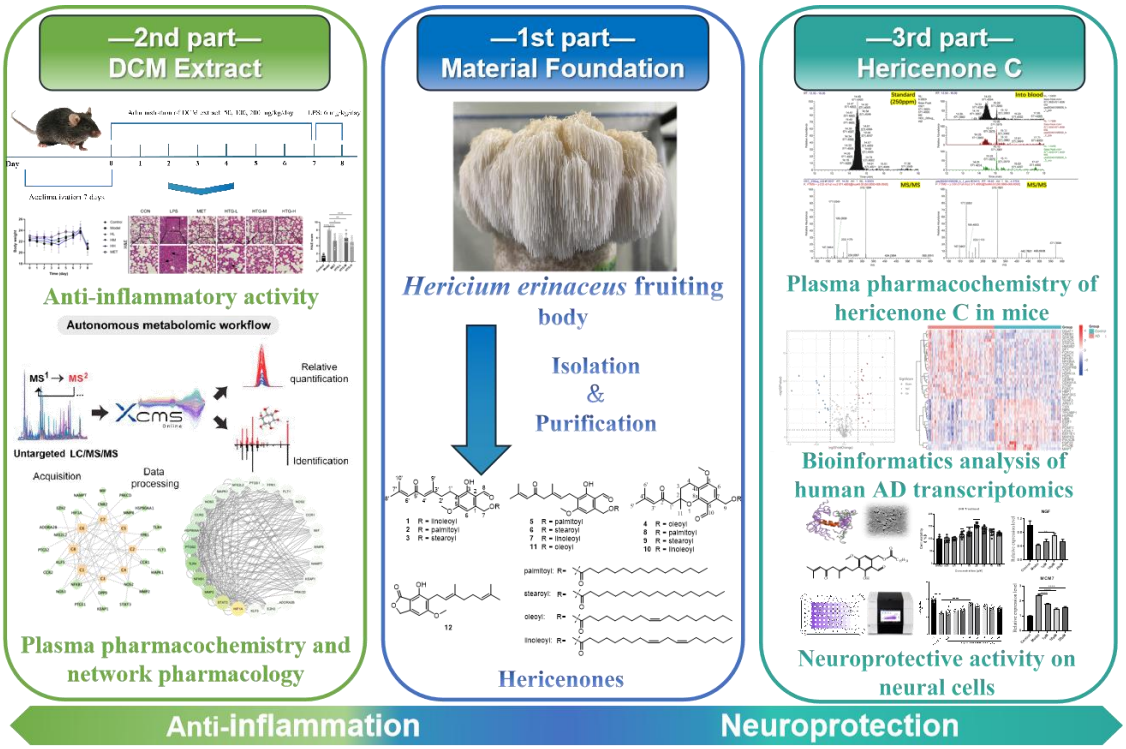

By studying the hydrophobic components of *H. erinaceus* at different material levels, combined with various analytical methods and pharmacological models, a scientific basis was provided for the functional food and pharmaceutical candidate for anti-inflammation and neuroprotection.

DECLARATION AND COPYRIGHT

I, Ruan Yang, declare that this thesis is my original work and that it has not been presented and will not be presented to any other university for a similar or any other degree award.

Signature:_____ Date: _____

ACKNOWLEDGMENTS

Throughout my pursuit of a Ph.D., I have received tremendous support and encouragement from numerous individuals whose assistance has had a profound impact on my academic career. I would like to express my sincere gratitude to these individuals.

First and foremost, I would like to sincerely thank my supervisor, **Assoc. Prof. Kuniyoshi Shimizu.** My supervisor not only provided me with meticulous guidance and support in academic matters but also offered me selfless care and encouragement in my personal life. My supervisor's conscientious guidance and rigorous academic attitude have deeply influenced me, and I have benefited greatly. I would also like to express my gratitude to **Prof. Atsushi Kume**for for his support and assistance in my research work. Under his careful guidance, I was able to delve deeply into my research topic and achieve significant research results. Their valuable advice and profound insights played a crucial role in the development and refinement of my thesis.

Furthermore, I want to thank my colleagues in the laboratory, such as **Dr. Wang Dongmei, Dr. Han Chunguang**, **Dr. Wang Duanyang,** and **Dr. Yhiya Amen**. They provided me with a conducive academic environment and collaborative opportunities, enabling me to conduct research in a positive and supportive atmosphere. Their guidance and suggestions have had a positive impact on my research work.

I would also like to express my gratitude to **Dr. Lv Weichao** and **Dr. Ren Guoqing**, visiting scholars from China Pharmaceutical University. They not only provided me with a lot of support and assistance in my research but also showed great care in my daily life. I would also like to thank their supervisor, **Prof. Zhang Chaofeng**, who accepted me as an exchange student in her research group, provided sufficient support

and guidance, and gave me a great deal of research motivation.

I also want to express my gratitude to my **family**, especially **my parents**, who have selflessly supported and encouraged me throughout my academic journey. Without their support, I would not have been able to successfully complete my studies. Their understanding and support have been my strong pillar of support.

Finally, I want to thank **all the teachers**, **laboratory colleagues**, and **friends** who have provided me with help and support throughout my academic career. It is due to your support and encouragement that I have been able to successfully complete my doctoral studies. Your friendship and assistance will forever be etched in my heart.

Thank you all!

ABSTRACT

Background: This study focuses on the medicinal and edible mushroom - *Hericium erinaceus*, a well-known species in China and Japan widely utilized in the food industry. Many hydrophobic components in natural products have excellent biological activity (such as flavonoids) and can easily cross biofilms to play a role (such as the blood-brain barrier). However, current bioactivity research on *H. erinaceus* primarily concentrates on hydrophilic components, with limited studies on hydrophobic and unique components such as hericenones.

Object: This research aims to isolate hydrophobic components, establish a different level of research material perspectives (extract and compound), investigate their traditional activities (anti-inflammatory and neuroprotective), and uncover their potential mechanisms through data mining and pharmacology research.

Method and Result: The first part focused on isolation. Dichloromethane (DCM) was used to extract *H. erinaceus* to obtain *H. erinaceus* DCM extract (HEDE), and the HEDE was separated and purified by column chromatography to obtain hericenones. Due to the most abundance of hericenone C in hericenone derivative, we have decided to pursue further research with hericenone C. This step laid the material foundation for subsequent activity experiments. The second part studied the metabolomics of components ingested into the blood in mice. We administered HEDE and hericenone C intragastrically to mice, collected blood, and performed the metabolomic analysis of plasma using Liquid Chromatograph Mass Spectrometer (LC/MS), we found some compounds in HEDE with a high abundance that can enter the bloodstream, and hericenone C can enter the bloodstream in its original form. These findings provide a basis for exploring the active ingredients of HEDE in vivo and for oral use of

hericenone C for therapeutic purposes. The third part evaluated the anti-inflammatory activity of the HEDE using lipopolysaccharide (LPS)-induced mice model of Acute lung injury (ALI). ALI results from both local and systemic inflammatory responses, and is also one of the serious complications of Corona Virus Disease 2019 (COVID-19)'s high morbidity and mortality, over the past few years, COVID-19 has caused widespread impact around the world. Pretreatment of HEDE demonstrated potent anti-inflammatory activity to LPS-induced ALI in this study. Metabolomic analysis in part 2 combined with network pharmacology, we found that HEDE can potentially ameliorate the inflammation of ALI through the TLR4/NFKB1/STAT3/HIF-1a pathway. This provides the basis for the potential functional food development of HEDE. Finally, by establishing an Amyloid beta-peptide 25-35 ($A\beta_{25-35}$)-induced Alzheimer's Disease (AD) cell model, we found that hericenone C can improve $A\beta_{25-35}$-induced human neuroblastoma cell (SH-SY5Y) death. Aging is the top risk related to AD and telomeres are closely related to aging. Past research has shown that hericenone C has the activity of promoting nerve growth factor synthesis in vitro and a mixture rich in hericenone C can improve cognition in aging animals. Therefore, we conducted bioinformatics studies on telomere aging based on the transcriptomics of human AD patients and found through molecular biological methods that hericenone C can play a neuroprotective role through the telomere aging-related targets and pathway (NGF/TrkA/ERK/CREB) on $A\beta_{25-35}$-induced AD cell model. This part revealed the potential of hericenone C as a pharmaceutical candidate for AD.

Conclusion: This study offers new perspectives and scientific evidence for the development of *H. erinaceus* as a potential pharmaceutical or functional food. In

addition, the natural product development approach adopted in this study can effectively explore potential targets for natural product therapy through metabolomic analysis of components ingested into the blood after oral administration of natural products and bioinformatics analysis of publicly available transcriptomic data.

ACHIEVEMENTS

Published papers

1. **Ruan, Y.**, Han, C., Wang, D., Inoue, Y., Amen, Y., Othman, A., ... & Shimizu, K. (2023). New benzaldehyde derivatives from the fruiting bodies of *Hericium erinaceus* with cytotoxic activity. Natural Product Research, 1-10.
2. **Ruan, Y.**, Lv, W., Li, S., Cheng, Y., Wang, D., Zhang, C., & Shimizu, K. (2023). Identification of telomere-related genes associated with aging-related molecular clusters and the construction of a diagnostic model in Alzheimer's disease based on a bioinformatic analysis. Computers in Biology and Medicine, 159, 106922.
3. **Yang Ruan***, Guoqing Ren*, Weichao Lv, Mingchun Wang, Renshi Li, Kuniyoshi Shimizu#, Chaofeng Zhang#. (2024). The Dual Role of 20(S)-protopanaxadiol in Alleviating Pulmonary Fibrosis through the Gut-Lung Axis. phytomedicine. 155699.
4. 謝佳弘弋, 阮暘, 松本雅子, 永田真紀, 清水邦義*. (2023). ヤマブシタケ(*Hericium erinaceus*)の神経保護活性の研究. 機能性食品と薬理栄養, 17-1.
5. Tamrakar, S., Wang, D., Hiraki, E., Han, C., **Ruan, Y.**, Allam, A. E., ... & Shimizu, K. (2023). Deacylated Derivative of Hericenone C Treated by Lipase Shows Enhanced Neuroprotective Properties Compared to Its Parent Compound. Molecules, 28(11), 4549.
6. Weichao Lv, Hongcai Mao, **Yang Ruan**, Shuaiyu Li, Kuniyoshi Shimizu, Renshi Li*, Chaofeng Zhang*. (2023). Identification and immunological characterization of PLA2G2A and cell death-associated molecular clusters in idiopathic pulmonary fibrosis. Life Sciences, 331, 122071.

7. Li, S., **Ruan, Y.**, Long, C., & Cheng, Y. (2023, December). Efficient CNN-LSTM Based Parameter Estimation of Lévy Driven Stochastic Differential Equations. In 2023 International Conference on Machine Learning and Applications (ICMLA) (pp. 316-323). IEEE.

Conferences

1. **Yang Ruan**, Chunguang Han, Dongmei Wang, Yuka Inoue, Yhiya Amen, Ahmed Othman, Yanisa Mittraphab, Maki Nagata, Kuniyoshi Shimizu. New benzaldehyde derivatives from the fruiting bodies of *Hericium erinaceus* with cytotoxic activity. The 73rd Annual Meeting of the Japan Wood Research Society, March 2023 (Oral Speaker).
2. **Yang Ruan**, Weichao Lv, Shuaiyu Li, Yuzhong Cheng, Duanyang Wang, Chaofeng Zhang, Kuniyoshi Shimizu. Hericenone C isolated from the fruiting body of Hericium erinaceus with neuroprotective effects - telomere genes associated with the Alzheimer's disease aging cluster based on bioinformatics screening. The l8th Asian Natural Product Conference, January 2024 (Oral Speaker)

TABLE OF CONTENT

LIST OF TABLES

LIST OF FIGURES

LIST OF APPENDICES

LIST OF ABBREVIATIONS

1D	*One dimension*
AD	*Alzheimer's disease*
ALI	*Acute lung injury*
ANNs	Artificial neural networks
AP-1	*Activator protein 1*
ARDEGs	Aging-related differentially expressed genes
ARDS	Acute respiratory distress syndrome
ARGs	Aging-related genes
ATCC	American Type Culture Collection
AUC	Area under the curve
Aβ	*Amyloid beta-peptide*
Aβ	Amyloid beta
BC	Betweenness centrality
BDNF	Brain-derived neurotrophic factor
BP	Biological process
BPC	Base peak chromatogram
CC	Cellular component
CC	Closeness centrality
$CDCl_3$	Deuterated chloroform
CDF	Cumulative distribution function
COSY	*^1H–^1H correlation spectroscopy*
COVID 19	*Corona Virus Disease 2019*

CREB	*cAMP-response element binding protein*
CREB	cAMP response element-binding protein
DC	Degree centrality
DCA	Decision curve analysis
DCM	*Dichloromethane*
DMEM	Dulbecco's Modified Eagle Medium
EC109	*Human Esophageal Cancer Cells*
ECL	Enhanced chemiluminescence
EP tube	Eppendorf tube
ERK	*Extracellular regulated protein kinases*
ERK	Extracellular signal-regulated kinase
FBS	Fetal Bovine Serum
GBM	Gradient boosting model
GC	Gas chromatography
GLM	Generalized linear model
H&E	Hematoxylin and eosin
H. erinaceus	*Hericium erinaceus*
HAGR	Human Ageing Genomic Resources
HEDE	*H. erinaceus DCM extract*
HEP	*H. erinaceus polysaccharides*
HIF-1α	*Hypoxia-inducible factor 1 alpha*
HL-60	*Leukemia Myeloid Cells*
HMBC	Heteronuclear multiple bond coherence

HMQC	*Heteronuclear multiple quantum coherence*
HPFC	*High-performance flash chromatography*
HPLC	*High-Performance Liquid Chromatography*
HR-ESI-MS	*High-resolution electrospray ionization mass spectrometry*
IL-1β	*Interleukin-1β*
IL-6	*Interleukin-6*
IR	*Infrared*
LC/MS	*Liquid Chromatograph Mass Spectrometer*
LPS	*Lipopolysaccharide*
MAPK	Mitogen-activated protein kinases
MET	Metformin
MF	Molecular function
MMP-9	*Matrix metalloproteinase-9*
MPLC	*Medium pressure liquid chromatography*
MS/MS	Tandem mass spectrometry
MSD	Mass selective detector
NF-κB	*Nuclear factor kappa B*
NF-κB1	*Nuclear factor of kappa light polypeptide gene enhancer in B-cells 1*
NGF	*Nerve growth factor*
NMR	*Nuclear Magnetic Resonance Imaging*
NO	*Nitric oxide*
Nrf2	*Nuclear factor erythroid 2-related factor 2*

NT3	Neurotrophin 3
NT4/5	Neurotrophin 4/5
OD	Optical density
p75NTR	p75 neurotrophin receptor
PAGE	Polyacrylamide gel electrophoresis
PGE2	*Prostaglandin E2*
PPI	Protein-protein interaction
RAW 264.7	*Mouse Monocyte Macrophage Leukemia Cells*
RF	Random forest
RMSE	Root mean square error
ROC	Receiver operating characteristic curve
SASP	Senescence-associated secretory phenotype
SH-SY5Y	*Human neuroblastoma cell*
STAT3	*Signal transducer and activator of transcription 3*
SVM	Support vector machine
TCM	*Traditional Chinese Medicine*
THAs	Targets of HEDE for treating ALI
TLR4	*Toll-like receptor 4*
TMS	Tetramethylsilane
TNF-α	*Tumor necrosis factor-α*
TOM	Topological overlap matrix
TRDEGs	Telomere-related differentially expressed genes
TRGs	Telomere-Related Genes

Trk	Tropomyosin-related kinase
TrkA	*Tyrosine kinase-A*
tSNE	t-distributed Stochastic Neighbor Embedding
UPLC	Ultra-performance liquid chromatography
UV	*Ultraviolet*
XIC	Extracted ion chromatogram

Chapter 1 Introduction and Background

1.1.Development and therapeutic potential of natural products

Natural products refer to chemical substances synthesized by living organisms, such as plants, animals, and microorganisms. These products often possess biological activity and play an important role in fields such as drug development, agriculture, and the food industry [1] . Natural products have been instrumental in the development of pharmaceuticals, serving as the foundation for the majority of ancient medicinal remedies throughout history [2] . They have been identified as a precious reservoir for the development of novel therapeutic agents aimed at combating a range of critical illnesses where effective solutions are still lacking or not yet accessible [3] . Despite their promise, the process of unearthing and cultivating drugs derived from natural sources has encountered significant obstacles. Challenges like the intricate architecture of these natural substances, the challenge of procuring substantial amounts, and the incompatibility of natural extracts with high-throughput screening processes have impeded their integration into contemporary pharmaceutical research [4,5] . Nevertheless, contemporary technological progress has sparked renewed interest in this sector. Novel approaches in the realms of molecular biology, chemical synthesis, and data mining have bolstered the efficiency and potency of uncovering medicinal compounds from natural origins [6,7] . The renewed focus on natural products is further motivated by the unfulfilled demands in the prevailing drug discovery frameworks. Moreover, the innate biological efficacy and wide variety of natural products provide a singular opportunity to identify novel molecular entities that possess superior therapeutic potential[3].

Functional foods, integrating nutritional elements and bioactive compounds, are pivotal in connecting the domains of nutrition and therapeutics. The integration is notably apparent in the notion of "medicinal foods," which leverage the curative attributes of

natural products [8]. The overlapping boundary between nutrition and medicine is a result of an enhanced awareness of how dietary choices affect health and an increasing market need for products that contribute to health and wellness. Natural products in functional foods encompass a broad spectrum, from plant-based phytonutrients to marine-sourced bioactives. For example, fucoidans, extracted from seaweed, demonstrate a multitude of beneficial biological activities such as antioxidant, anti-inflammatory, and antiviral capabilities, making them valuable components in the development of functional foods[9]. Equally, fungi are acknowledged for their nutritional richness and their array of bioactive characteristics, which underpin their classification as functional foods and providers of health-promoting nutrients[10].

1.2.Hydrophobic and hydrophilic natural products

In the study of natural products, hydrophilicity (water affinity) and hydrophobicity (water aversion) are two important concepts. Hydrophilic compounds are typically capable of interacting with water to form a uniform solution, while hydrophobic compounds tend to separate from water, forming distinct phases or droplets[11].

1.2.1.Hydrophobic compounds

Hydrophobic compounds are difficult to dissolve in aqueous solutions. They typically exhibit good solubility in organic solvents, such as alcohols, ketones, ethers, and so on. Their chemical structures often contain hydrophobic groups like hydrocarbon chains or aromatic rings, and they may have a small number of polar groups, but the overall structure is predominantly nonpolar [12] . The main types of chemical structures of hydrophobic natural products include terpenes, flavonoids, steroids.

1.2.1.1.Terpenoids

Terpenoids constitute are the largest class of natural products, known for their chemical structural diversity. They are formed by the polymerization of isoprene (C_5H_8) units, creating a variety of complex structures. Based on their chemical structure, terpenes can be divided into the following categories: monoterpenes, which are composed of two isoprene units and are commonly found in plant essential oils, such as limonene in lemon oil. Sesquiterpenes, composed of three isoprene units, are commonly found in spices and aromatic plants, such as sesquiterpenes in coriander oil. Diterpenes, composed of four isoprene units, are widely present in resins and certain vegetable oils. Triterpenes, composed of six isoprene units, are found in the waxy layers of many plants and certain medicinal plants. Tetraterpenes, composed of eight isoprene units, include pigments such as carotenoids[13–15].

1.2.1.2.Flavonoids

Flavonoids are natural substances synthesized in several parts of plants that exhibit a high antioxidant capacity [16] . They are natural products with various benzene ring structures, found in fruits, vegetables, grains, bark, roots, stems, flowers, tea, and wine. Their basic structure consists of two benzene rings and a pyran ring. Flavonoids can be further classified based on their chemical structure and substituent groups. Some are hydrophobic, while others are hydrophilic. The hydrophobic ones include flavones, such as quercetin, which have antioxidant and anti-inflammatory effects; isoflavones, primarily found in soybeans, with estrogen-like biological activity; and flavanones, such as naringin, mainly found in citrus plants[17,18].

1.2.1.3.Steroids

Steroids encompass plant sterols and steroid hormones, commonly found in plant cell

membranes[19]. Steroids play a crucial role in the body. They are not only key participants in biochemical reactions but also play an important role in cell signaling and gene expression. Plant steroids, for example, have antioxidant properties and anti-inflammatory effects, while animal steroids play a central role in reproduction and metabolism[20,21].

1.2.1.4.Fatty Acids

Fatty Acids, such as linoleic acid and oleic acid, are primarily derived from vegetable oils and have significant nutritional value [22] . Fatty acids are classified based on their degree of saturation: Saturated fatty acids have no double bonds in their carbon chains, and all carbon atoms are fully bonded with hydrogen atoms. Common saturated fatty acids include palmitic acid (C16) and stearic acid (C18). Unsaturated fatty acids contain one or more double bonds in their carbon chains. They can be further subdivided based on the number of double bonds. Monounsaturated fatty acids contain only one double bond, such as oleic acid (C18:1). Polyunsaturated fatty acids contain two or more double bonds, such as linoleic acid (C18:2) and linolenic acid (C18:3) [23] . Fatty acids currently play a pivotal role in regulating the fluidity of cell membranes in all cell types and are involved in complex processes of eukaryotic organisms, such as proliferation, differentiation, secretion, migration, invasion, and phagocytosis, highlighting the importance of these molecules in sustaining life[24].

1.2.2.Hydrophilic compounds

Hydrophilic natural products often contain polar functional groups such as hydroxyl (-OH), carboxyl (-COOH), amino ($-NH_2$), and carbonyl (C=O) groups. These groups facilitate strong interactions with water molecules through hydrogen bonding, making

the compounds more soluble in water [11] . Sugars, amino acids and their derivatives, saponins, alkaloids, phenolic acids, are all hydrophilic natural products.

1.2.2.1.Sugars

Sugars are categorized into three main types: monosaccharides, which are simple sugars with 3 to 7 carbon atoms, such as glucose, fructose, and galactose. They serve as the building blocks for more complex carbohydrates, connecting through glycosidic bonds[25]. Disaccharides are formed by the connection of two monosaccharide molecules through glycosidic bonds. Common disaccharides include sucrose (a combination of glucose and fructose), lactose (a combination of glucose and galactose), and maltose (a combination of two glucose molecules). Disaccharides are hydrolyzed into their constituent monosaccharides during the digestive process for energy utilization [26] . Polysaccharides are high molecular weight compounds formed by the connection of multiple monosaccharide units through glycosidic bonds. Polysaccharides are ideal natural resources for supplements and medicines and have been receiving increasing attention over the years. Different polysaccharides obtained from microorganisms, plants, and animals possess various properties, such as antioxidant, immunomodulatory, anti-inflammatory, anti-HIV, antimutagenic, antitumor, and anticoagulant activities [27–31] . The high molecular weight of bioactive polysaccharides is not conducive to penetrating multiple cellular membrane barriers within the body to exert pharmacological effects [32] . Conversely, if the molecular weight is too low, the polysaccharides will not exhibit any bioactivity. Therefore, methods for modifying the structure of polysaccharides are fundamental approaches to solving the aforementioned issues[33].

1.2.2.2.Amino acids

Amino acids have the same basic structure, which mainly includes the following parts: the alpha carbon is the central carbon atom of the amino acid, connected to three other groups. The amino group (-NH_2) gives it basicity. The carboxyl group (-COOH) allows the amino acid to release hydrogen ions in water, showing acidity. The vast majority of amino acids are hydrophilic and the side chain (R group) is the unique part of each amino acid, determining the properties and functions of the amino acid [34]. Derivatives like GABA, an inhibitory neurotransmitter, and glutamate, an excitatory one, are crucial for brain function. Lysine and arginine can form compounds like nitric oxide, affecting blood vessels and immunity, and their derivatives are in supplements to boost health[35].

1.2.2.3.Saponins

Saponins are structurally divided into two groups, triterpene saponins and steroid saponins [36]. Triterpene saponin aglycones include the α-amyrane (e.g. ursolic acid) [37], β-amyrane (e.g. oleanolic acid) [38] and lupane (e.g. betulinic acid) skeletons [39], or the tetracyclic dammarane backbone (e.g. ginsenoside Rb1) [40], linked with one to three carbohydrate chains containing up to six sugar or uronic acid molecules. While steroid saponins consist of two groups, corresponding to spirostanol (e.g., dioscin) and furostanol (e.g., protodioscin) aglycones[41]. Saponins function as defence compounds for plants and are pharmaceutically utilised by humans for their anti-thrombotic, anti-inflammatory, anti-cancer, anti-diabetic, and antihypertensive properties and for treating reproductive disorders[42–46].

1.2.2.4.Phenolic acids

Phenolic acids are aromatic acid compounds, with their basic structure including a phenolic ring and a carboxylic acid group. The phenolic ring has a conjugated double

bond system, which gives these compounds good chemical stability and bioactivity[47]. Most phenolic acids are highly water-soluble, which allows for efficient transport and storage within plants. For instance, caffeic acid and chlorogenic acid are well soluble in water and thus play a significant role in the biosynthesis and metabolic processes of plants. Caffeic acid is widely present in a variety of plants, including fruits, vegetables, herbs, and beverages. It is an important component of foods such as coffee, red wine, tea, and olive oil. Its antioxidant, anti-inflammatory, and potential antitumor effects make it a hot topic of research[48,49]. Chlorogenic acid is a natural compound with a broad range of health benefits, and its antioxidant and anti-inflammatory properties give it potential value in the prevention and treatment of various diseases[50].

1.3.Therapeutic applications of mushrooms

Mushrooms have been integral to oriental medicinal practices for many centuries, serving to combat and mitigate the effects of numerous illnesses. In contemporary times, the extracts from these fungi are becoming more accessible as dietary enhancements[51,52]. The bioactive compounds found in mushrooms are classified into hydrophilic and hydrophobic compounds and include polysaccharides, terpenoids, phenolics, and various other secondary metabolites, which exhibit antioxidant, anticancer, anti-inflammatory, and immunomodulatory activities[53]. Within this group of bioactive substances, hydrophilic compounds - polysaccharides, especially beta-glucans, have garnered significant attention for their ability to bolster immune responses. Research indicates that these complex sugars can regulate immune function by stimulating the activity of macrophages, natural killer cells, and T-cells, which in turn, strengthens the immune system's capability to combat infections and resist tumor development[54]. Mushrooms possess notable antioxidant characteristics. Ingredients such as

ergothioneine and glutathione, which are found within these fungi, function as powerful antioxidants that reduce oxidative stress, a critical element in the aging process, and numerous chronic illnesses [55]. Moreover, the anti-inflammatory benefits of mushrooms are linked to their hydrophobic bioactive constituents, including triterpenes and flavonoids, which can suppress inflammation by moderating the production of inflammatory cytokines [56]. Furthermore, specific mushroom varieties such as *Agaricus blazei* and *Ganoderma lucidum* have been the subject of anticancer research. Evidence from studies suggests that the bioactive components present in these mushrooms can suppress the proliferation of tumors and trigger programmed cell death in cancerous cells [57]. Blending such naturally occurring substances within foods designed for health benefits and within medical formulations represents a sustainable method to elevate human health and battle diverse conditions.

1.4.Current research in *Hericium erinaceus* fruiting body

Hericium erinaceus, recognized as "Houtou" or "Shishigashira" in Chinese and "Yamabushitake" in Japanese, is frequently recommended in Traditional Chinese Medicine (TCM) because of its beneficial impact on health (Figure 1). This particular species is widespread across the northern latitudes of Europe, Asia, and North America[58,59]. *H. erinaceus* is esteemed as a significant medicinal fungus, with numerous of its bioactivities being reported. Especially its neuroprotective activity and immunomodulatory activity.

Figure 1. *Hericium erinaceus* cultivated in our laboratory.

1.4.1.Biological activities

1.4.1.1.Neuroprotective activities

NGF stimulates neuronal proliferation and are instrumental in preventing neuronal apoptosis, thereby playing an essential role in sustaining neuronal health[60]. Dysfunction of NGF has been linked to the development of AD as well as other neurodegenerative conditions, underscoring the therapeutic potential of NGF-targeted strategies in related-treatment[61,62]. Past studies have shown that hericenones C−E have neurotrophic properties that stimulate NGF synthesis[63]. Compounds in *H. erinaceus* fruiting body, hericenones compounds is a major factor in promoting NGF synthesis. Stimulation of NGF synthesis is the primary and traditional approach to assess neurotrophic and protective effects.

Moreover, contemporary research into *H. erinaceus* has demonstrated that the dietary provision of hericenones-rich extract to aging mice for a duration of two months effectively reversed the age-related deterioration of recognition memory [64] and mitigated the alleviated reduced locomotor activity in weakened mice [65]. In addition, a primordium of *H. erinaceus* contains ergothioneine and hericenes, but lacks erinacines, offering benefits to neuroprotection and aging prevention [66]. The structure of hericenes are close to hericenones, and recent studies have shown that hericene A can stimulate a broad neurotrophic pathway in the central hippocampal neurons, culminating in the activation of the ERK1/2 signaling pathway and the enhancement of spatial memory [67]. This implies that this class of compounds may have the potential for neuroprotective activity.

1.4.1.2.Immunomodulatory activities

The research on *H. erinaceus*'s immunomodulatory effects has primarily concentrated on its polysaccharides. To date, an extensive array of studies has confirmed that these polysaccharides exhibit immunomodulatory activities, such as anti-inflammatory properties. They have the capacity to modulate macrophages [68–71], ameliorate immunosuppression [72–74], anti-inflammation [75,76], and repair damaged intestinal mucosal immunity [77].

In addition to that, ethanol extracts of *H. erinaceus* fruiting body have demonstrated potent anti-inflammatory properties in a dextran sulfate sodium-induced ulcerative colitis mouse model, reducing inflammation in the gut by inhibiting the generation of inflammatory factors, including tumor necrosis factor-α (TNF-α), Interleukin-1β (IL-1β), and Interleukin-6 (IL-6) [78]. Hericenone E can regulate the LPS-induced inflammatory

response by controlling the activation of nuclear factor kappa B (NF-κB) and activator protein 1 (AP-1), which in turn leads to a decrease in the generation of nitric oxide (NO) and prostaglandin E2 (PGE2)[79]. Hericene A and hericenone F, have been demonstrated to suppress the production of pro-inflammatory mediators (TNF-α, IL-6, and NO) in murine RAW 264.7 macrophage cells[80]. Moreover, it was found that a 2-month oral supplement of *H. erinaceus* extract could significantly change the relative abundance of gut microbiota involved in cognition and inflammation, thereby producing immunomodulatory effects in the hippocampus of mice through gut-brain axis[81].

1.4.1.3.Antioxidant activities

A newly identified polysaccharide component exhibits potent DPPH-radical scavenging activity, with a maximum scavenging rate that can reach up to 91.72%±0.17%, which is essentially comparable to the scavenging capacity of Vitamin C[82]. Han *et al.* reported that administered to mice at a dosage of 300 mg/kg for 15 days via gavage of *H. erinaceus* polysaccharides (HEP), significantly reduced the level of lipid peroxidation and increased the activity of antioxidant enzymes in the experimental animals compared to the renal ischemia-reperfusion group[83]. Additionally, the ethanol extract of *H. erinaceus* may exert antiangiogenic and antioxidant effects by modulating the MMP-9/NF-κB and Nrf2-antioxidant signaling pathways[84].

1.4.1.4.Other biological activities

Hou *et al.* reported polysaccharides of *H. erinaceus* fruiting body induce apoptosis in human colorectal cancer cells[85]. Hericenone I has cytotoxic activity against the EC109 cell line[86]. Hericerin A and hericerin could induce apoptosis in HL-60 cells[87], and hericerin inhibited pollen growth[88]. Hericenone B has been found to stimulate the

release of arachidonic acid in the body, inhibiting platelet aggregation[89]. *H. erinaceus* extracts have also demonstrated inhibitory activity against various pathogenic bacteria[90] and *Salmonella typhimurium*[91]. Measurement of inhibition of α-glucosidase activity is the main method used to evaluate antihyperglycemic activity in vitro, erinacerins have shown inhibitory activity against α-glucosidase[92–95].

1.4.2.Target compounds - Hericenones

Through the aforementioned content, we can observe that hericenones exhibit good effects on the important bioactivities of *H. erinaceus*, such as neurotrophic activity and anti-inflammatory activity. However, research on the related mechanisms is very scarce. Hericenones often have a structure with long-chain fatty acids, making them primarily hydrophobic compounds. At the same time, current research on the fruiting bodies of *H. erinaceus* has largely focused on hydrophilic compounds and extracts, like polysaccharides, but hydrophobic compounds also possess very important bioactivities. We will focus on the study of hericenones, and the following are related literature on hericenones.

Hericenones A and B, identified as the isobenzofuranone and isoindoline-1-one alkaloid respectively, originated from *H. erinaceus* and were first isolated in the year 1990 by Kawagishi *et al.*[96]. In 1991, they isolated the novel compounds from *H. erinaceus*, hericenones C-E, which are recognized for their capacity to stimulate NGF synthesis[63]. Building on their previous work, they further isolated hericenone F-H in 1992, demonstrating comparable stimulating effects on NGF synthesis[97]. Hericenone I was isolated by MA *et al.*[98] with cytotoxic activity against the EC109 cell line. 3-hydroxyhericenone F isolated and showed protective effects against endoplasmic reticulum (ER) stress-induced cell death in neuro2a cells, whereas hericenone J, isolated

concurrently, did not demonstrate this protective activity[99]. Subsequently, the isomer of hericenone J, known as isohericenone J, was isolated [87] . Hericenone K was obtained from the fruiting bodies of *H. erinaceus* by Zhang *et al.* [100] and hericenone O-R were first reported in this thesis[101]. All the structures of hericenones are shown in Figure 2.

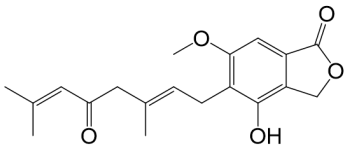

Hericenone A

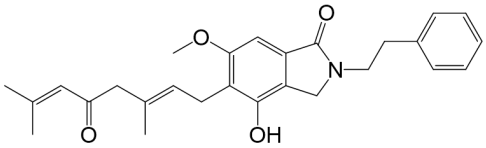

Hericenone B

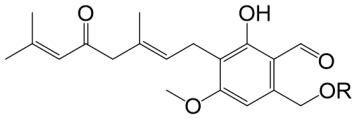

Hericenone C R = palmitoyl
Hericenone D R = stearoyl
Hericenone E R = linoleoyl
Hericenone I R = oleoyl

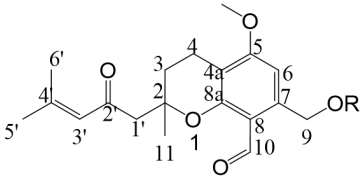

Hericenone R R = oleoyl
Hericenone F R = palmitoyl
Hericenone G R = stearoyl
Hericenone H R = linoleoyl

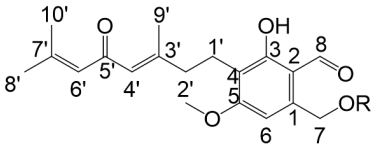

Hericenone O R = linoleoyl
Hericenone P R = palmitoyl
Hericenone Q R = stearoyl

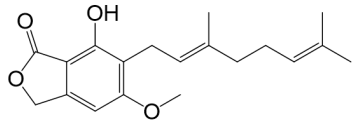

Hericenone J

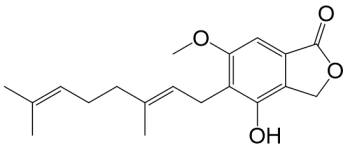

Isohericenone J

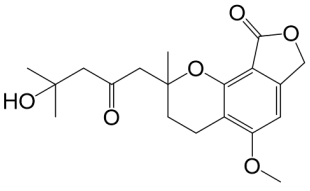

Hericenone K

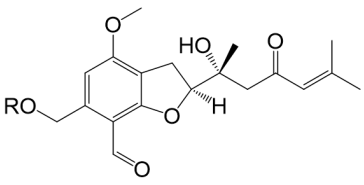

Hericenone Z R=palmitoyl

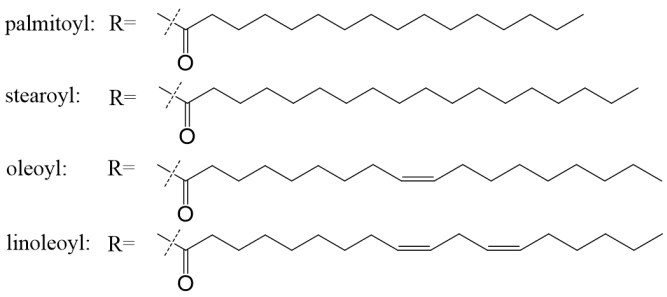

Figure 2. The chemical structures of hericenones from *H. erinaceus* fruiting body.

1.5.Aim of the study

With the increasing research on the compounds of *H. erinaceus* in recent years, scientists have obtained a large number of compounds from the fruiting body of *H. erinaceus*. *H. erinaceus* is widely recognized for its cognitive-enhancing properties. Hericenones, a class of hydrophobic compounds with long-chain fatty acids found in the fruiting bodies of *H. erinaceus*, have garnered significant attention in the scientific community due to their potential cognitive-enhancing properties. This species of mushroom has been traditionally used in various cultures for its health benefits, and modern research is beginning to uncover the complex biochemistry that underpins these traditional uses. Despite these promising findings, the study of hericenones is still in its infancy, and much remains to be learned about their bioactivity mechanisms.

Among them, hericenone C, which has the highest content in its derivatives, has been reported to promote the synthesis of NGF in vitro [63]. Extract containing hericenones C and D have been shown to mitigate cognitive decline in aging mice[65]. And hericene A, a structurally similar compound to hericenones, exhibits neurotrophic activity via the ERK1/2 pathway [67]. This indicates the significant potential for research on hericenones.

In summary, the study of the bioactivity mechanisms of hericenones, which have important bioactivities such as neurotrophic and anti-inflammatory effects, is still insufficient and not in-depth. These shortcomings have limited the further development and application of the fruiting bodies of *H. erinaceus*. To explore the application of *H. erinaceus* fruiting body as functional food and pharmaceutical candidates, this study focuses on the bioactivities of hydrophobic extract. The research flow is shown in Figure 3.

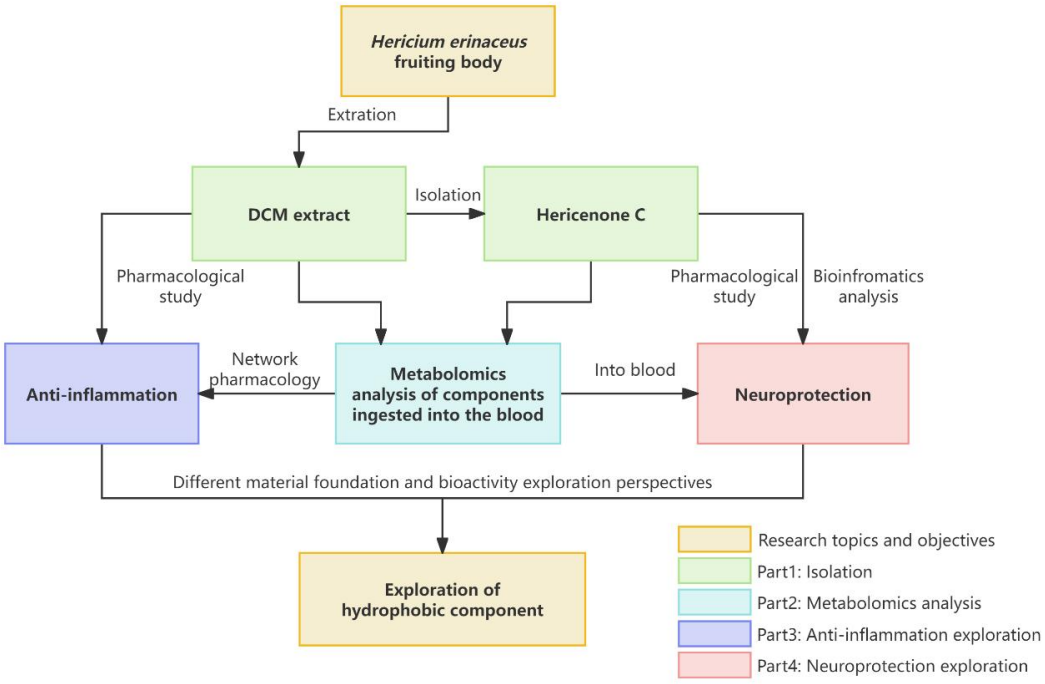

Figure 3. Scheme of the research flow.

First, we need to isolate this class of compounds from *H. erinaceus*, as most of the compounds unique in *H. erinaceus*, including hericenone C, are not commercially available. This means that to determine the bioactivity of hericenone C, we need to extract, isolate, and identify it from the fruiting body of *H. erinaceus*. During this process, we can summarize known compounds and potentially discover new ones. Therefore, in the first part, we used DCM as the extraction solvent to extract hydrophobic components. We utilized liquid chromatography, MS, and NMR to isolate and identify hericenones.

Secondly, to understand the components in HEDE that can enter the bloodstream and whether hericenone C can be transported in the blood, we established three groups of mice: a control group, an HEDE group, and a hericenone C group. The latter two groups underwent gavage administration of HEDE and hericenone C respectively for seven consecutive days. Plasma samples were collected for analysis two hours after the final gavage on the last day. Given that the active mechanisms of extracts are generally challenging to study, we used LC/MS-based non-targeted metabolomics to analyze high-abundance compounds entering the plasma from HEDE by comparing them to the database. Then, combined with network pharmacology and molecular biology methods, we can predict and verify potential mechanisms. Also, targeted metabolomics analysis of the plasma samples following hericenone C gavage can help determine whether hericenone C can enter the blood in an unmetabolized form.

In recent years, COVID-19 has had a significant global impact, leading to increased attention on lung protection. Therefore, we established an LPS-induced ALI mouse model following a seven-day gavage pretreatment of HEDE. Combining the results of metabolomics analysis with network pharmacology and molecular biology methods, our

aim is to explore the mechanism by which HEDE prevents or ameliorates LPS-induced acute lung inflammation in mice. This aligns with the concept of functional foods—prevention rather than treatment—and offers a new perspective on developing the hydrophobic components of *H. erinaceus* as functional foods for lung protection.

Finally, we investigated the neurotrophic activity of hericenone C and its mechanism in improving cognitive decline caused by aging. We first established an $A\beta_{25-35}$-induced AD cell model and found that hericenone C could ameliorate neuronal cell death. Given the close relationship between aging and telomeres, we hypothesize that hericenone C may exert neuroprotective effects by influencing telomere aging-related targets and pathways. To identify telomere aging targets associated with AD, we utilized transcriptome data from AD patients to analyze genes closely associated with aging and telomeres during AD progression. We then validated and explored these findings in the AD cell model using molecular biology methods. This part of the study aims to enhance the clinical relevance of the research by employing bioinformatics to mine transcriptome data from AD patients and to provide scientific evidence for hericenone C as a potential pharmaceutical candidate for AD.

In conclusion, the aim of this study is to explore the potential applications of hydrophobic components in the *H. erinaceus* fruiting body at different levels of material basis, biological activity, and product development, and to provide a new perspective on the study of natural product activities by employing interdisciplinary approaches.

Chapter 2 Extraction and isolation of bioactive hydrophobic components from *Hericium erinaceus* fruiting body

2.1.Introduction

H. erinaceus is a species of medicinal fungus well-regarded for its potential health benefits. It has been an integral part of traditional Chinese medicine for centuries, owing to its various bioactive compounds that demonstrate antioxidant, anti-inflammatory, immunomodulatory, and neuroprotective properties[102–109].

The extraction and isolation of hydrophobic components from the *H. erinaceus* have become a subject of interest in recent years. These hydrophobic components encompass terpenoids, sterols, fatty acids, and other lipophilic compounds [110] . Among these, erinacines and hericenones stand out due to their notable neuroprotective effects and ability to stimulate nerve growth factor (NGF) synthesis, making them of particular interest in the context of neurodegenerative diseases.

Erinacines, a group of diterpenoid compounds, are primarily responsible for the neurodegenerative properties observed in *H. erinaceus* mycelium. These compounds have demonstrated the ability to cross the blood-brain barrier and promote the synthesis of NGF, which is essential for the growth, maintenance, and survival of neurons [111–120] . Similarly, hericenones, aromatic compounds found in the fruiting body, contribute to the mushroom's neuroprotective profile by also enhancing NGF production, but there is a lack of relevant research on hericenones.

Understanding the hydrophobic components of *H. erinaceus* fruiting body and their respective bioactivities provides a foundation for exploring their therapeutic potential in various medical fields. The neuroprotective, anti-inflammatory properties of these compounds highlight the significant promise of *H. erinaceus* as a natural source of novel pharmacological agents.

2.2.Experimental

2.2.1.Fungal material

Mature fruiting bodies of *H. erinaceus* were procured in October 2019 from Aso Biotech, a firm specializing in mushrooms, located in Kumamoto, Japan. The *H. erinaceus* strain used, KX-YB044, was sourced from Kinokkusu Co., Ltd. The cultivation process employed a growth medium made from a mixture of wood chips from deciduous trees, common wheat bran, and rice bran. The mushrooms were cultivated under conditions of 22℃ ± 2℃, with a humidity range of 75-92%, and in the absence of light.

2.2.2.Extraction

The dried and pulverized 4.45kg *H. erinaceus* fruiting body powder was extracted with dichloromethane, yielding a 138.224 g DCM extract. This extract underwent three separate extractions at room temperature, followed by solvent evaporation under reduced pressure.

2.2.3.Isolation

The workflow is shown in Figure 4. Part of the DCM extract (5 g) was separated by high-performance flash chromatography (HPFC) (Biotage® Selekt System). Employing a Biotage® Sfär Silica HC D chromatographic column (High Capacity Duo 20 m 25 g) to isolate, the flow rate was set at 80 mL per minute. The elution was conducted using a progressive gradient, starting with a mixture of n-hexane and ethyl acetate in the ratio of 100:0 to 0:100 by volume, followed by a transition to a mixture of ethyl acetate and methanol in the same volumetric ratio, yielding a total of five distinct fractions, labeled as Fr. D1 through D5.

The subfraction designated as Fr. D2, with a mass of 150.75 mg, was subjected to medium-pressure liquid chromatography (MPLC) using a BUCHI Pure C-850 FlashPrep apparatus. This setup included an Inertsil ODS-3 preparative column from GL Sciences, characterized by dimensions of 20 cm by 250 cm and a particle diameter of 5 micrometers. The chromatographic separation was achieved with a solvent system comprising water and acetonitrile in a volumetric proportion of 4:96, at a flow velocity of 6 mL per minute. This method led to the successful isolation of multiple compounds, identified as follows: compound 1 (4.4 mg, eluted at 151 minutes), compound 2 (3.0 mg, at 221 minutes), compound 3 (5.5 mg, at 331 minutes), compound 4 (3.1 mg, at 203 minutes), compound 5 (20.2 mg, at 189 minutes), compound 6 (8.3 mg, at 290 minutes), compound 7 (4.4 mg, at 133 minutes), compound 8 (7.5 mg, at 211 minutes), compound 9 (2.3 mg, at 319 minutes), compound 10 (2.2 mg, at 144 minutes), and compound 11 (2.3 mg, at 183 minutes), each listed in sequence.

Further, the subfraction Fr. D3, with a mass of 1.54 g, was processed through MPLC on a BUCHI Reveleris® PREP platform. This utilized a silica flash cartridge column, with a solvent gradient of n-hexane to EtOAc, ranging from a 100% n-hexane to a 100% EtOAc mixture (volume ratio), at a flow rate of 30 mL/min. This procedure yielded nine distinct subfractions, labeled Fr. D3-1 through Fr. D3-9.

Among these, Fr. D3-1, weighing 98.69 mg, was subjected to further MPLC separation using the same BUCHI Pure C-850 FlashPrep system and Inertsil ODS-3 column. The elution solvent was a gradient of methanol and isopropanol, starting from 0% to 15% (volume ratio), with a flow rate of 8 mL/min. This led to the collection of compound **12** (6.1 mg, 10 minutes) and compound **13** (8.6 mg, 38.2 minutes).

Additionally, Fr. D3-6, with a mass of 133.8 mg, was also separated via MPLC on the

BUCHI Pure C-850 FlashPrep system with an Inertsil ODS-3 column. The elution solvent

in this case was a mixture of methanol and isopropanol, with a gradient ranging from 0% to 50% (volume ratio), at a flow rate of 8 mL/min. This process resulted in the isolation of compound **14** (61.2 mg, 18.2 minutes) and compound **15** (8.2 mg, 15.4 minutes).

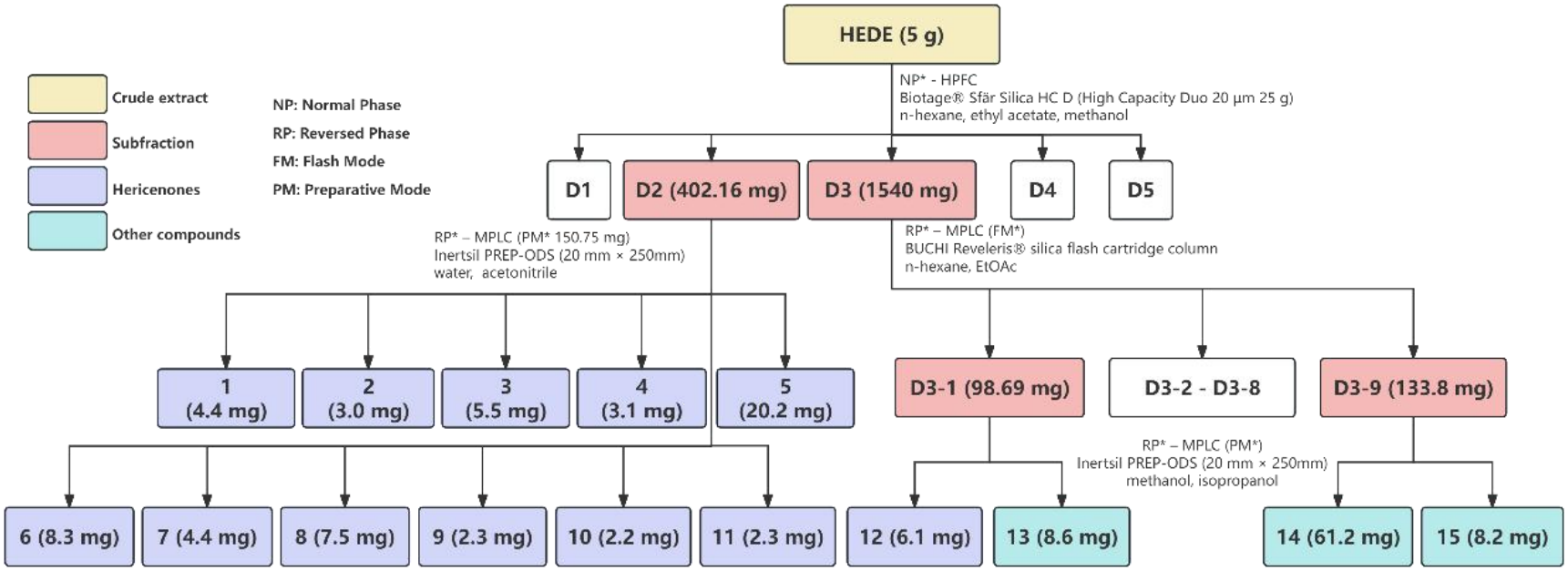

Figure 4. The isolation workflow.

2.2.4.Identification of compounds

2.2.4.1.Spectroscopic measurements and liquid chromatography analysis

Spectral analysis was carried out employing a JASCO V-730BIO UV-VIS spectrophotometer, which was utilized to record ultraviolet (UV) spectra in a methanol solvent. For the acquisition of infrared (IR) spectral data, a JASCO FT/IR-6700 Fourier Transform Infrared (FTIR) spectrometer was deployed. In the context of compound analysis, High-Performance Liquid Chromatography (HPLC) was executed on an Agilent Poroshell 120 EC-C18 analytical column, with dimensions of 3 cm by 100 cm and a particle size of 2.7 micrometers. The HPLC system was coupled with an Agilent 1260 Infinity II LC apparatus, featuring a multi-channel solvent delivery module, an automated sample introduction system, an evaporative light scattering detector, and a diode array detector. The detection system was configured to track wavelengths at 236 nm, 274 nm, and 295 nm.

2.2.4.2.High-resolution mass spectrometry analysis

High-resolution electrospray ionization mass spectrometry (HR-ESI-MS) was performed utilizing an Agilent 6545 Q-TOF LC/MS instrument. The chromatographic analysis was conducted on an Agilent Poroshell 120 EC-C18 column, with dimensions of 2.1 cm by 100 cm and a particle size of 2.7 micrometers. The mobile phase consisted of two components: solvent A, a blend of 95% methanol with 5% ultrapure water in 100% methanol, and solvent B, isopropanol. An injection volume of 1 microliter was delivered at a flow rate of 0.2 milliliters per minute. The UV absorbance of the compounds was monitored at wavelengths of 236 nm, 274 nm, and 295 nm. A gradient

elution was implemented, beginning with 0% B, increasing to 25% B over a 15-minute period, then rapidly increasing to 70% B within 0.5 minutes, holding at 70% B for 4 minutes, followed by a return to 0% B over 0.5 minutes, and concluding with a 4-minute hold at 0% B. The mass spectrometer operated in positive ion mode, with full-scan mass ranges set from m/z 100 to 2000 for MS and m/z 50 to 1500 for MS/MS. The ionization parameters were adjusted to a gas temperature of 250°C, a drying gas flow rate of 12 liters per minute, and a fragmentor voltage set to 120 volts.

2.2.4.3.Nuclear magnetic resonance analysis

Nuclear Magnetic Resonance (NMR) spectral data encompassing proton (^{1}H) NMR, carbon (^{13}C) NMR, ^{1}H–^{1}H Correlation Spectroscopy (COSY), Heteronuclear Multiple Quantum Coherence (HMQC), and Heteronuclear Multiple Bond Coherence (HMBC) were recorded using either a JNM-ECS400 NMR spectrometer from JEOL Ltd. or a DRX 600 NMR spectrometer from Bruker Daltonics, USA. Chemical shifts were reported in parts per million (ppm), using tetramethylsilane (TMS) as an internal standard, with coupling constants noted in hertz. The preparation of samples involved dissolving the compounds in deuterated chloroform ($CDCl_3$) with a purity of 99.8%, provided by FUJIFILM Wako Pure Chemical Corporation. The spectral peaks were referenced to the solvent peak at 7.26 ppm for ^{1}H and 77.16 ppm for ^{13}C. The NMR measurements were performed on instruments operating at frequencies of 400 MHz and 600 MHz.

2.2.4.4.Hydrolysis, methylation, and analysis of fatty acid by GC-MS

Methylation of fatty acids was performed utilizing a kit supplied by NACALAI TESQUE, INC., KYOTO, JAPAN. The process commenced by introducing the

desiccated sample into a sealable test tube. Subsequently, 0.25 ml of hydrolysis reagent A, a mixture of 52% toluene and 48% methanol, and 0.25 ml of hydrolysis reagent B, which includes 93% methanol, were introduced into the tube. The tube was then sealed and kept at a temperature of 37°C for 5 minutes to facilitate the release of fatty acids. To transform these liberated fatty acids into their methyl esters, 0.5 mL of a methylation reagent with a 30% methanol concentration was added, followed by an incubation period of 20 minutes at 37 °C. Afterward, 1.0 mL of an isolation reagent, predominantly n-hexane at 96% purity, was incorporated, and the mixture was vigorously mixed. The supernatant was then transferred to a new test tube, taking care to avoid the inclusion of the turbid layer. Subsequently, 1 mL of deionized water was added to the supernatant, stirred for further purification, and then decanted into another clean test tube.

The subsequent analysis was conducted on an Agilent 7890B Gas Chromatography (GC) system, coupled with an Agilent 5977B Mass Selective Detector (MSD) from Agilent Technologies, USA. The chromatographic separation was executed using an Agilent CP-Sil 88 column, characterized by a length of 100 meters, an internal diameter of 0.25 mm, and a film thickness of 0.20 micrometers. The identification of compounds was based on the comparison of their mass spectral data with those of established reference materials.

2.3.Results and discussion

2.3.1.Determination of new natural compounds

Compound **1** was obtained as a yellow oil and named hericenone O. The HR-ESI/MS analysis yielded a protonated molecular ion peak $[M+H]^+$ at m/z 595.4001, which matched the calculated value for $C_{37}H_{55}O_6^+$ (595.3999). The IR data of **1** showed a

hydroxyl group at 3355 cm^{-1}, an ester-carboxyl group at 1738 cm^{-1}, and α, β-unsaturated carbonyl group at 1621 cm^{-1}. ^{1}H NMR (400 MHz, $CDCl_3$): δ 12.39 (1H, s, HO-3), 10.11 (1H, s, H-8), 6.51 (1H, s, H-6), 6.03 (1H, m, H-6′), 6.01 (1H, m, H-4′), 5.36 (2H, dt, *J* = 8.6, 6.1 Hz, H-9″, H-10″), 5.32 (2H, dt, *J* = 8.0, 6.5 Hz, H-12″, H-13″), 5.32 (2H, s, H-7), 3.90 (3H, s, MeO-9), 2.81 (2H, m, H-1′), 2.78 (2H, dd, *J* = 6.6, 5.9 Hz, H-11″), 2.34 (2H, t, *J* = 7.6 Hz, H-2″), 2.28 (2H, m), 2.23 (3H, d, *J* = 1.24 Hz, H-10′), 2.15 (3H, d, *J* = 1.24 Hz, H-9′), 2.04 (4H, m, H-8″, H-14″), 1.87 (3H, d, *J* = 1.24 Hz, H-8′), 1.62 (6H, m, H-3″, H-7″, H-15″), 1.27 (6H, m, H-4″, H-5″, H-6″), 0.88 (3H, t, *J* = 6.8 Hz, H-18″). ^{13}C NMR (100 MHz, $CDCl_3$): δ 193.3 (C-8), 191.9 (C-5′), 173.3 (C-1″), 163.7 (C-3′), 163.1 (C-3, C-5), 154.3 (C-7′), 138.9 (C-1), 130.4 (C-9″), 130.2 (C-10″), 128.2 (C-12″), 128.0 (C-13″), 126.5 (C-4′), 125.7 (C-6′), 117.6 (C-4), 112.9 (C-2), 105.6 (C-6), 63.1 (C-7), 56.1 (MeO-9), 39.9 (C-2′), 34.3 (C-2″), 25.8 (C-15″), 25.0 (C-16″), 22.7 (C-17″), 20.8 (C-1′), 20.7 (C-10′), 19.4 (C-9′), 14.2 (C-18″), 31.7, 29.70, 29.48, 29.26, 29.22, 29.21, 27.33, 27.31, 25.8, 25.0, 22.7 (C3"-8", 11", 14”-17") (Table 1). The ^{1}H and ^{13}C NMR revealed the presence of a formyl group (δ_H 10.11, δ_C 193.3), a methoxy group (δ_H 3.90, δ_C 56.1), two trisubstituted double bonds at δ_H 6.01(H-4') and 6.03 (H-6'), δ_C 126.5 (C-4'), 125.7 (C-6'), 163.7 (C-3'), and 154.3 (C-7'), and two carbonyl carbons at δ_C 191.9 (C-5') and 173.3 (C-1"). A benzyl alcohol group was inferred from the signals at δ_C 138.9 (C-1), 112.9 (C-2), 163.1 (C-3), 117.6 (C-4),163.1 (C-5), and 105.6 (C-6), δ_H 6.51 (H-6) with carbinol group signals at δ_C 63.1 (C-7) and δ_H 5.3 (H-7). DQFCOSY analysis and the HMBC correlation led to the determination of the gross structure of hericenone O shown in Figure 5. A formyl group was linked to C-2 from the correlations of δ_H 10.11 (H-8) to C-2, 3. A hydroxy group was linked to C-3 from the correlations of δ_H 12.39 (HO-3) to C-2, 3, and 4, and a methoxy group was

linked to C-5 from the correlation of δ_H 3.90 (MeO-9) to C-5. A residue of 3′,7′-dimethyl-4′,6′-octadienyl was linked to C-4 through C-1′ from the correlations of δ_H 2.81 (H-1′) to C-3, 4, 5, in addition to the carbon signals at δ_C 20.8 (C-1′), 39.9 (C-2′), 163.7 (C-3′), 126.5 (C-4′), 191.9 (C-5′), 125.7 (C-6′), 154.3 (C-7′), 27.9 (C-8′), 19.9 (C-9′), and 20.7 (C-10′) with their proton signals at δ_H 2.28 (H-2′), 6.01 (H-4′), 6.03 (H-6′), 1.87 (H-8′), 2.15 (H-9′), and 2.23 (H-10′). The *E*-geometry configurations at the C-3′/C-4′ double bond were deduced from signals in the NOESY spectrum, corresponding to H-4′/H-2′. The core structure was determined as 4-(3′,7′-dimethyl-4′,6′-octa-dienyl)-2-formyl-3-hydroxy-5-methoxybenzyl alcohol, this kind of structure has been found for the first time in a natural source. Moreover, a linoleic acid residue was indicated by the remaining carbon signals at δ_C 173.3 (C-1″), 34.3 (C-2″), 32.1 – 22.7 (C-3″ ~ C-8″, C-11″ ~ C-17″), 130.4 (C-9″), 130.2 (C-10″), 128.2 (C-12″), 128.0 (C-13″) and the terminal methyl 14.2 (C-18″) with their proton signals at δ_H 2.34 (H-2″), 1.62 (H-3"), 1.61 (H-7″, 15″), 2.03 (H-8″, 14″), 5.32 (H-9″, 10″), 5.36(H-12″, 13″), 2.76 (H-11″), 1.24-1.36 (H-4″~6″,15″~17″), and 0.88 (H-18″). The *Z*-geometry configurations at positions C-9″, 10″ and C-12″, 13″ were deduced from signals at 5.32 (dt, J = 8.6, 6.1 Hz) and 5.36 (dt, J = 8.0, 6.5 Hz), respectively in ^{1}H-NMR. The fatty acid in compound **1** was deduced as linoleic acid after hydrolysis, methylation, and analysis through GC/MS, as compared to authentic standard. In addition, this linoleic acid residue was inferred to link to C-7 by an ester bond according to the correlation between δ_H 5.32 (H-7) and C-1, 2, 6, 1″.

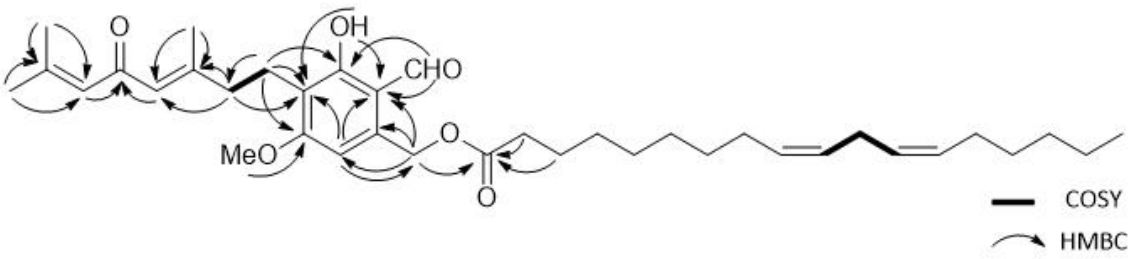

Figure 5. The Gross structure of compound **1** with COSY and key HMBC correlations.

Compound **2** was obtained as a yellow oil and named hericenone P. The HR-ESI/MS gave an ion $[M+H]^+$ peak at m/z 571.3999 (calcd for $C_{35}H_{55}O_6^+$: 571.3999) and corresponded to a molecular formula of $C_{35}H_{54}O_6$. The IR spectrum of **2** showed almost identical data to that of **1**. ^{1}H NMR (400 MHz, $CDCl_3$): δ 12.39 (1H, s, HO-3), 10.11 (1H, s, H-8), 6.52 (1H, s, H-6), 6.04 (1H, m, H-6′), 6.01 (1H, m, H-4′), 5.32 (2H, s, H-7), 3.90 (3H, s, MeO-9), 2.81 (2H, m, H-1′), 2.34 (2H, t, *J* = 7.6 Hz, H-2″), 2.28 (2H, m, H-2′), 2.23 (3H, d, *J* = 1.24 Hz, H-10′), 2.15 (3H, d, *J* = 1.24 Hz, H-9′), 1.88 (3H, d, *J* = 1.24 Hz, H-8′), 1.61 (2H, m, H-3″), 1.25 (24H, m, H-4″ to H-15″), 0.88 (3H, t, *J* = 6.8 Hz, H-16″). ^{13}C NMR (100 MHz, $CDCl_3$): δ 193.3 (C-8), 191.9 (C-5′), 173.4 (C-1″), 163.7 (C-3′), 163.1 (C-3, C-5), 154.3 (C-7′), 138.9 (C-1), 126.5 (C-4′), 125.7 (C-6′), 117.6 (C-4), 112.9 (C-2), 105.6 (C-6), 63.1 (C-7), 56.1 (MeO-9), 39.9 (C-2′), 34.4 (C-2″), 27.9 (C-8′), 20.8 (C-1′), 20.7 (C-10′), 19.4 (C-9′), 14.3 (C-16″), 32.1, 29.83, 29.82, 29.81, 29.80, 29.78, 29.72, 29.59, 29.51, 29.37, 29.25, 25.0, 22.8 (C3" to C15"). DQFCOSY analysis and the HMBC correlation led to the determination of the gross structure of hericenone P shown in Figure 6. The core structure of compound **2** is consistent with compound **1**, and they differ only in the length of fatty acid moiety. A palmitic acid residue was indicated by the remaining carbon signals at δ_C 173.4 (C-1″), 34.4 (C-2″), 32.1 – 22.7 (C-3″ ~ C-15″), and the terminal methyl 14.3 (C-16″) with their

proton signals at δ_H 2.34 (H-2″), 1.61 (H-3″), 1.20-1.33 (H-4″ ~ H-15″), and 0.88 (H-16″). In addition, this palmitic acid residue was inferred to link to C-7 by an ester bond according to the correlation between δ_H 5.32 (H-7) and C-1, 2, 6, 1″. The compound **2** was identified as (*E*)-4-(3,7-dimethyl-5-oxoocta-3,6-dien-1-yl)-2-formyl-3-hydroxy-5-methoxybenzyl palmitate.

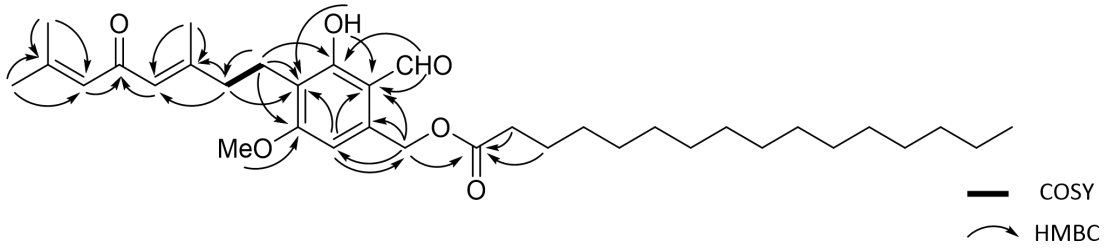

Figure 6. The Gross structure of compound **2** with COSY and key HMBC correlations.

Structures of isolated known compounds were determined by comparison of their spectral data with those reported in the literature. Compounds **3-4**[121] were reported for the first time from a natural source and named hericenone Q-R in this study, and compounds 3 in this study has the same core structure as compounds **1-2**.

Compounds **3** was obtained as a yellow oil. The HR-ESI/MS gave an ion $[M+H]^+$ peak at m/z 599.4314 (calcd for $C_{37}H_{59}O_6^+$, 599.4312) and corresponded to a molecular formula of $C_{37}H_{58}O_6$. ^{1}H NMR (400 MHz, $CDCl_3$): δ 12.39 (1H, s, HO-3), 10.11 (1H, s, H-8), 6.52 (1H, s, H-6), 6.04 (1H, m, H-6′), 6.01 (1H, m, H-4′), 5.32 (2H, s, H-7), 3.90 (3H, s, MeO-9), 2.81 (2H, m, H-1′), 2.34 (2H, t, *J* = 7.6 Hz, H-2″), 2.28 (2H, m), 2.23 (3H, d, *J* = 1.24 Hz, H-10′), 2.15 (3H, d, *J* = 1.24 Hz, H-9′), 1.88 (3H, d, *J* = 1.24 Hz, H-8′), 1.61 (6H, m, H-3″, H-7″, H-15″), 1.25 (6H, m, H-4″, H-5″, H-6″), 0.87 (3H, t, *J*

= 6.8 Hz, H-18″) (Table 3).

Compounds **4** was obtained as a yellow oil. The HR-ESI/MS gave an ion $[M+H]^+$ peak at m/z 597.4161 (calcd for $C_{37}H_{57}O_6^+$, 597.4155) and corresponded to a molecular formula of $C_{37}H_{56}O_6$. ^{1}H NMR (400 MHz, $CDCl_3$): δ 10.41 (1H, s, HO-10), 6.54 (1H, s, H-6), 6.06 (1H, sept, *J* = 1.2 Hz, H-3′), 5.51 (2H, s, H-9), 5.34 (2H, m, H-9″, H-10″), 3.88 (3H, s, MeO-12), 2.82 (1H, d, *J* = 14.2 Hz, H-1′), 2.66 (1H, d, *J* = 14.2 Hz, H-1′), 2.63 (2H, t, *J* = 6.8 Hz, H-4), 2.41 (2H, t, *J* = 7.6 Hz, H-2″), 2.14 (3H, d, *J* = 1.2 Hz, H-6′), 2.01 (1H, m, H-3), 2.00 (4H, m, H-8″, H-11″), 1.91 (1H, dt, *J* = 13.6, 6.9 Hz), 1.86 (3H, d, *J* = 1.2 Hz, H-5′), 1.69 (2H, m, H-3″), 1.44 (3H, s, H-11), 1.28 (20H, m, H-12″ to H-17″), 0.87 (3H, t, *J* = 6.8 Hz, H-18″); ^{13}C NMR (100 MHz, $CDCl_3$): δ 198.1 (C-2′), 190.5 (C-10), 173.4 (C-1″), 162.1 (C-5), 158.4 (C-8a), 156.6 (C-4′), 139.8 (C-7), 130.2 (C-9″), 129.9 (C-10″), 125.1(C-3′), 115.9 (C-8), 109.4 (C-4a), 100.9 (C-6), 77.0 (C-2), 64.7 (C-9), 55.7 (MeO-12), 52.6 (C-1′), 34.6 (C-2″), 30.1 (C-3), 27.9 (C-5′), 25.2 (C-3″), 24.6 (C-11), 21.0 (C-6′), 16.6 (C-4), 14.3 (C-18″), 32.0, 29.90, 29.84, 29.66, 29.47,29.46, 29.36, 29.35, 29.25, 27.36, 27.31, 22.8 (C4″-8″, 11″, 12″-17″) (Table 4).

Table 1. ^{1}H (400 MHz) and ^{13}C NMR (100 MHz) spectroscopic data of compound **1** in $CDCl_3$.

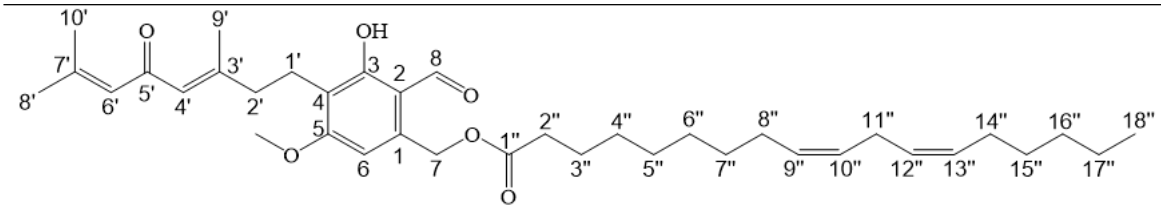

Position	δ_C	δ_H (multiplicity, *J* in Hz)
1	138.9	
2	112.9	
3	163.1	
4	117.6	
5	163.1	
6	105.6	6.51 (s)
7	63.1	5.32 (s)
8	193.3	10.11 (s)
OMe	56.1	3.90 (s)
OH		12.39 (s)
1'	20.8	2.83-2.78 (m)
2'	39.9	2.30-2.25 (m)
3'	163.7	
4'	126.5	6.02-6.00 (m)
5'	191.9	
6'	125.7	6.04-6.02 (m)
7'	154.3	

8'	27.9	1.87 (d, 1.24)
9'	19.4	2.15 (d, 1.24)
10'	20.7	2.23 (d, 1.24)
1"	173.3	
2"	34.3	2.34 (t, 7.6)
3"	-[a]	1.66-1.50 (m)
7", 15"	-[a]	1.66-1.50 (m)
8", 14"	-[a]	2.08-1.97 (m)
9", 10"	130.4, 130.2	5.32 (dt, 8.6, 6.1)
12", 13"	128.2, 128.0	5.36 (dt, 8.0, 6.5)
11"	-[a]	2.78 (dd, 6.6, 5.9)
4" - 6"	-[a]	1.39-1.21 (m)
16", 17"	-[a]	
18"	14.2	0.88 (t, 6.8)

[a]31.7, 29.70, 29.48, 29.26, 29.22, 29.21, 27.33, 27.31, 25.8, 25.0, 22.7 (C3″-8″, 11″, 14″-17″).

Table 2. ^{1}H (400 MHz) and ^{13}C NMR (100 MHz) spectroscopic data of compound **2** in $CDCl_3$.

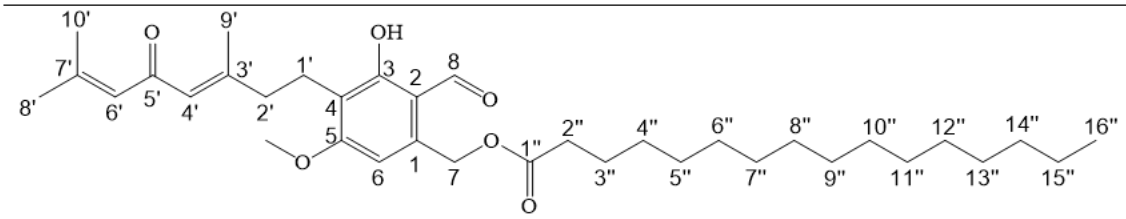

Position	δ_C	δ_H (multiplicity, *J* in Hz)
1	138.9	
2	112.9	
3	163.1	
4	117.6	
5	163.1	
6	105.6	6.52 (s)
7	63.1	5.32 (s)
8	193.3	10.11 (s)
OMe	56.1	3.90 (s)
OH		12.39 (s)
1'	20.8	2.83-2.78 (m)
2'	39.9	2.30-2.25 (m)
3'	163.7	
4'	126.5	6.02-6.00 (m)
5'	191.9	
6'	125.7	6.04-6.02 (m)
7'	154.3	

8'	27.9	1.88 (d, 1.24)
9'	19.4	2.15 (d, 1.24)
10'	20.7	2.23 (d, 1.24)
1"	173.4	
2"	34.4	2.34 (t, 7.6)
3"	-[a]	1.66-1.50 (m)
4"-15"	-[a]	1.35-1.20 (m)
16"	14.3	0.88 (t, 6.8)

[a]32.1, 29.83, 29.82, 29.81, 29.80, 29.78, 29.72, 29.59, 29.51, 29.37, 29.25, 25.0, 22.8 (C3″ to C15″).

Table 3. Comparisons of ^{1}H (400 MHz) spectroscopic data of natural and synthetic compound **3** in $CDCl_3$.

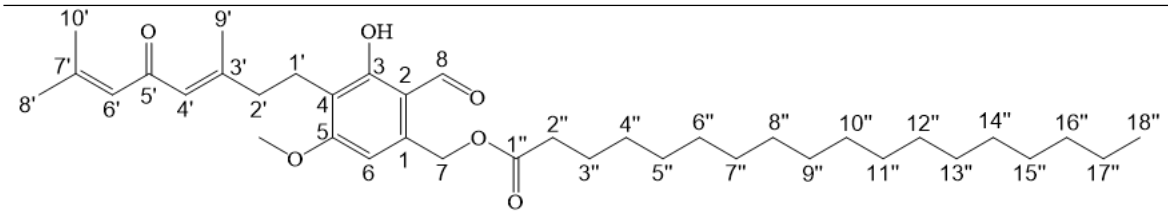

Position	synthetic compound[a]	natural product
	δ_H (multiplicity, *J* in Hz)	δ_H (multiplicity, *J* in Hz)
6	6.52 (s)	6.52 (s)
7	5.32 (s)	5.32 (s)
8	10.11 (s)	10.11 (s)
OMe	3.90 (s)	3.90 (s)
OH	12.39 (s)	12.39 (s)
1'	2.81 (m)	2.83-2.78 (m)
2'	2.28 (m)	2.30-2.25 (m)
3'		
4'	6.01 (m)	6.02-6.00 (m)
5'		
6'	6.03 (m)	6.04-6.02 (m)
7'		
8'	1.88 (d, 1.0)	1.88 (d, 1.24)
9'	2.15 (d, 1.0)	2.15 (d, 1.24)
10'	2.23 (d, 1.0)	2.23 (d, 1.24)
1"		

2"	2.34 (t, 7.6)	2.34 (t, 7.6)
3"	1.61 (m)	1.66-1.50 (m)
4"-17"	1.35-1.21 (m)	1.35-1.21 (m)
18"	0.87 (t, 6.8)	0.87 (t, 6.8)

[a]Kobayashi, S. et al. (2021). Total Synthesis, Structure Revision, and Neuroprotective Effect of Hericenones C-H and Their Derivatives. *Journal of Organic Chemistry, 86*(3), 2602–2620.

Table 4. Comparisons of ^{1}H (400 MHz) and ^{13}C NMR (100 MHz) spectroscopic data of natural and synthetic compound **4** in $CDCl_3$.

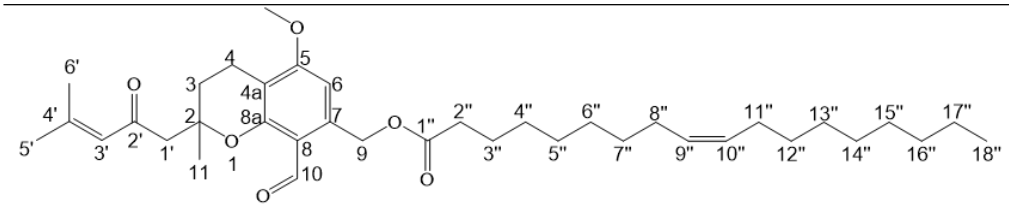

Position	synthetic compound[a]		natural product	
	δ_H (multiplicity, *J* in Hz)	δ_C	δ_H (multiplicity, *J* in Hz)	δ_C
2		77.0		77.0
3		30.1	2.04-1.97 (m)	30.1
	1.91 (dt, 13.6, 6.8)		1.91 (dt, 13.8, 6.9)	
4	2.63 (t, 6.8)	16.6	2.63 (t, 6.8)	16.6
4a		109.3		109.4
5		162.0		162.1
6	6.54 (s)	100.9	6.54 (s)	100.9
7		139.8		139.8
8		115.8		115.9
8a		158.4		158.4
9	5.51 (br s)	64.7	5.51 (s)	64.7
10	10.41 (s)	190.5	10.41 (s)	190.5
11	1.44 (s)	24.6	1.44 (s)	24.6
OMe	3.88 (s)	55.7	3.88 (s)	55.7
1'	2.82 (d, 14.0) 2.66 (d, 14.0)	52.6	2.82 (d, 14.2) 2.66 (d, 14.2)	52.6

2'		198.1		198.1
3'	6.06 (sept, 1.2)	125.1	6.06 (sept, 1.2)	125.1
4'		156.6		156.6
5'	1.86 (d, 1.2)	27.9	1.86 (d, 1.2)	27.9
6'	2.14 (d, 1.2)	21.0	2.14 (d, 1.2)	21.0
1"		173.4		173.4
2"	2.41 (t, 7.5)	34.5	2.41 (t, 7.6)	34.6
3"	1.73-1.64 (m)	25.2	1.73-1.64 (m)	25.2
4"-7"	1.37-1.24 (m)	-[b]	1.37-1.24 (m)	-[c]
8", 11"	2.05-1.98 (m)	-[b]	2.05-1.98 (m)	-[c]
9", 10"	5.37-5.31 (m)	130.2, 129.8	5.37-5.31 (m)	130.2, 129.9
12"-17"	1.37-1.24 (m)	-[b]	1.37-1.24 (m)	-[c]
18"	0.87 (t, 6.8)	14.3	0.87 (t, 6.8)	14.3

[a]Kobayashi, S. et al. (2021). Total Synthesis, Structure Revision, and Neuroprotective Effect of Hericenones C-H and Their Derivatives. *Journal of Organic Chemistry, 86*(3), 2602–2620. [b]32.0, 29.89, 29.84, 29.66, 29.46, 29.36, 29.35, 29.25, 27.34, 27.29, 22.8 (C4″-8″, 11″, 12″-17″). [c]32.0, 29.90, 29.84, 29.66, 29.47,29.46, 29.36, 29.35, 29.25, 27.36, 27.31, 22.8 (C4″-8″, 11″, 12″-17″).

2.3.2.Determination of known natural compounds

Compound **5** was obtained as a yellow oil. The ESI-MS gave an ion [M+H]+ peak at m/z 571.4003 (calc for $C_{35}H_{55}O_6^+$: 571.3999), suggesting a molecular formula of $C_{35}H_{54}O_6$. The ^1H NMR spectrum was compared with the previous paper[63], and it was determined as hericenone C.

Compound **6** was obtained as a yellow oil. The ESI-MS gave an ion [M+H]+ peak at m/z 599.4317 (calc for $C_{37}H_{59}O_6^+$: 599.4312), suggesting a molecular formula of $C_{37}H_{58}O_6$. The ^1H NMR spectrum was compared with the previous paper[63], and it was determined as hericenone D.

Compound **7** was obtained as a yellow oil. The ESI-MS gave an ion [M+H]+ peak at m/z 595.4008 (calc for $C_{37}H_{55}O_6^+$: 595.3999), suggesting a molecular formula of $C_{37}H_{54}O_6$. The ^1H NMR spectrum was compared with the previous paper[63], and it was determined as hericenone E.

Compound **8** was obtained as a yellow oil. The ESI-MS gave an ion [M+H]+ peak at m/z 571.4001 (calc for $C_{35}H_{55}O_6^+$: 571.3999), suggesting a molecular formula of $C_{35}H_{54}O_6$. The ^1H NMR spectrum was compared with the previous paper[97], and it was determined as hericenone F.

Compound **9** was obtained as a yellow oil. The ESI-MS gave an ion [M+H]+ peak at m/z 599.4313 (calc for $C_{37}H_{59}O_6^+$: 599.4312), suggesting a molecular formula of $C_{37}H_{59}O_6$. The ^1H NMR spectrum was compared with the previous paper[97], and it was determined as hericenone G.

Compound **10** was obtained as a yellow oil. The ESI-MS gave an ion [M+H]+ peak at m/z 595.4008 (calc for $C_{35}H_{55}O_6^+$: 595.3999), suggesting a molecular formula of $C_{35}H_{54}O_6$. The ^1H NMR spectrum was compared with the previous paper[97], and it was

determined as hericenone H.

Compound **11** was obtained as a yellow oil. The ESI-MS gave an ion [M+H]+ peak at m/z 599.4154 (calc for $C_{37}H_{57}O_6^+$: 597.4155), suggesting a molecular formula of $C_{37}H_{56}O_6$. The ^{1}H NMR spectrum was compared with the previous paper[98], and it was determined as hericenone I.

Compound **12** was obtained as a colorless crystal. The ESI-MS gave an ion $[M+H]^+$ peak at m/z 317.1748 (calc for $C_{19}H_{25}O_4^+$: 317.1752), suggesting a molecular formula of $C_{19}H_{24}O_4$. The ^{1}H NMR spectrum was compared with the previous paper[100], and it was determined as Hericenone J.

Compound **13** was obtained as a white powder. The ESI-MS gave an ion [M+H]+ peak at m/z 397.3466 (calc for $C_{28}H_{45}O$: 397.3470), suggesting a molecular formula of $C_{28}H_{44}O$. The ^{1}H NMR spectrum was compared with the previous paper[122], and it was determined as ergosterol.

Compound **14** was obtained as a white crystal. The ESI-MS gave an ion [M+H]+ peak at m/z 429.3367 (calc for $C_{28}H_{45}O_3$: 429.3369), suggesting a molecular formula of $C_{28}H_{44}O_3$. The ^{1}H NMR spectrum was compared with the previous paper[123], and it was determined as ergosterol peroxide.

Compound **15** was obtained as a white powder. The ESI-MS gave an ion [M+H]+ peak at m/z 427.3209 (calc for $C_{28}H_{45}O$: 427.3212), suggesting a molecular formula of $C_{28}H_{44}O$. The ^{1}H NMR spectrum was compared with the previous paper[124], and it was determined as 9,11-dehydroergosterol peroxide.

Table 5. Comparison of the ^{1}H NMR data of documented and isolated in this experiment Hericenone C in $CDCl_3$.

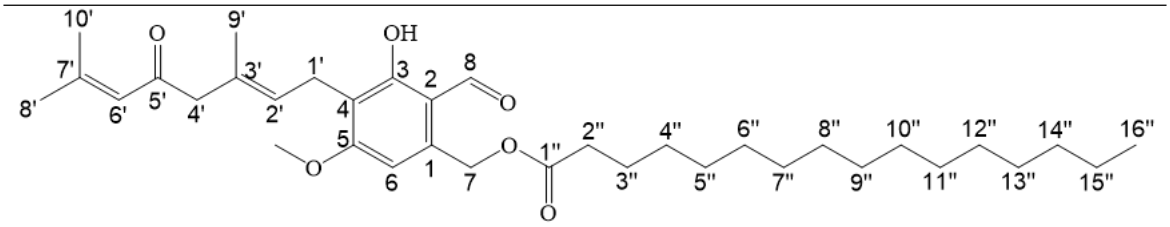

Position	δ_H (multiplicity, *J* in Hz)	
	Previous paper[α]	This experiment
6	6.53 (s)	6.52 (s)
7	5.32 (s)	5.32 (s)
8	10.11 (s)	10.10 (s)
OMe	3.91 (s)	3.91 (s)
OH	12.38 (s)	12.37 (s)
1'	3.4 (d, 7.33)	3.39 (d, 7.2)
2'	5.32 (t,7.33)	5.32 (t, 7.9)
4'	3.01 (s)	3.00 (s)
6'	6.09 (s)	6.08 (s)
8'	1.84 (s)	1.84 (s)
9'	1.78 (s)	1.77 (s)
10'	2.12 (s)	2.12 (s)
2"	2.33 (dd, 7.70, 7.32)	2.33 (t, 7.6)
3"	1.61 (m)	1.60 (m)
4"-15"	1.25 (m)	1.24 (m)
16"	0.88 (t, 6.96)	0.87 (t, 6.92)

[α]Kawagishi, Hirokazu. et al. "Hericenones C, D and E, stimulators of nerve growth factor (NGF)-synthesis, from the mushroom *Hericium erinaceum*." *Tetrahedron Letters* 32.35 (1991): 4561-4564.

2.4.Conclusion

In this research, a total of twelve hericenones and three sterols were extracted from the fruiting bodies of *H. erinaceus* (Figure 7). Notably, compounds numbered **1**-**4** were identified in a natural source for the first time. The chemical analysis conducted proved to be instrumental, serving dual purposes: it shed light on the presence of novel hericenone constituents within *H. erinaceus* and simultaneously laid a foundation for subsequent studies on the biological activity of hericenone C. It is worth noting that hericenone C, as the most abundant compound in this class, was prepared in large quantities and laid the foundation for subsequent cell and animal experiments.

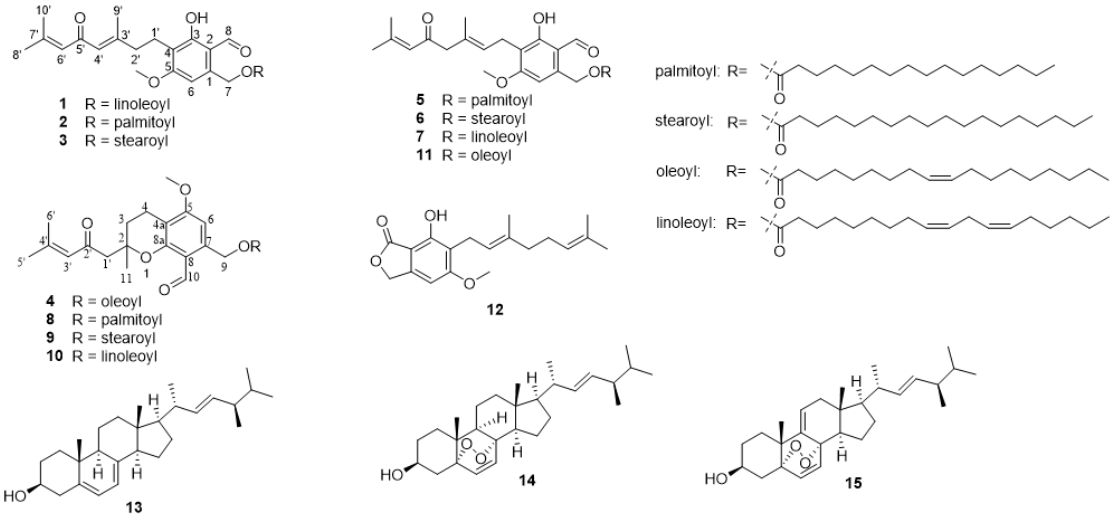

Figure 7. Chemical structures of compounds **1**-**15**.

Chapter 3 Metabolomic analysis of components entering the bloodstream（Plasma pharmacochemistry study）

3.1.Introduction

The therapeutic properties of natural herbal components have garnered widespread recognition due to their bioactive constituents [125] . These components, rooted in traditional medicine, have been utilized for centuries to treat a myriad of ailments[126]. In contemporary research, the quest to elucidate the mechanisms of action and efficacy of these natural compounds has led to the adoption of sophisticated analytical methods[127,128].

Plasma pharmacochemistry, a widely recognized and commonly employed research approach, facilitates the metabolomic analysis of bioactive components of natural products that are absorbed into the bloodstream. This method is pivotal in understanding the pharmacokinetics and pharmacodynamics of herbal compounds, thereby providing insights into their therapeutic efficacy [129,130] . Ultra-performance liquid chromatography-tandem mass spectrometry (UPLC-MS/MS) has emerged as a powerful tool for the rapid identification of active constituents in blood samples following oral administration of herbal preparations. This technique's high sensitivity and resolution enable the precise quantification and characterization of multiple bioactive compounds, even in complex biological matrices[131,132].

In this study, our goal is to apply metabolomics analysis to identify compounds that can exist in their original form in mouse blood after the intake of hydrophobic components. On one hand, understanding the components that can enter the bloodstream at high levels in HEDE, combined with research on network pharmacology, can reveal their potential biological activities. On the other hand, determining whether hericenone C can enter the bloodstream in its original form can provide insights into whether it can be transported via the blood to target organs to exert relevant biological activities, laying

the foundation for subsequent pharmacological research.

3.2.Experimental

3.2.1.Animals

Male C57BL/6 mice, aged 6-8 weeks and weighing between 20-22 grams, were sourced from the Jiangsu Huachuang Sino Medical Technology CO., Ltd., China. Animal License Number: SCXK(SU)2020-0009. These mice were housed in an experimental animal facility, where they were acclimated for one week under controlled conditions of temperature at 22 ± 2°C, relative humidity at 55 ± 10%, and a 12-hour light cycle. All animal use adhered to the guidelines for animal ethics and welfare.

3.2.2.Metabolomics analysis

3.2.2.1.Plasma sample preparation

The animal experiment procedure is shown in Figure 8. Twenty-seven C57 mice were evenly and randomly distributed into three groups of nine: a HEDE group (n = 9), a hericenone C group (n=9), or a blank group (n = 9). All animals were administered with HEDE (200 mg/kg), hericenone C (30 mg/kg) by gavage once a day for consecutive seven days in experiment group (HEDE and hericenone C made into a suspension with saline containing 0.5% CMC–Na sodium carboxymethylcellulose), or an equivalent amount of normal saline in the blank group. On the seventh day, blood samples were collected two hours after the last administration. Mice were weighed and anesthetized with an intraperitoneal injection of 2% pentobarbital at a dosage of 50 mg/kg. Blood was drawn from the abdominal aorta, allowed to coagulate for one hour at room temperature, and then centrifuged at 3000 rpm for 15 minutes at 4 °C to isolate the plasma. UHPLC-MS/MS was utilized to analyze the supernatant fluid, blood samples

from three mice were pooled to form a single analytical sample, with a volume of 0.25 mL per mouse. All plasma samples were frozen at -80°C for subsequent analysis.

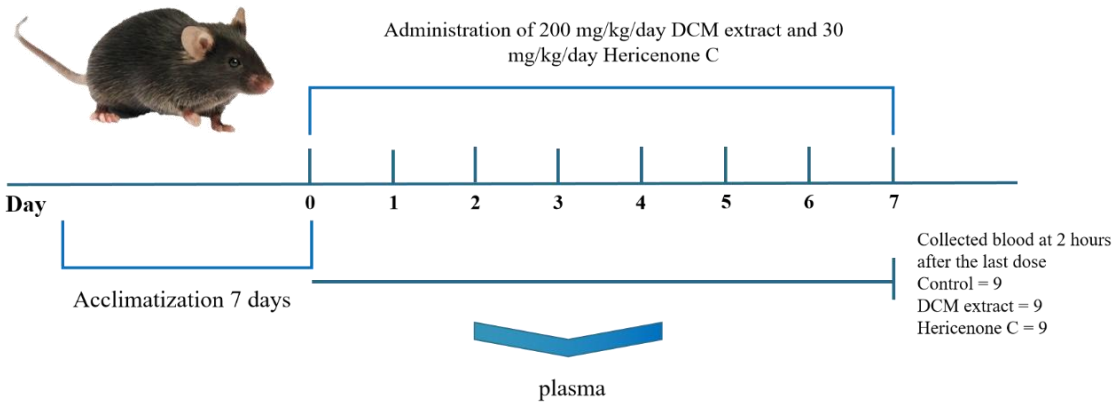

Figure 8. Work flow of animal experiment.

The list of analyzed samples is shown below (Table 6). Pipette 600 μL of a 2 g/mL HEDE sample into a 1.5 mL EP tube; add 400 μL of anhydrous methanol, mix thoroughly by vortexing for 10 seconds, then take 200 μL of this solution and add 200 μL of a 40% methanol aqueous solution; vortex mix for another 10 seconds; centrifuge for 15 minutes at 16,000 g and 4°C, collect the supernatant, which constitutes the HEDE analytical group sample. The standard for hericenone C is prepared by dissolving in methanol at a concentration of 0.25 mg/mL. For plasma samples, take an appropriate volume, add methanol, and vortex mix for 60 seconds, then let it stand at -20°C for 30 minutes, followed by centrifugation at 16,000 g for 20 minutes at 4°C, collect the supernatant and dry it under vacuum, resuspend the residue in 100 μL of a 40% methanol aqueous solution, vortex, and centrifuge again at 16,000 g for 15 minutes at 4°C, collect the supernatant, which constitutes the plasma analytical group sample. The processing of the blank plasma plus HEDE is as follows: take blank plasma, add a

solution of HEDE, add methanol, vortex mix for 60 seconds, let it stand at -20°C for 30 minutes, centrifuge at 16,000 g for 20 minutes at 4°C, collect the supernatant and dry it under vacuum, resuspend the residue in 100 μL of a 40% methanol aqueous solution, vortex, and centrifuge at 16,000 g for 15 minutes at 4°C, collect the supernatant, which constitutes the processed sample.

Table 6. List of samples.

Sample name	Sample name abbreviation	Number of samples
DCM extract	HEDE	1
Hericenone C	HEC	1
Blank plasma	CON	3
Plasma of HEDE administration	PHEDE	3
Plasma of hericenone C administration	PHEC	3

3.2.2.2.Metabolomics analysis conditions

The plasma samples were examined utilizing a Vanquish UHPLC apparatus from Thermo Scientific, based in Waltham, MA, coupled with a HSS-T3 column (100 x 2.1 mm, with 1.8 μm particle size; Waters). The column was maintained at a temperature of 35 ℃ within its compartment. The mobile phase consisted of solvent A, which was water containing 0.1% formic acid, and solvent B, which was acetonitrile also containing 0.1% formic acid (both LC-MS grade solvents sourced from Fisher Chemical). The samples were separated at a flow rate of 0.3 mL per minute, following a defined gradient elution: starting with a 1-minute isocratic condition at 5% solvent B,

followed by a linear gradient to 98% B over the course of 16 minutes, then a quick reversion to the initial 5% B within 0.5 minutes, and concluding with a 2.5-minute isocratic phase at the starting 5% B concentration.

The analysis was conducted using a Q-Exactive HFX mass spectrometer from Thermo Fisher Scientific, Bremen, Germany, which was interfaced with the UHPLC system. Mass spectral data acquisition was performed in both positive and negative ionization modes of electrospray, with a data-dependent strategy. The mass range for acquisition extended from m/z 90 to 1,300. The MS/MS spectra were obtained by selecting the top ten most intense peaks from the MS1 scan. High-energy collision dissociation was applied in a stepwise manner, with collision energies at levels of 20, 40, and 60. The capillary temperature was kept at 320 ℃ , and the probe heater temperature was regulated at 350℃.

Compound annotation was done by matching accurate mass, isotopic distributions, and MS/MS spectral to reference data from an in-house standards TCM database (Shanghai Applied Protein Technology CO., Ltd., Shanghai, China) and public databases GNPS[133], ReSpect[134]and Massbank[135].

Precisely aspirate 6 μL each of samples from the CON group, PHEDE group, PHEC group, and HEDE+CON group, as well as 2 μL each of samples from the HEDE group and HEC group for LC-MS injection analysis. Each batch of CON group samples and dosed plasma group samples were injected once, the HEDE+CON group samples were injected in triplicate, and the HEDE group and HEC group samples were injected in quintuplicate.

3.2.3.Data processing

The raw format raw data files were imported into ProteoWizard for conversion into

the .mzXML format. Subsequently, XCMS software was utilized for peak alignment, retention time correction, and peak extraction. Compound identification was performed by searching against a local high-resolution mass spectrometry database of traditional Chinese medicine from the Institute of New Life Sciences, with a primary mass error tolerance of less than 25 ppm and a secondary fragmentation spectrum match score greater than 0.7. The higher the score, the greater the similarity of the mass spectrum [136,137] . It is generally accepted that a score above 0.7 indicates reliable identification results[138,139].

3.3.Results and discussion

3.3.1.Components in the HEDE that can enter the bloodstream in their original form

This research examines the durability of the experimental apparatus and the veracity of the data obtained. The findings from the HEDE sample's detection were subjected to a Pearson correlation analysis, depicted in Figure 9. A correlation coefficient above the 0.9 mark is generally regarded as indicative of a robust correlation. The experimental outcomes reveal that the correlation coefficients for the sample comparisons consistently exceed 0.9, underscoring the experiment's high reproducibility and confirming the stability and credibility of the data.

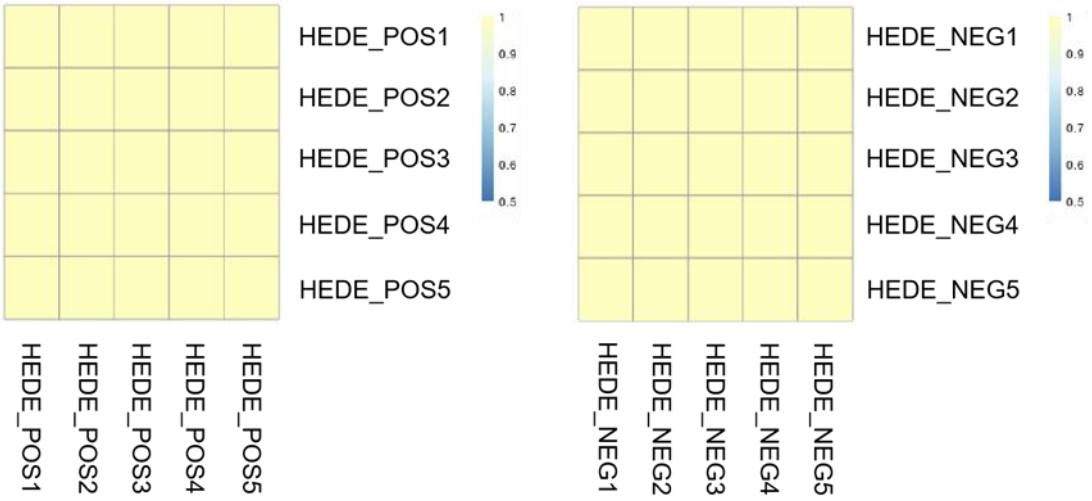

Figure 9. Correlation of samples in positive and negative ion modes.

In this study, UHPLC-HRMS was employed to collect data from the CON samples, PHEDE samples, CON+HEDE samples, and HEDE samples. A comparative analysis of the base peak chromatograms (BPC) for both positive and negative ions was conducted, as depicted in Figure 10. The spectra visually reveal significant differences between the HEDE sample and the biological samples, with discernible variations observed between the chromatograms of the treated groups and the blank control group.

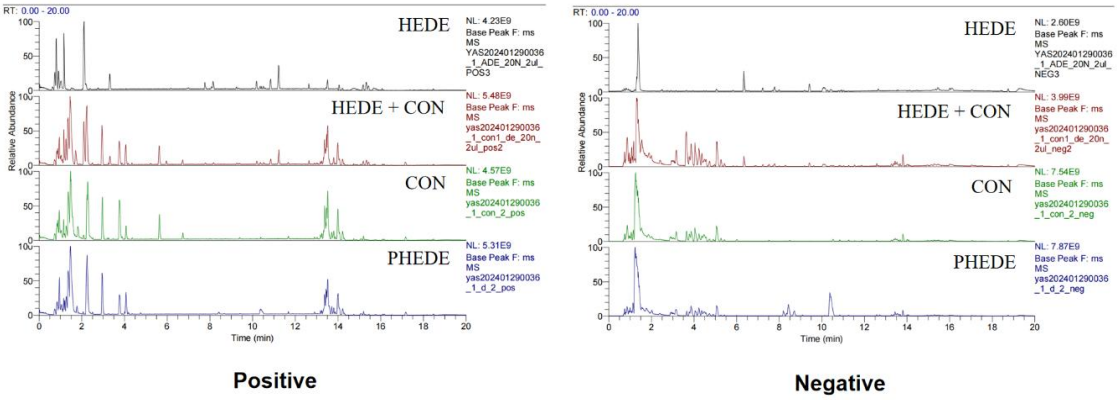

Figure 10. The BPC diagrams of each group of samples in positive and negative ion

detection modes.

Compounds identification was performed by searching a HRMS database with a mass error of less than 25 ppm for the MS spectrum and a MS/MS fragmentation spectrum matching score greater than 0.7. The chemical components in the HEDE and PHEDE samples were analyzed and identified, and the statistical results are shown in Table 7.

Table 7. Identified components in positive and negative modes.

Detection mode	The amount of identified components	The amount of components entering the blood
Positive	1481	157
Negative	626	63
Total	2003	219

The compounds identified in this experiment were annotated according to the NPClassifie classification method [140] . The number of compounds identified in each pathway and main superclass are shown in Table 8, as illustrated in Figure 11A. The proportion of each compound category is shown in Figure 11B for the compounds that entered the bloodstream. Compounds identification classifies the top 5 categories of pathways and superclasses. For the compounds that enter the bloodstream, the classification displays the top 5 categories of pathways, superclasses, and the top 3 categories of classes.

In the BPC of the positive and negative ion modes of HEDE, chromatographic peaks with higher abundance were confirmed for peak shape and secondary spectrum inspection. Then, the chromatographic peaks in the positive and negative ion charts were sequentially marked with numbers in numerical order, as shown in Figure 12. A total of 31 chromatographic peaks were marked, and the corresponding identified compound information is presented in Table 9, with the NPClassifier chemical classification shown in Figure S49.

Table 8. Pathway, superclass, and count of compounds.

Pathway	SuperClass	count
Alkaloids	Anthranilic acid alkaloids	64
	Nicotinic acid alkaloids	61
	Pseudoalkaloids	63
	Tryptophan alkaloids	70
	Tyrosine alkaloids	40
	other	298
Amino acids and Peptides	Oligopeptides	7
	Small peptides	167
	other	11
Carbohydrates	Aminosugars and aminoglycosides	3
	Nucleosides	21
	Polyols	1
	Saccharides	18
	other	2
Fatty acids	Fatty Acids and Conjugates	103
	Fatty amides	25
	Fatty esters	25
	Glycerophospholipids	31
	Octadecanoids	20
	other	81
Polyketides	Aromatic polyketides	12
	Chromanes	19
	Cyclic polyketides	11
	Linear polyketides	11
	Macrolides	15
	other	44
Shikimates and Phenylpropanoids	Coumarins	42
	Flavonoids	45
	Lignans	9
	Phenolic acids (C6-C1)	53
	Phenylpropanoids (C6-C3)	23
	other	80
Terpenoids	Diterpenoids	47
	Monoterpenoids	23
	Sesquiterpenoids	47
	Steroids	67
	Triterpenoids	35
	other	35
other	Meroterpenoids	12
	Oligopeptides	7
	Peptide alkaloids	6
	Pseudoalkaloids	6
	Small peptides	13
	other	39

A

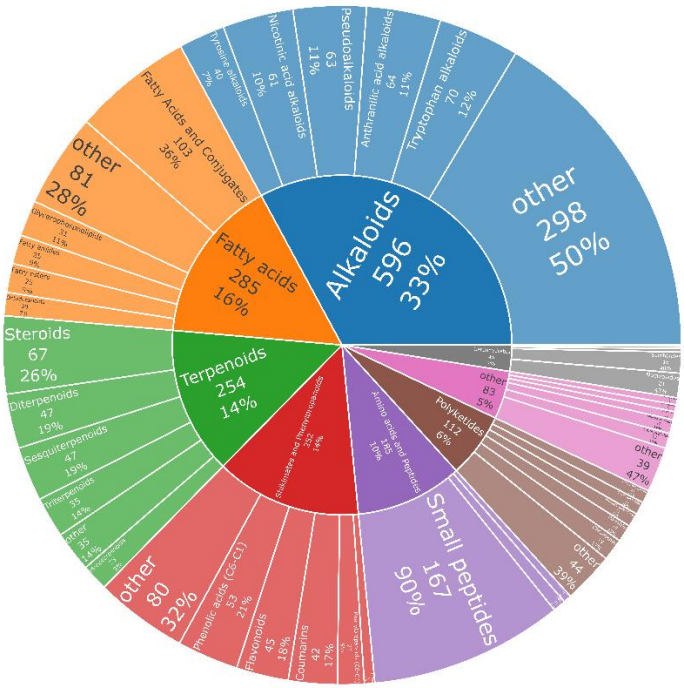

B

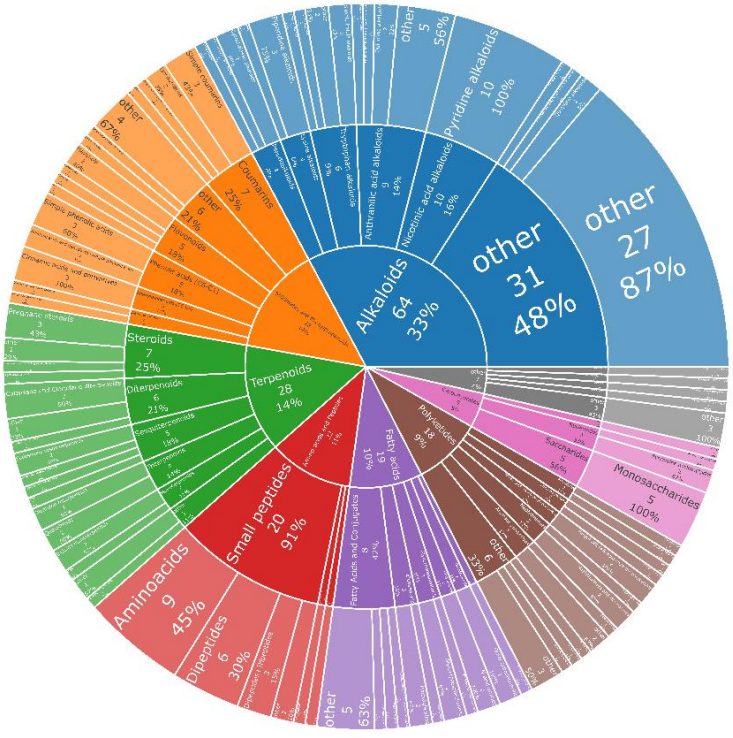

Figure 11. The proportion of HEDE compounds (A) and compounds that enter the bloodstream (B) in various chemical classifications.

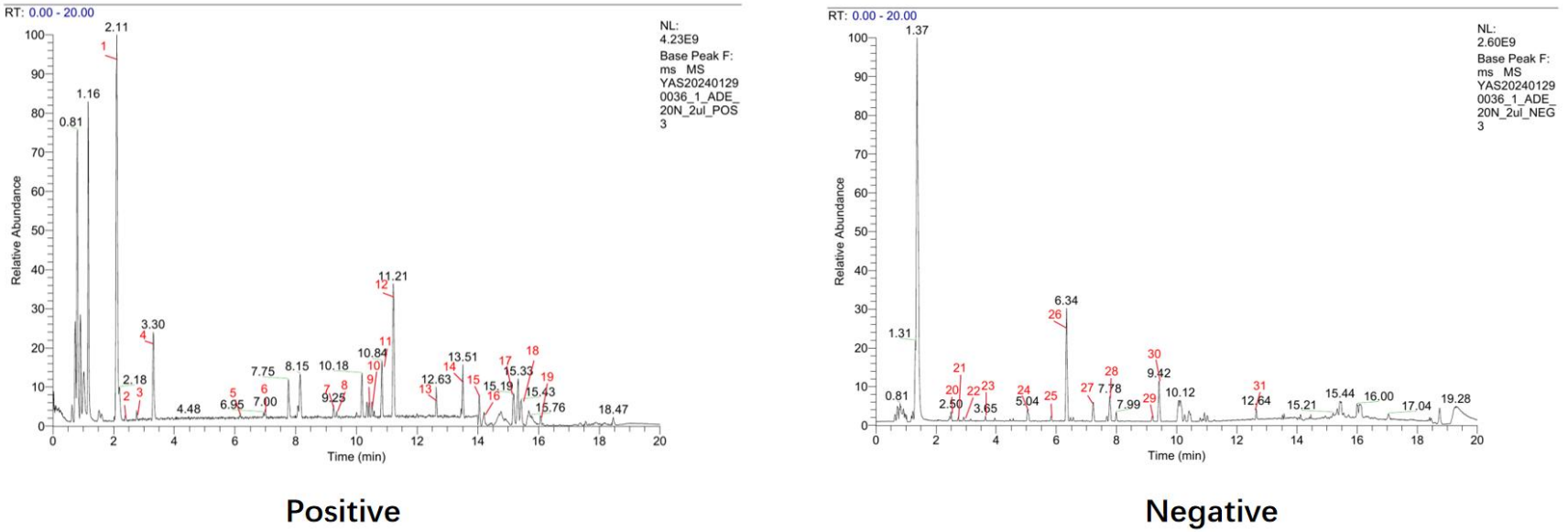

Figure 12. The BPC charts of HEDE under positive and negative ion modes—marked peaks.

Table 9. Identification results of chemical components of marked peaks in BPC charts.

Peak number	m/z	RT min	Formula	ppm	compound name	adduct	score	PubCHEM	CAS	Product Ion	Into Blood or None
1	153.0546	2.11	C8H8O3	0.1	3-Hydroxy-2-methoxybenzaldehyde	[M+H]+	0.989	11804953	66495-88-3	[153.05, 101.02, 97.03, 154.06, 107.05]	Into_Blood
2	151.123	2.45	C9H14N2	0.2	2-Butyl-3-methylpyrazine	[M+H]+	0.998	85228	15987-00-5	[151.12, 152.13, 109.08, 110.08, 151.09]	None
3	195.1129	2.77	C10H14N2O2	0	(5aR,10aR)-Octahydrodipyrrolo[1,2-a:1',2'-d]pyrazine-5,10-dione	[M+H]+	0.962	6932481	53990-71-9	[195.11, 98.06, 196.12, 196.1, 99.06]	Into_Blood
4	114.0916	3.32	C6H11NO	2	3,3-Dimethyl-2-pyrrolidone	[M+H]+	0.999	5114908	4831-43-0	[114.09, 96.08, 115.1, 97.07, 114.11]	None
5	289.107	6.18	C16H18O6	0.1	O-Desmethylmycophenolic acid	[M+H-H2O]+	0.883	25879063	31858-65-8	[289.11, 99.04, 243.1, 172.09, 215.11]	None
6	384.217	6.99	C23H31NO5	0.1	Antibiotic F 1839A	[M+H-H2O]+	0.762	10069635	159096-43-2	[384.22, 246.11, 216.1, 149.06, 385.13]	None
7	371.1465	9.26	C21H22O6	6.7	2-Oxatricyclo[13.2.2.13,7]eicosa-3,5,7(20),8,15,17,18-heptaen-12-one, 5,10-dihydroxy-4,6-dimethoxy-	[M+H]+	0.771	1.29E+08	2111898-00-9	[371.15, 313.1, 215.03, 372.15, 314.11]	Into_Blood
8	307.1516	9.36	C15H24O5	0.1	Dimethyl 2-((1S,2R)-3-oxo-2-pentylcyclopentyl)malonate	[M+Na]+	0.998	7060951	308368-94-7	[307.15, 308.15, 307.23, 307.07, 307.09]	None
9	465.2386	10.43	C25H36O8	20.7	5.beta.-Androst-1-en-17.beta.-ol-3-one glucuronide	[M+H]+	0.941		361432-77-1	[465.24, 349.15, 466.24, 367.17, 327.13]	None
10	396.1783	10.52	C21H27NO5	0.3	Spirotetramat	[M+Na]+	0.998			[396.18, 397.18, 99.04, 396.3, 99.05]	Into_Blood
11	330.1699	10.84	C19H23NO4	0.6	Sinomenine	[M+H]+	0.947	5459308	115-53-7	[330.17, 192.07, 232.1, 164.07, 331.18]	None
12	353.1358	11.22	C19H22O5	0.6	5'-(Furan-3-yl)-4a-hydroxy-4,7-dimethylspiro[5,6,7,8a-tetrahydro-1H-naphthalene-8,3'-oxolane]-2,2'-dione	[M+Na]+	0.893	45359774		[353.14, 215.03, 353.23, 354.14, 353.19]	Into_Blood
13	316.1907	12.63	C19H25NO3	0	Piperolein A	[M+H]+	0.779	11141599	30505-92-1	[316.19, 192.07, 164.07, 317.19, 218.08]	Into_Blood
14	520.3396	13.51	C26H50NO7P	0.2	1-Linoleoyl-sn-glycero-3-phosphorylcholine	[M+H]+	0.955	11988421	22252-07-9	[184.07, 104.11, 520.34, 125.0, 502.33]	None
15	420.253	14.05	C27H41NO6S	8.6	Epothilone B	[M+H-C3H4O3]+	0.784	448013	152044-54-7	[420.25, 105.07, 296.13, 421.26, 204.07]	None
16	522.3553	14.2	C26H52NO7P	0.4	18:1 Lyso PC	[M+H]+	0.971	16081932	19420-56-5	[184.07, 104.11, 522.36, 125.0, 504.34]	None
17	256.2633	15.18	C16H33NO	0.7	Palmitamide	[M+H]+	0.993	69421	629-54-9	[256.26, 257.27, 102.09, 116.11, 130.12]	None
18	282.2791	15.43	C18H35NO	0.6	Oleamide	[M+H]+	0.957	5283387	301-02-0	[282.28, 265.25, 247.24, 97.1, 95.09]	None
19	284.2947	16.07	C17H37NO	1.8	1-desoxymethylsphinganine	[M-H2O+H]+	0.996	70678793	1219484-98-6	[284.29, 285.3, 102.09, 116.11, 284.22]	None
20	157.0499	2.44	C7H10O4	5.5	Isopropylfumaric acid	[M-H]-	0.989	6508102	7596-39-6	[157.05, 113.06, 95.05, 111.04, 113.05]	None
21	157.0497	2.69	C7H12O5	5.6	3-Isopropylmalic acid	[M-H-H2O]-	1	36	16048-89-8	[113.06, 157.05, 114.06, 156.89, 113.08]	None
22	157.0498	2.89	C7H12O5	5.4	2-Isopropylmalic acid	[M-H-H2O]-	0.998	77	3237-44-3	[113.06, 157.05, 114.06, 156.89, 158.08]	None
23	136.0393	3.63	C8H9NO4	7.5	(S)-3,5-DHPG	[M-H-CH2O2]-	0.985	443586	162870-29-3	[136.04, 94.03, 137.04, 109.02, 93.02]	None
24	173.0812	5.05	C8H14O4	5	Suberic acid	[M-H]-	0.997	10457	505-48-6	[111.08, 173.08, 129.09, 109.06, 112.08]	None
25	144.0445	5.83	C10H7NO3	6.9	4-(5-Oxazolyl)benzoic acid	[M-H-CO2]-	0.999	2776414	250161-45-6	[144.04, 145.05, 116.05, 144.02, 126.03]	None
26	187.097	6.35	C9H16O4	4	Azelaic acid	[M-H]-	0.998	2266	123-99-9	[125.1, 187.1, 97.06, 123.08, 126.1]	None
27	155.1068	7.22	C9H16O2	6.3	4-Methylcyclohexaneacetic acid	[M-H]-	0.999	3616945	6603-71-0	[155.11, 156.11, 155.14, 155.07, 137.1]	None
28	279.0874	7.77	C10H20N2O3S2	10.8	Met-Met	[M-H]-	0.977	6993083	7349-78-2	[279.09, 176.08, 235.1, 173.1, 191.11]	Into_Blood
29	215.1284	9.18	C11H20O4	2.8	Undecanedioic acid	[M-H]-	0.966	15816	1852-04-6	[215.13, 197.12, 153.13, 216.13, 198.12]	None
30	239.1649	9.41	C14H26O4	1.2	Tetradecanedioic acid	[M-H-H2O]-	0.999	13185	821-38-5	[239.16, 195.18, 139.11, 240.17, 238.89]	None
31	314.1762	12.65	C19H25NO3	0.2	2-Benzyl-4-(octahydro-2H-isoindol-2-yl)-4-oxobutanoic acid	[M-H]-	0.873	3047758	145324-16-9	[314.18, 176.03, 230.08, 188.03, 191.06]	Into_Blood

3.3.2.Hericenone C can enter the bloodstream in its original form

In the positive ion mode, HEC and PHEC were extracted for m/z 571.3999, and their extracted ion chromatogram (XIC) and MS/MS are shown in Figure 13. No related substances were detected in the negative ion mode. From the figure, it can be seen that HEC is detected in PHEC, with retention time and several key secondary ion fragments matching the standard.

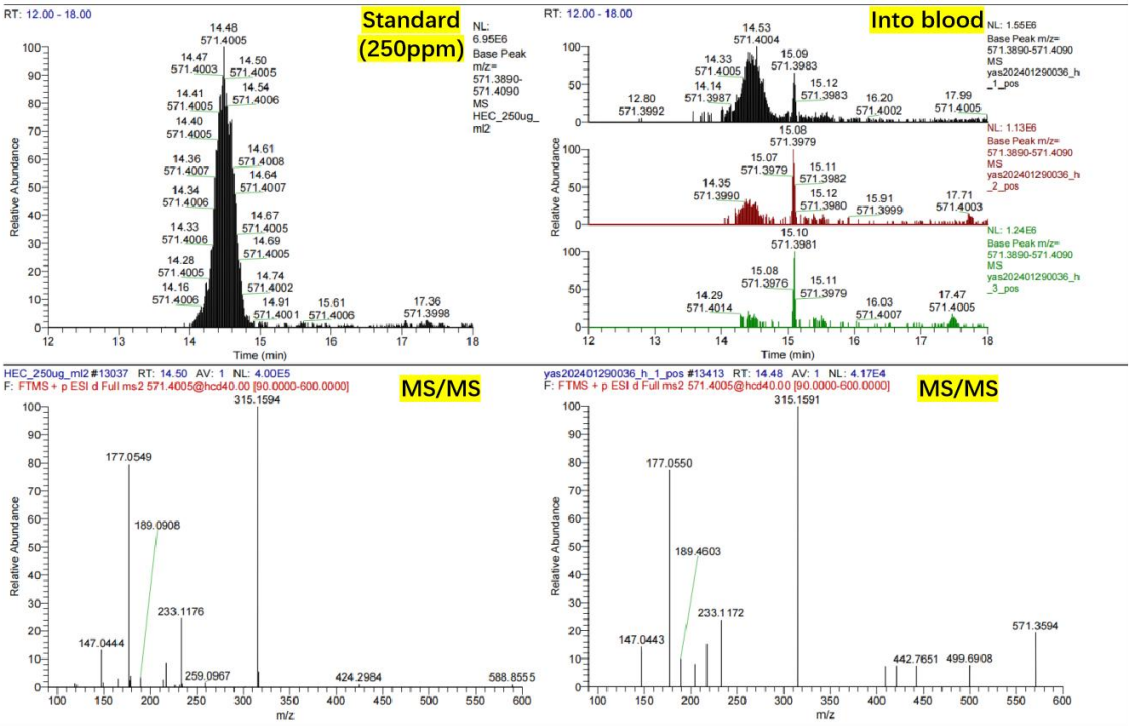

Figure 13. HEC and PHEC's XIC and MS/MS in positive ion mode.

The XIC and MS/MS of HEC in the blood of the CON+HEDE group in the positive ion mode for m/z 571.3999 are shown in. It can be seen from the figure that HeC has a low concentration in HEDE and there are high interfering peaks near the peak, while no detection was found in both CON and PHEDE.

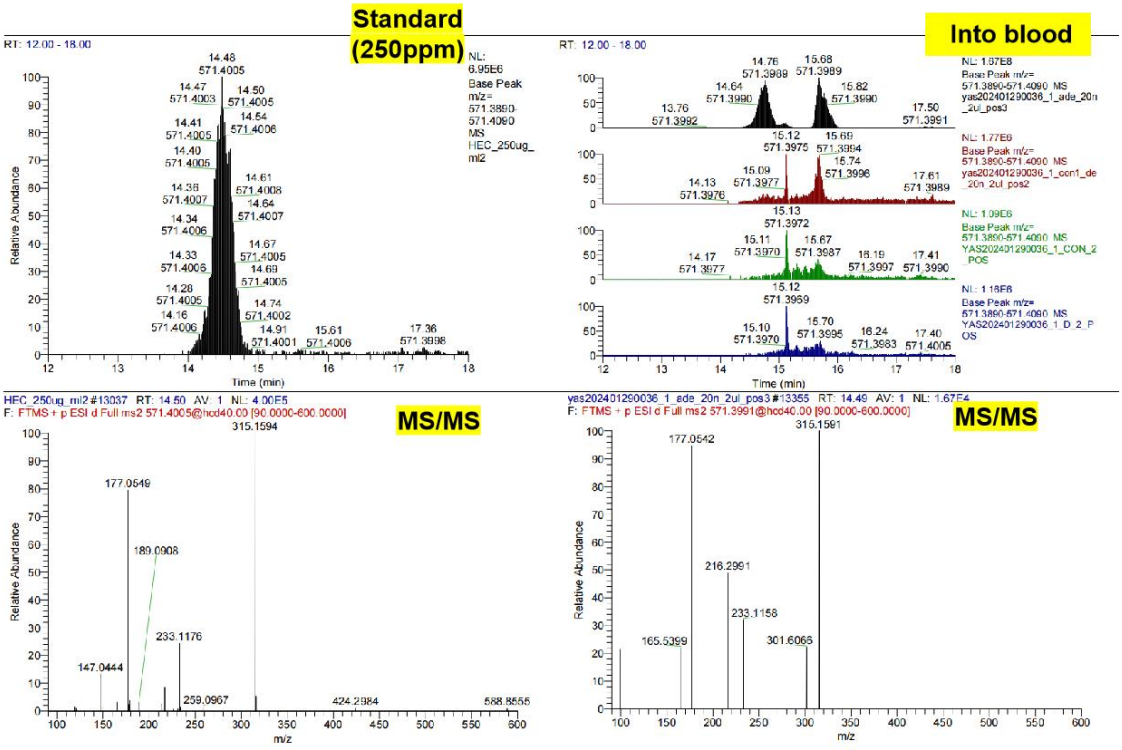

Figure 14. HEC, HEDE, CON, and PHEDE's XIC and MS/MS in positive ion mode.

3.4.Conclusion

In this chapter, we performed a plasma pharmacochemical study on the blood of mice continuously gavaged with HEDE or hericenone C for seven days, and the results of LC-MS/MS analyses revealed the chemical composition of HEDEand listed 31of them as known compounds of high abundance. The metabolomics results showed that eight of these high-abundance compounds can enter the bloodstream in a form that is not metabolized, facilitating our understanding of the possible contributors to the biological activity of HEDE. On the other hand, we found that hericenoneC can enter the bloodstream in a form that is not metabolized, suggesting that it may be transported by the bloodstream to target organs to act. These findings provide a foundation for understanding and conducting subsequent bioactivity assays.

Chapter 4 Study on Anti-inflammatory activity of HEDE based on metabolomic analysis and network pharmacological research

4.1.Introduction

COVID-19, caused by SARS-CoV-2, has been linked to severe respiratory complications, including ALI and acute respiratory distress syndrome (ARDS) [141,142] . The relationship between COVID-19 and these severe lung conditions is characterized by a complex interplay of inflammation and immune responses [143,144] . SARS-CoV-2 infection can trigger a severe systemic inflammatory response, primarily due to the production of pro-inflammatory cytokines like IL-6, TNF, and IL-1β. This surge in cytokines can enhance lung permeability, facilitating the spread of the virus and the entry of immune cells, which in turn can intensify lung inflammation and lead to ALI and ARDS [145] . In the post-pandemic era, COVID-19 has become a part of our lives. *H. erinaceus* has the effects of enhancing immunity and anti-inflammation, which is of great value for preventing inflammation in our daily lives.

Network pharmacology offers a novel perspective by examining the synergistic relationships among multiple active components, target genes, and pathways. This systems biology approach is particularly valuable for natural products, which often consist of multiple ingredients [146] . By mapping out the intricate web of interactions between these components, network pharmacology provides a reliable method to uncover the mechanisms of action and potential synergies or antagonisms [147,148] . The integration of network pharmacology and plasma pharmacochemistry offers new methods for drug development and research on natural products, revealing the multi-target mechanisms of action of drugs[149,150].

In this study, we aim to integrate plasma pharmacochemistry with network pharmacology to dissect the complex pharmacological profiles of HEDE components. By performing LPS-induced mice ALI model, evaluating HEDE's anti-inflammatory

activity, coupled with network pharmacology for systems-level analysis, we seek to advance our understanding of therapeutic actions of HEDE to ALI and lung inflammation. This provides a scientific basis for the development of HEDE into related functional foods.

4.2.Experimental

4.2.1.Animal experiment

Adult male C57BL/6 mice, weighing between 20 to 22 grams, were sourced from Jiangsu Huachuang Sino Medical Technology CO., Ltd., China. Animal License Number: SCXK(SU)2020-0009. The animals were housed under conditions with regulated temperature, humidity, and appropriate lighting. After a seven-day adaptation period, in the experimental setup, the mice were randomly assigned to five distinct groups: a control group, a 250 mg/kg metformin (MET) group, and three treatment groups receiving 50mg/kg, 100mg/kg, and 200mg/kg of HEDE, respectively. The prophylactic administration was done intragastrically on a daily basis for a period of 7 days, the control group received an equivalent volume of physiological saline, during which body weight was measured every day. The LPS-induced ALI mice model is a classic model for research and screening of ARDS drugs and pharmacological mechanisms[151]. After pretreatment, 5 mg/kg LPS intratracheal instillation induced ALI, and 24 h after stimulation, mice were euthanized and lung tissues were collected (Figure 15).

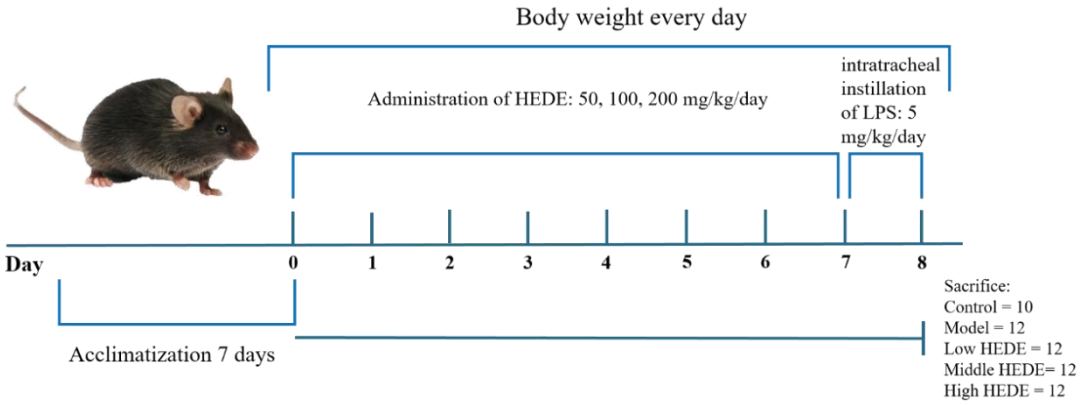

Figure 15. Workflow of animal experiment.

4.2.2.Histopathology analysis

The left lung tissues were harvested and preserved using a 10% formalin solution for a period of 24 hours. Subsequently, they were embedded in paraffin and subjected to hematoxylin and eosin (H&E) staining to visualize cellular structures. The degree of lung inflammation was quantified through an inflammation score, which reflects the intensity of the inflammatory response within the pulmonary tissue. Evaluation of the lung inflammation was conducted by a seasoned pathologist. For the microscopic examination, five randomly chosen fields from the stained slides were observed under an Olympus BX53 microscope at 200x magnification.

4.2.3.Network pharmacology research

4.2.3.1.Target prediction of active components

"Super-PRED" [152] (https://prediction.charite.de/index.php), a web-based tool, was employed to forecast the compound targets of a set of genes associated with HEDE. These compounds adopted components in HEDE obtained by plasma metabolomics analysis that could enter the blood. This server leverages the chemical resemblance of

pharmaceutical compounds to their respective molecular targets and the therapeutic implications stemming from similar properties. The process of target prediction involves scrutinizing the input compounds against an extensive database that encompasses roughly 341,000 compounds, spanning across 1,800 distinct targets, and encompassing 665,000 documented interactions between these compounds and targets. The outcomes of this analysis were subsequently cross-referenced with the "UniProt" (https://www.uniprot.org/) to validate the findings. Gene sets pertinent to ALI were identified through a comprehensive search on platforms such as "GeneCards" (https://www.genecards.org/), "DisGeNET" [153] (https://www.disgenet.org/home/), and "OMIM" [154] (https://omim.org/) utilizing search terms like "acute lung injury" and "acute respiratory distress syndrome". Upon obtaining the gene names, they were mapped to their corresponding UniProt IDs, and the final list of related target genes was compiled by merging and de-duplication the data. A new gene set is obtained by taking the intersection of the above two gene sets and used as the Targets of HEDE for treating ALI (THAs)

4.2.3.2.Network construction

THAs were imported into STRING (www.string-db.org/) and Cytoscape 3.7.2 for analysis and target acquisition. Utilizing the Bisogenet plugin in Cytoscape 3.7.2 software to conduct a protein-protein interaction (PPI) analysis between HEDE and THAs, followed by the application of the CytoNCA plugin to analyze the topological parameters of all nodes within the network, including degree centrality (DC), closeness centrality (CC), and betweenness centrality (BC). Key nodes within the network are identified by leveraging the concepts of network topology. Upload key THAs to the

David 6.8 (Database for Annotation, Visualization and Integrated Discovery, https://david.ncifcrf.gov/) database for gene function (GO, Gene Ontology) analysis to understand the main processes in which the targets are involved, including biological process (BP), cellular component (CC), and molecular function (MF). Utilize the "clusterProfiler" package in R language 3.6.3 for KEGG (Kyoto Encyclopedia of Genes and Genomes, https://www.kegg.jp/) enrichment analysis of the key targets, and use the "ggplot2" package to draw bubble charts.

4.2.4.Total RNA isolation and qRT-PCR analysis

RNA was isolated from cellular and tissue samples utilizing the RNA-Quick Purification Kit provided by YiShan Biotech, located in Shanghai, China. Following this, reverse transcription was carried out with the aid of the HiScript® II Q RT SuperMix kit, a product of Vazyme Biotech Co., Ltd from Nanjing, China. Quantitative real-time PCR (qRT-PCR) was executed with the ChamQTM SYBR® qPCR Master Mix (Low ROX Premixed), also supplied by Vazyme Biotech Co., Ltd. β-actin and GAPDH were served as an endogenous control for normalization, and the comparative quantification of gene expression was calculated using the ΔΔCt method. The specific primer sequences employed in this study are detailed in Table 10.

4.2.5.Statistical analysis

Results are presented as the average values accompanied by their standard deviations (S.D.). For statistical analysis, one-way ANOVA was initially utilized, supplemented by Tukey's test for assessing differences among multiple groups. Additionally, two-way ANOVA was employed, followed by Bonferroni's method for post-hoc comparisons. Statistical significance was determined using a p-value cut-off of less than 0.05.

Table 10. Primers used for real-time PCR.

Sprcies	Gene		Primer (5'-3')
Mouse	IL-1β	Forward	GCAACTGTTCCTGAACTCAACT
		Reverse	ATCTTTTGGGGTCCGTCAACT
	IL-6	Forward	TAGTCCTTCCTACCCCAATTTCC
		Reverse	TTGGTCCTTAGCCACTCCTTC
	TNF-α	Forward	GACGTGGAACTGGCAGAAGAG
		Reverse	TTGGTGGTTTGTGAGTGTGAG
	TLR4	Forward	GCTTTCACCTCTGCCTTCAC
		Reverse	GAAACTGCCATGTTTGAGCA
	NF-kB1	Forward	ACCTTTGCTGGAAACACACC
		Reverse	ATGGCCTCGGAAGTTTCTTT
	STAT3	Forward	CAGCAGCTTGACACACGGTA
		Reverse	AAACACCAAAGTGGCATGTGA
	HIF-1α	Forward	CCTGCACTGAATCAAGAGGTTGC
		Reverse	CCATCAGAAGGACTTGCTGGCT
	β-actin	Forward	GGCTGTATTCCCCTCCATCG
		Reverse	CCAGTTGGTAACAATGCCATGT
	GAPDH	Forward	GCATGGCCTTCCGTGTTC
		Reverse	GATGTCATCATACTTGGCAGGTTT

4.3.Results and discussion

4.3.1.HEDE relieves lung injury induced by LPS in mice

This experiment first assessed the therapeutic effect of HEDE on LPS-induced ALI in mice. Compared with the control group, there was no significant change in the body weight of mice after continuous gavage administration of HEDE for seven days, indicating that HEDE has no obvious toxicity to mice (Figure 16).

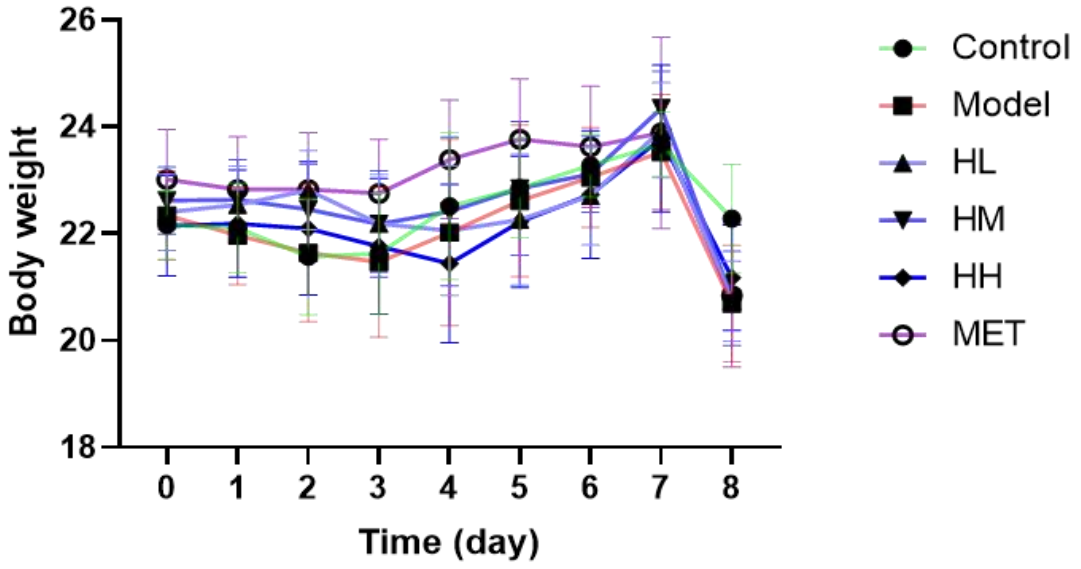

Figure 16. The change in body weight of mice over time. All data are presented as means ± S.D. *p < 0.05, **p < 0.01, ***p <0.001. HL: 50 mg/kg/day HEDE treatment group; HM: 100 mg/kg/day HEDE treatment group; HL: 200 mg/kg/day HEDE treatment group.

An initial assessment of lung tissue samples from the LPS-induced group revealed significant pathological changes, characterized by intense leukocytic infiltration,

alveolar septal thickening, pulmonary edema, and hemorrhagic areas. These conditions were notably reduced in mice that had been pre-treated with HEDE (Figure 17).

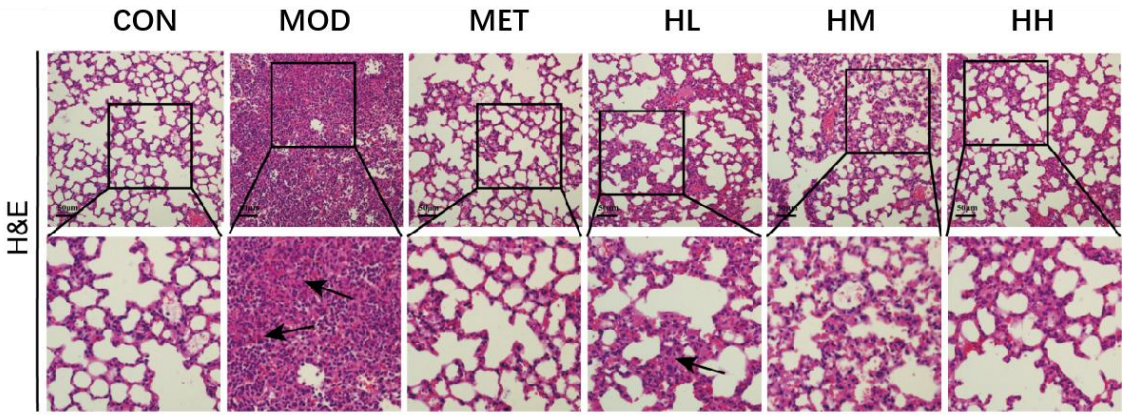

Figure 17. H&E stained pathological section plots. MET: 200 mg/kg/day metformin treatment group; HL: 50 mg/kg/day HEDE treatment group; HM: 100 mg/kg/day HEDE treatment group; HL: 200 mg/kg/day HEDE treatment group.

As shown in Figure 18A, a semi-quantitative method was applied to score lung injury, and we observed that LPS significantly increased the lung injury score, while HEDE pretreatment reduced the lung injury score. In addition, compared with the control group, the expression of IL-6, IL-1β, and TNF-α genes in the lung tissue of the model group rats increased. HEDE can inhibit the increase in IL-6, IL-1β, and TNF-α levels (Figure 18B-D). This indicates that HEDE improved LPS-induced lung inflammation.

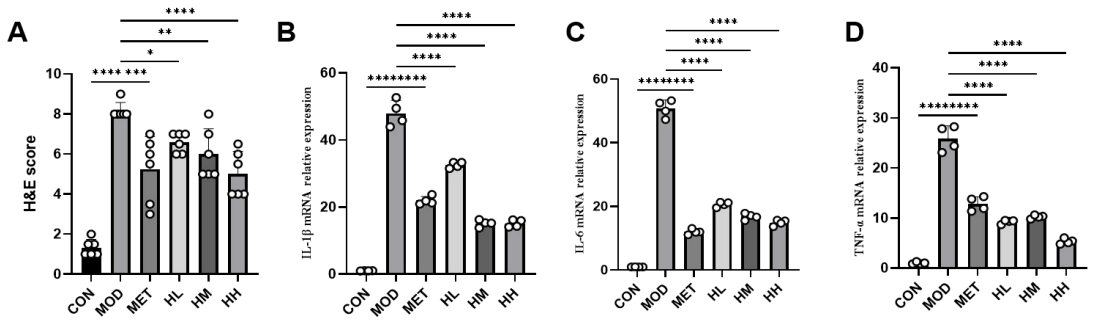

Figure 18. H&E score (A), IL-1β (B), IL-6 (C), and TNF-α (D) mRNA relative expression level. All data are presented as means ± S.D. *p < 0.05, **p < 0.01, ***p <0.001, ****p <0.0001. MET: 200 mg/kg/day metformin treatment group; HL: 50 mg/kg/day HEDE treatment group; HM: 100 mg/kg/day HEDE treatment group; HL: 200 mg/kg/day HEDE treatment group.

4.3.2.Network pharmacology research

Utilizing the "GeneCards", "DisGeNET", and "OMIM" databases, we screened genes related to ALI/ARDS, identifying a total of 613 genes. Based on the 8 compounds that could enter the blood in HEDE, we predicted 129 potential THAs from the "Super-PRED" database, with the screening criteria being Accuracy greater than 0.8 and probability greater than 0.7. By intersecting the two sets, we discovered 29 potential THAs for HEDE treatment of ALI (Figure 19A), and the interaction between compounds and targets is shown in Figure 19B.

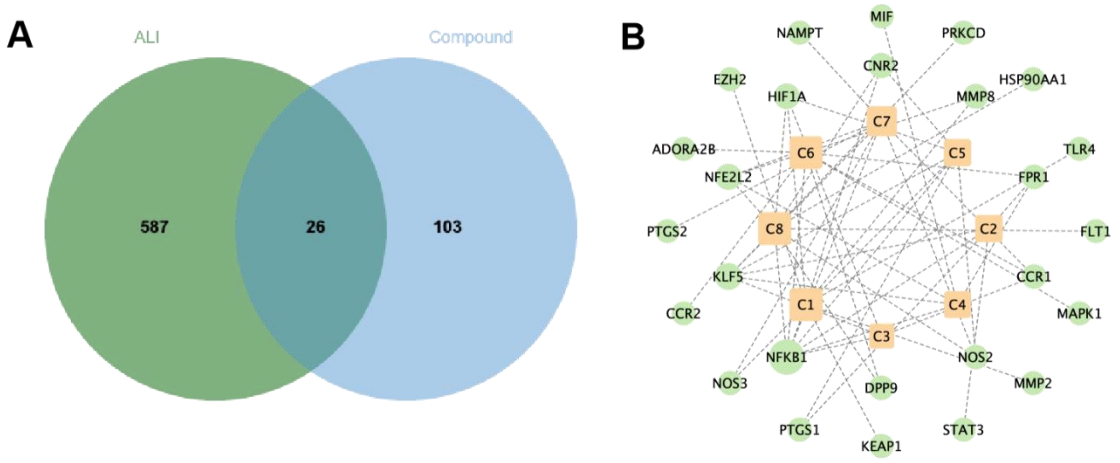

Figure 19. The intersection of compound targets set and disease targets set (A), and compound-target interaction network (B). C1-C8 represented the 8 components in HEDE that can enter blood.

After generating a PPI network for the 29 potential targets in the "STRING" database (Figure S50), we imported it into Cytoscape software for further visualization analysis. Subsequently, we conducted an enrichment analysis on these potential therapeutic targets. The GO analysis results showed that among the Biological Processes, these targets are involved in, the inflammatory response is the most prominent, followed by "positive regulation of vascular endothelial growth factor production," "positive regulation of tumor necrosis factor production," "angiogenesis," and "response to lipopolysaccharide," all of which are closely related to the inflammatory response (Figure 20). In the KEGG analysis, the HIF1 signaling pathway stands out, which is closely related to hypoxia caused by acute lung injury (Figure 21).

In network analysis, DC (degree centrality), CC (closeness centrality), and BC (betweenness centrality) typically refer to different measures or concepts that describe

the importance of nodes in a network or the structural characteristics of the network. These centrality measures are important tools in network analysis, helping us understand the structure and dynamics of networks, as well as the role and influence of nodes within them. By analyzing these centralities, key nodes in the network can be identified, which is crucial for screening for key gene nodes. Through topological analysis to generate PPI (DC, CC, and BC), we obtained key nodes in the network (Figure 22A-C), which are the key THAs, namely STAT3, TLR4, NFkB1, and HIF-1α.

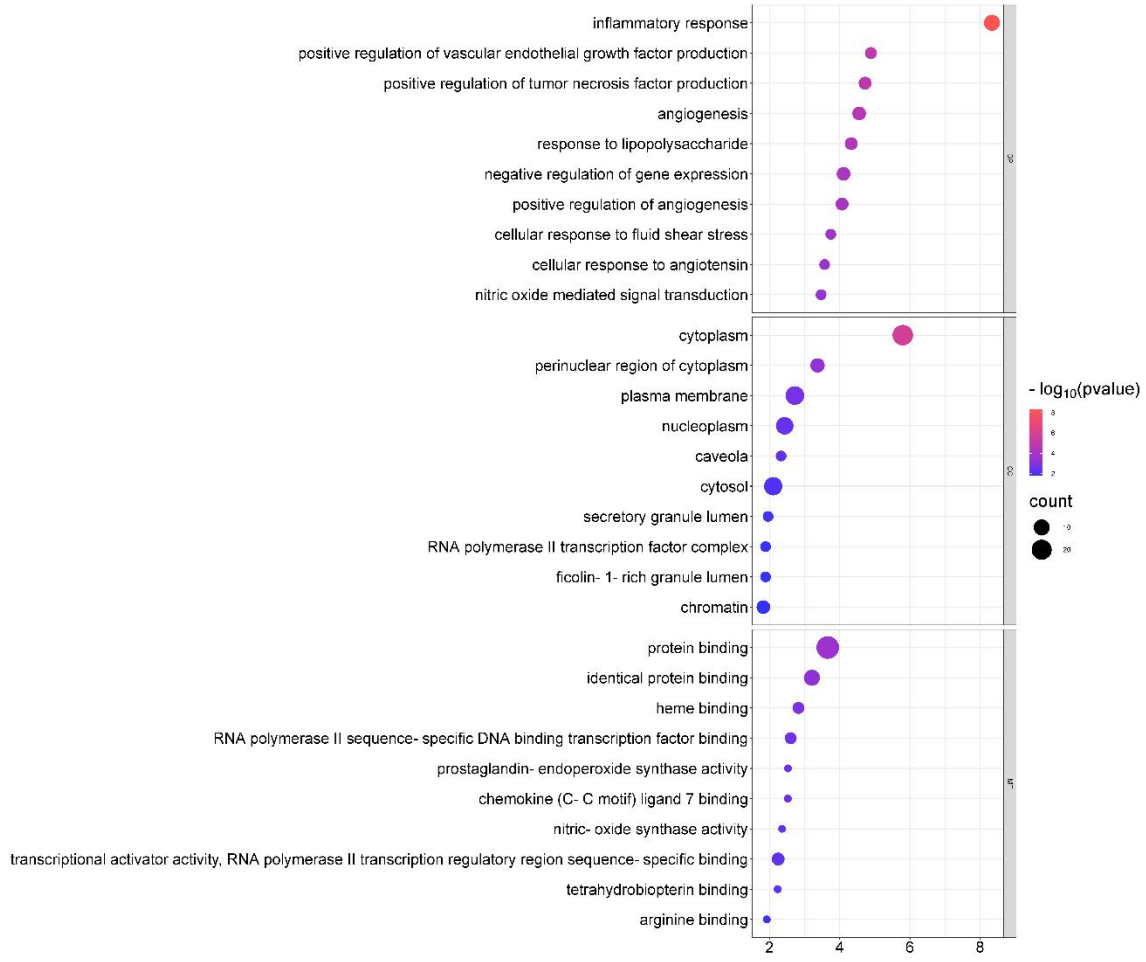

Figure 20. GO enrichment analysis of THAs. BP（Biological Process）: Represents biological processes, describing the biological processes or activities that gene products are involved in within an organism. CC（Cellular Component）: Represents cellular components, describing the location of gene products within a cell or the cellular structures they are part of. MF（Molecular Function）: Represents molecular functions, describing the functions or activities of gene products at the molecular level. The size of the bubble represents the number of genes enriched to that item and the color range represents its significance.

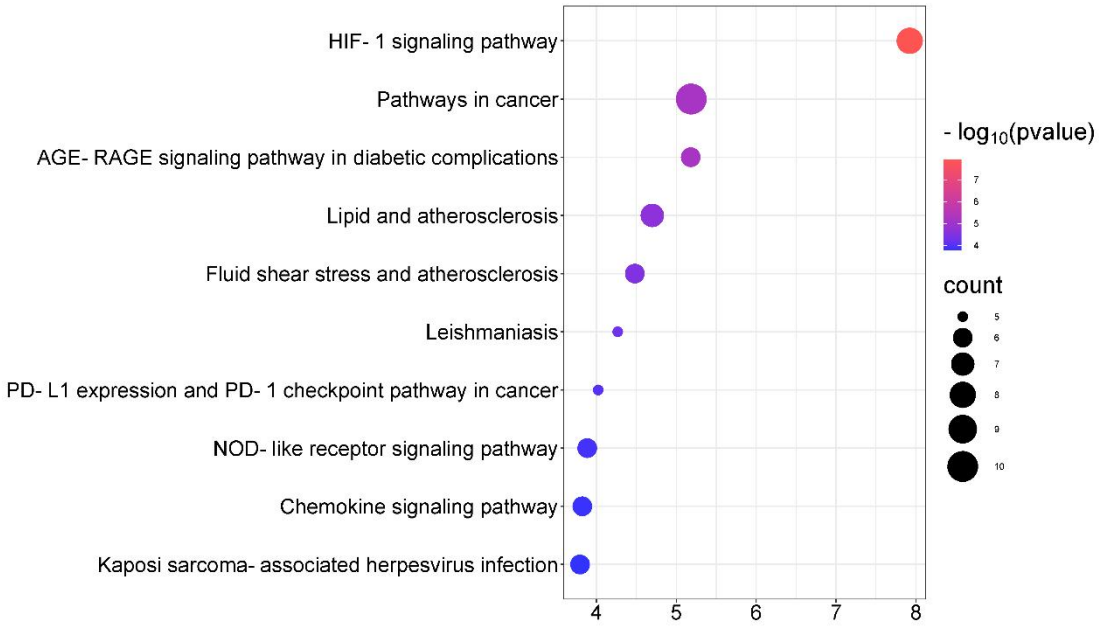

Figure 21. KEGG enrichment analysis of THAs. The size of the bubble represents the number of genes enriched to that item and the color range represents its significance.

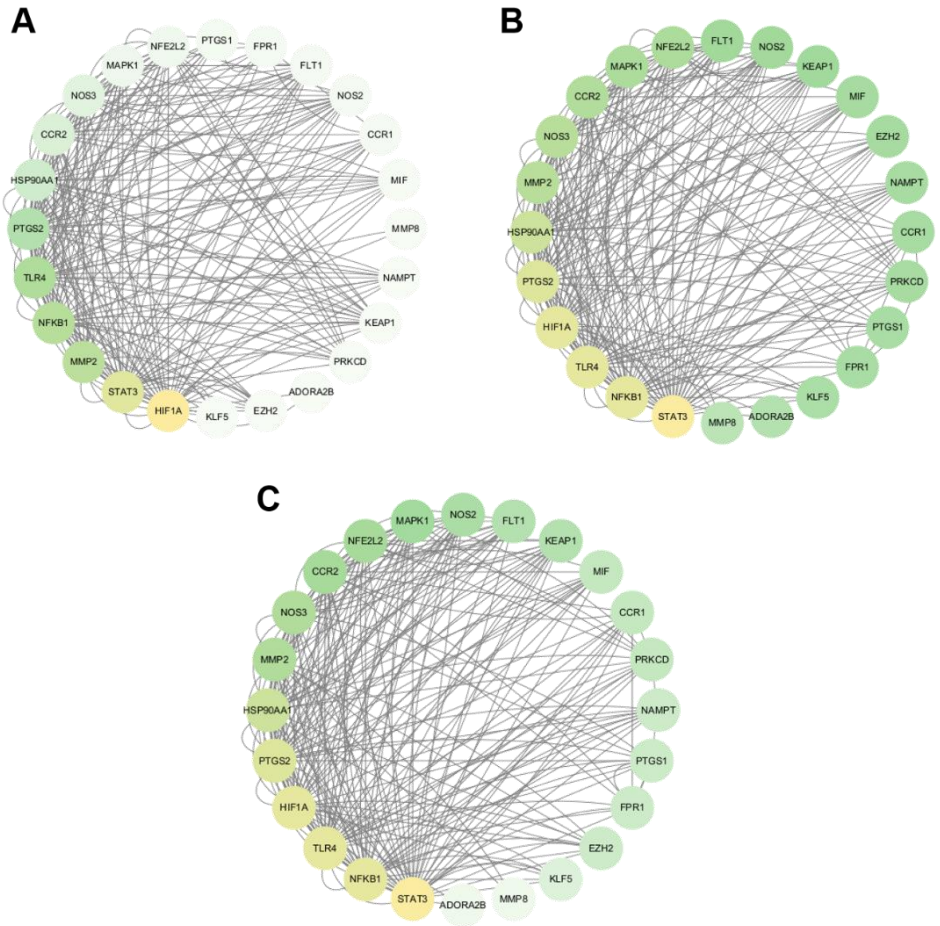

Figure 22. PPI network analysis under the topological parameters of degree centrality (DC), closeness centrality (CC), and betweenness centrality (BC). Degree centrality is a measure of the importance of a node in a network based on the number of its neighbors. The higher the degree centrality of a node, the more directly connected it is to other nodes in the network; Closeness centrality measures how close a node is to all other nodes in the network. The higher the closeness centrality of a node, the shorter the average path length to other nodes; Betweenness centrality measures the ability of a node to control the flow of information in a network. A node with high betweenness centrality is on many of the shortest paths in the network.

4.3.3.HEDE can regulate HIF-1α pathway to reduce LPS-induced inflammation

Based on the results of the pathological slice evaluation and scoring as well as inflammatory indicators, we selected the dose of HH (200mg/kg) for subsequent research in the following experiments.

The analysis results of network pharmacology indicate that the HIF1 pathway is an important pathway for HEDE to improve ALI inflammation, and TLR4, NFkB1, STAT3, and HIF-1α are important nodes in the molecular interaction network. According to previous research, LPS can activate TLR4, thereby activating NFkB1[155,156], and NFkB1 can further activate STAT3[157], and the activation of the above targets can upregulate the expression of HIF-1α[158,159].

Thus, we verified the targets screened by network pharmacology. The results showed that compared to the control group, the expression of the relevant targets in the model group was significantly upregulated, indicating that LPS triggered an inflammatory response by activating TLR4. TLR4 can promote the release of inflammatory factors such as IL-6, IL-1β, TNF-α, and MCP-1 by activating NF-κB. At the same time, TLR4/NFKB1 can activate STAT3 and HIF-1α to further exacerbate inflammation. In contrast to the model group, the expression of various genes in the HEDE treatment group was significantly downregulated, indicating that HEDE can alleviate the inflammatory response of acute lung injury through this pathway.

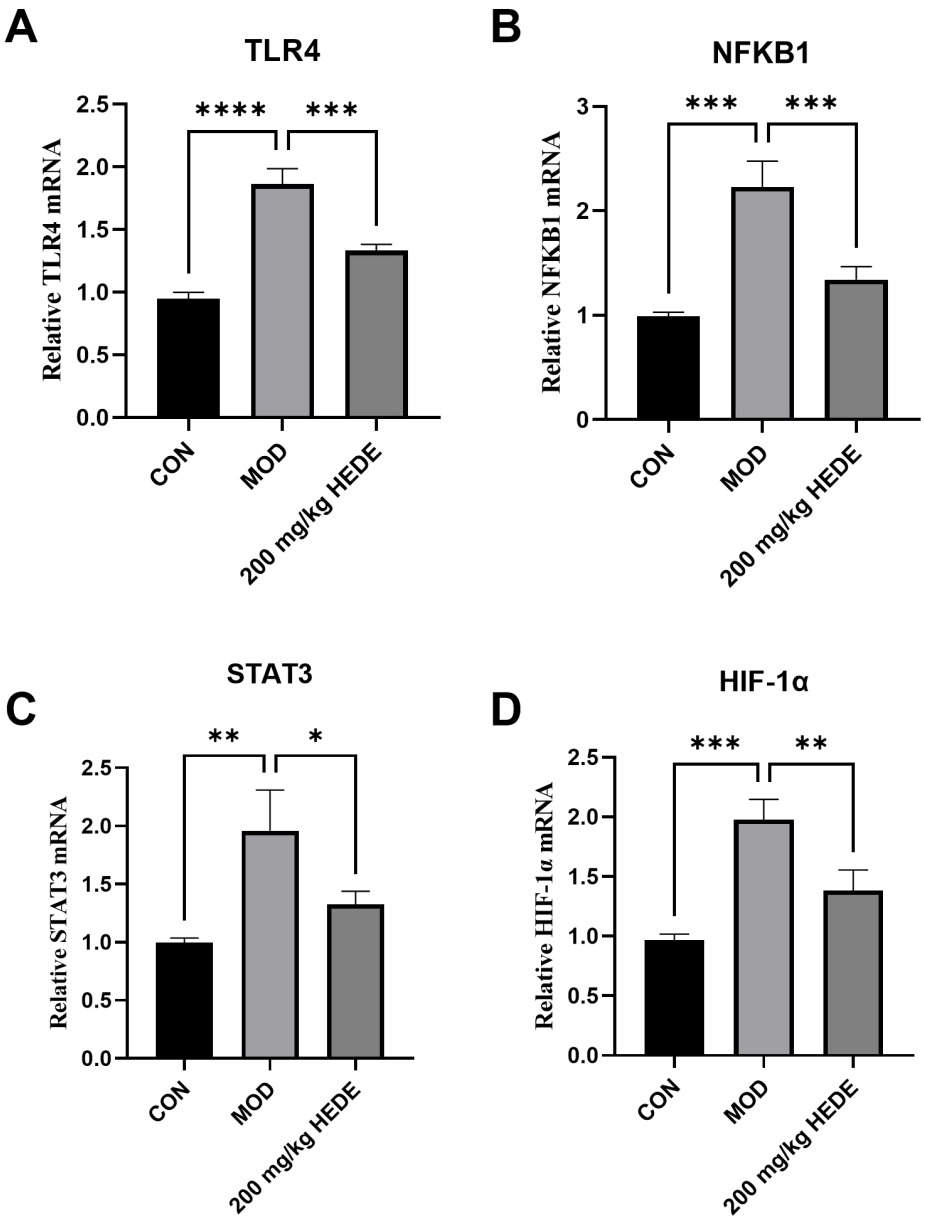

Figure 23. The expression of genes that obtained through the combined analysis of plasma pharmacochemistry and network pharmacology. (A) TRL4 mRNA relative expression. (B) NFkB1 mRNA relative expression. (C) STAT3 mRNA relative expression. (D) HIF-1α mRNA relative expression. All data are presented as means ± S.D. *p < 0.05, **p < 0.01, ***p <0.001, ****p <0.0001.

4.4.Conclusion

This chapter delves into the anti-inflammatory activity of HEDE, especially its application in the ALI model. Research findings indicate that HEDE, when pre-treated in a mouse model of ALI induced by LPS, exhibits a potent anti-inflammatory effect. Through methods such as histopathological analysis, real-time quantitative PCR, and statistical analysis, the study confirms the potential efficacy of HEDE in reducing lung injury and regulating the expression levels of related inflammatory factors.

Furthermore, by integrating the metabolomics analysis from the third chapter with network pharmacology, it was discovered that HEDE may ameliorate the inflammatory condition of ALI through the TLR4/NFKB1/STAT3/HIF-1α signaling pathway. This provides a scientific basis for the development of HEDE as a potential functional food.

Overall, this research offers new insights into the anti-inflammatory activity of HEDE as a natural product and provides valuable information for further functional food development and research. With these findings, we can better understand the potential applications of HEDE in the treatment of inflammatory diseases such as acute lung injury.

Chapter 5 Study on the neuroprotective activity of hericenone C based on bioinformatics analysis and molecular biology method

5.1.Introduction

Alzheimer's disease (AD) is a cognitive decline disorder that impacts over 50 million individuals globally, diminishing their autonomy and emerging as a top mortality cause with the aging demographic [160] . Predominantly affecting the elderly, AD's occurrence escalates approximately every five years post-65, making it the foremost dementia type, responsible for 50%–75% of dementia cases [161] . The aging process, a pivotal AD risk factor, leads to a buildup of senescent cells that can trigger persistent inflammation through the senescence-associated secretory phenotype (SASP)[162]. Telomeres, which are found at the chromosome termini, diminish in length with each cell division, thereby correlating closely with human aging and lifespan. Research in clinical settings has indicated that individuals afflicted with age-related conditions like Alzheimer's disease (AD) and cognitive decline exhibit reduced telomere lengths [163,164] . The connection between the aging process and the attrition of telomeres is widely acknowledged as a critical factor in the development of AD.

The manipulation of research data and the extraction of insights from the data have grown in importance in AD research. Several different approaches have been used to generate a vast amount of data in the medical and healthcare fields. Data mining research is necessary to extract vast volumes of diverse data [165] . Machine learning, a technique that lets computers learn and make predictions from data, has many applications in genetics and genomics. The machine learning approaches reported to date include supervised learning (classification and regression), unsupervised learning (clustering and dimensionality reduction), reinforcement learning (model-based and model-free), self-supervised learning (contrastive and generative), and more [166]. Typical examples are the use of 'enhanced directed random walk (EDRW)' for finding genes that

are related to different types of breast cancer based on gene expression data [167] , the classification of cancer types and the identification of driver genes based on a deep learning model, DeepCues [168] , and the utilization of 497 genes evaluated by LASSO regression as the basis for a low-cost machine-learning technique to predict early-onset preeclampsia [169] . We speculated that the application of a variety of machine learning methods could unmask the potential connections among AD, aging and telomeres, thus contributing to the identification of new ideas and directions for the diagnosis and treatment of AD.

Neurotrophins constitute a group of proteins that foster the survival and development of neurons. They stimulate growth and branching of nerve fibers, as well as the formation of dendrites, by selectively binding to specific tropomyosin-related kinase (Trk) receptors and the p75 neurotrophin receptor[170]. This interaction is crucial for the proper functioning and maintenance of the nervous system. The neurotrophin group in mammals includes several key members: NGF, brain-derived neurotrophic factor (BDNF), neurotrophin 3 (NT3), and neurotrophin 4/5 (NT4/5), as identified in various studies [171,172] . NGF consists of a chain of 118 amino acids and has been identified to interact with two distinct types of receptors: the high-affinity TrkA receptor and the low-affinity p75 neurotrophin receptor (p75NTR)[173]. NGF attaches to the p75 NTR, and in the presence of TrkA, this interaction can enhance neuronal survival, neurite elongation, and the formation of synapses [170] . NGF activates multiple signaling pathways, including the extracellular signal-regulated kinase (ERK), mitogen-activated protein kinases (MAPKs), to stimulate CREB (cAMP Response Element-Binding Protein) phosphorylation, which is essential for gene expression and neuronal survival [174,175] . NGF effects on aging, particularly in relation to neuronal health and

cognitive function, have been widely studied [176–179] . By querying databases related to telomeres (TelNet: http://www.cancertelsys.org/telnet/) and aging (Human Ageing Genomic Resources database (HAGR): http://hagr.ageing-map.org/index.php), the NGF/TrkA/ERK/CREB pathway is involved in both telomeres and aging.

Hericenones, a class of hydrophobic compounds found in the fruiting bodies of *H. erinaceus*. Among them, hericenone C, which has the highest content in its derivatives, has been reported to promote the synthesis of NGF in vitro [63,180] . Extract containing hericenones C and D have been shown to mitigate cognitive decline in aging mice[65]. We speculate that hericenone C may regulate targets related to growth and aging, thereby exerting its effects.

In summary, aging and telomeres are closely related to neurodegenerative diseases such as AD, and hericenone C may have the potential to regulate pathways related to these targets. Our goal is to study the ability of hericenone C to regulate telomere aging-related targets through bioinformatics analysis and molecular biology methods.

5.2.Experimental

5.2.1.The construction of $A\beta_{25-35}$-induced AD cell models and the protective effect of hericenone C

5.2.1.1.Cell culture and hericenone C treatment

The SH-SY5Y cell line was obtained from the American Type Culture Collection (ATCC) and maintained in a regulated setting at a temperature of 37°C and with 5% CO2 in a cell culture incubator. The cells were grown in a high-glucose Dulbecco's Modified Eagle Medium (DMEM) enriched with 10% Fetal Bovine Serum (FBS), as well as antibiotics including penicillin at a concentration of 100 μg/ml and streptomycin

at the same concentration.

SH-SY5Y cells were cultured in DMEM with serum for 12 hours to promote adhesion. To detect the toxicity of hericenone C to SH-SY5Y, the cells were plated in a 96-well plate and treated with FBS-free DMEM containing various concentrations of hericenone C (0.01, 0.1, 1, 10, 20, 50, 75, 100 μM) for 24 hours. Subsequently, after the removal of the medium, the CCK8 working solution (100 ul per well) was added to each well, and the optical density (OD) at 450 nm was measured using a microplate reader.

5.2.1.2.The construction of $A\beta_{25-35}$-induced AD cell model

The peptide amyloid beta (Aβ), recognized for its neurotoxic properties, is a key factor in the pathogenesis of AD, characterized by its excessive deposition within the brain[181]. Mitigating the detrimental effects of Aβ on mitochondria is deemed essential for attenuating the pathological manifestations in AD[182].

$A\beta_{25-35}$ peptide was from Peptide Institute, Inc. (Lot. 710504). For the purpose of aggregation induction, the $A\beta_{25-35}$ peptide was prepared in distilled water and subsequently subjected to a 3-day incubation period at a temperature of 37 °C[183,184].

To select the appropriate concentration of $A\beta_{25-35}$ treatment, SH-SY5Y cells were plated in a 96-well plate and cultured in DMEM with 10% FBS for 12 hours to facilitate adhesion. The cells were then treated with FBS-free DMEM containing 5, 10, 20, and 40 μM $A\beta_{25-35}$, with time points set at 6, 12, and 24 hours, respectively. Subsequently, after the removal of the medium, 100 μl of CCK8 working solution per well was added, and the OD at 450 nm was measured using a microplate reader.

5.2.1.3.$A\beta_{25-35}$-induced AD cell model treated by hericenone C

To assess the protective effect of hericenone C on $A\beta_{25-35}$-induced AD cell models,

SH-SY5Y cells were plated in a 96-well plate and cultured in DMEM with 10% FBS for 12 hours to promote adhesion. An FBS-free DMEM medium containing 5 μM $A\beta_{25-35}$ and hericenone C at concentrations of 0.01, 0.1, 1, 10, 20, 50, 75, and 100 μM was prepared and used to co-treat the cells for 24 hours. Subsequently, after the removal of the medium, 100 μl of CCK8 working solution per well was added, and the OD at 450 nm was measured using a microplate reader.

5.2.2.Bioinformatics mining of AD targets for telomere aging

5.2.2.1.Data source

Four microarray datasets pertinent to AD were procured from the Gene Expression Omnibus repository. The dataset GSE132903 was selected for detailed examination and encompasses a cohort of 98 non-demented individuals alongside 97 samples from the middle temporal gyrus of AD patients. The GSE33000 dataset comprises 157 controls free from dementia alongside 310 cortical tissue samples from AD patients. The GSE122063 dataset contains 44 control cortical tissues and 56 samples from AD patients. Lastly, the GSE106241 dataset includes 40 cortical tissue samples from AD patients. The latter three datasets were earmarked for the validation process.

The transformation of raw probe identifiers within the GEO datasets to gene expression profiles was executed via an R script. This script facilitated the retrieval of gene names associated with each probe from the respective platform's annotation file, followed by a conversion of these probe identifiers to their corresponding gene IDs, thereby finalizing the annotation process. The standardization of the gene expression data was achieved through the application of the “normalizeBetweenArrays” function from the “limma” R package.

5.2.2.2.AD-related differential expression aging genes screening

A total of 307 genes associated with human aging, known as aging-related genes (ARGs), were extracted from the HAGR database[185]. These were then cross-referenced with the gene list from the GSE132903 dataset, resulting in a subset of 285 overlapping genes. Utilizing the “limma” R package, a comparative analysis of gene expression was conducted on the matrix to discern aging-related differentially expressed genes (ARDEGs) between AD and non-AD groups. Significance for ARDEGs was determined using a p-value threshold of less than 0.05 and a log fold change criterion of greater than 0.25 on a log2 scale.

The differential expression of each identified ARDEG was subsequently visualized and scrutinized. A heatmap representation of the ARDEGs was constructed employing the “pheatmap” R package, while a volcano plot was created to illustrate the data using the “ggplot2” R package. To further elucidate the biological significance of these ARDEGs, GO and KEGG pathway analyses were performed with the “clusterProfiler” R package. The GO enrichment analysis was segmented into three categories—BP, CC, and MF—to explore the biological roles and pathways in which the ARDEGs are enriched.

5.2.2.3.AD-related differential expression telomere genes screening

A total of 2093 genes related to human aging were extracted from the TelNet database, referred to as Telomere-Related Genes (TRGs). These genes were then cross-referenced with the gene list from the GSE132903 dataset, yielding a subset of 1886 overlapping genes. Using the "limma" R package, a comparative analysis of gene expression was conducted on the matrix to identify Telomere-Related Differentially Expressed Genes (TRDEGs) between the AD and non-AD groups. Significance for TRDEGs was

determined with a p-value threshold of less than 0.05.

5.2.2.4. Telomere-related genes associated with Aging

We conducted an analysis of the expression profiles of ARDEGs utilizing the "ConsensusClusterPlus" R package, implementing a k-means clustering approach with Euclidean correlation distance[186]. The parameter for the maximum number of potential subtypes, denoted by k, was established at 6. The determination of the optimal cluster number was facilitated by the examination of the cumulative distribution function curve, the consensus matrix, and the consensus clustering score, achieved through 2000 iterations of 80% sample resampling. To elucidate the distinctions in transcriptome profiles among gene clusters, we employed t-SNE dimensionality reduction technique and the 'Rtsne' R package.

Employing the "WGCNA" R package, we executed an identification process for co-expression modules, selecting an optimal soft power threshold to construct a weighted adjacency matrix [187] . This matrix was subsequently transformed into a topological overlap matrix (TOM). The generation of modules was contingent upon the TOM dissimilarity measure, calculated as (1 - TOM), and was executed using hierarchical clustering with a minimum module size criterion of 100. Each resultant module was randomly assigned a distinct color. The eigengene of each module encapsulated the comprehensive gene expression profiles. The measure of modular importance elucidated the correlation between the modules and the pathological state. The gene significance quantified the linkage between individual genes and clinical attributes. Applying the WGCNA algorithm, we dissected a dataset comprising 195 samples, delineated into 97 instances of Alzheimer's Disease (AD) and 98 control

subjects, as well as a subset of 97 AD samples categorized into Cluster A with 50 individuals and Cluster B with 47. From the module with the most pronounced association to the disease trait, as indicated by the WGCNA output, we extracted hub gene sets characterized by elevated gene significance (GS > 0.5) and module membership (MM > 0.5). The intersection of these gene sets facilitated the identification of 10 critical TRGs.

5.2.2.5.Machine learning model construction

Employing the "caret" R package, we engaged four distinct machine learning methods to discern TRGs with the strongest correlation to AD: the random forest (RF), the generalized linear model (GLM), the gradient boosting model (GBM), and the support vector machine (SVM). Within our analyses, the AD status was designated as the dependent variable, with the 10 TRGs, as identified through the WGCNA screening process, serving as the independent variables. The dataset of 195 samples was randomly partitioned into a training subset, constituting 70% of the data, and a validation subset, comprising the remaining 30%. The "caret" R package facilitated a grid search to dynamically optimize the model parameters, with all four models operating under their default settings. Subsequently, the "DALEX" R package was implemented to graphically represent the residual distribution for each of the four models, alongside the root mean square error (RMSE) following permutations of pivotal variables. The dataset underwent rigorous calibration through fivefold cross-validation, repeated 400 times, and iterated machine learning, executed 2,000 times, to refine the outcomes. Finally, the "Proc" R package was utilized to delineate the receiver operating characteristic (ROC) curve and to calculate the area under the curve (AUC) values, offering a visual

assessment of model performance. Finally, we proceeded to perform an analysis on the datasets GSE33000 and GSE122063 to ascertain the diagnostic efficacy of the model.

5.2.2.6.Validation of external datasets

Nomogram models, grounded in multivariate analysis, extensively integrate the outcomes of logistic or Cox regression to prognosticate the risk of specific clinical events in patient populations, complemented by illustrative graphical representations. In our study, we harnessed the “rms” R package, incorporating three TRGs, to evaluate the incidence of AD and its subtypes through a nomogram model. Each predictive factor within the model is assigned a score, with the aggregate score being the cumulative tally of the individual factor scores. To gauge the model's predictive accuracy, we employed a calibration curve and conducted a decision curve analysis (DCA), which serves as a metric for the model's prognostic utility in clinical decision-making.

Employing the “neuralnet” R package, we constructed artificial neural networks (ANNs) based on the three TRGs to ascertain the presence of AD and its subtypes. The architecture of the model included an intermediary hidden layer comprising five nodes. Subsequently, the “pROC” R package was utilized to graphically depict the ROC curves and the corresponding AUC values for each gene, thereby facilitating an assessment of the

model's diagnostic accuracy.

5.2.3.The investigation of the mechanism underlying the neuroprotective effect of hericenone C

5.2.3.1.Total RNA isolation and qRT-PCR analysis

RNA was isolated from cellular and tissue samples utilizing the RNA-Quick Purification Kit provided by YiShan Biotech, located in Shanghai, China. Following this, reverse transcription was carried out with the aid of the HiScript® Ⅱ Q RT SuperMix kit, a product of Vazyme Biotech Co., Ltd from Nanjing, China. Quantitative real-time PCR (qRT-PCR) was executed with the ChamQTM SYBR® qPCR Master Mix (Low ROX Premixed), also supplied by Vazyme Biotech Co., Ltd. GAPDH served as an endogenous control for normalization, and the comparative quantification of gene expression was calculated using the ΔΔCt method. The specific primer sequences employed in this study are detailed in Table 11.

Table 11. Primers used for real-time PCR.

Species	Gene		Primer (5’-3’)
Human	MCM7	Forward	CCTACCAGCCGATCCAGTCT
		Reverse	CCTCCTGAGCGGTTGGTTT
	HMGN5	Forward	AAAGAAAGGCTGCAGGTG
		Reverse	GTAAAGGGCACAGGCATAG
	CERS1	Forward	CAATGTGGGCATCCTTGTGCT
		Reverse	AGTAGAGGCGGAACCAGAAC
	NGF	Forward	CAACAGGACTCACAGGAGCA
		Reverse	CTCTCCCAACACCATCACCT
	GAPDH	Forward	CTGGGCTACACTGAGCACC
		Reverse	AAGTGGTCGTTGAGGGCAATG

5.2.3.2.Western blotting

Western blot assay for SH-SY5Y cells (n = 3 per group). SDS-polyacrylamide gel electrophoresis (SDS-PAGE) is performed for electrophoresis. Accurately take 5.00 μL of protein sample with a pipette and add it to the sample wells. Add electrophoresis buffer to the electrophoresis tank, set the voltage to 80 V first, and once the sample has run out of the upper gel, increase the voltage to 120 V until the protein runs to about 1 cm from the bottom edge of the gel, then turn off the power. After removing the gel, use a PVDF membrane with a pore size of 0.22 μm or 0.45 μm for the transfer operation. The PVDF membrane should be soaked in methanol for 1-2 minutes before use and then transferred to the transfer buffer. The transfer assembly (negative to positive pole) should be clamped in the order of sponge/filtration paper/gel/membrane/filtration paper/sponge, placed into the transfer tank, and the transfer buffer is added. The transfer is performed at a current of 200 mA for 90 minutes (the transfer time can be extended accordingly with the increase of the target protein molecular weight). After the transfer is complete, take out the PVDF membrane and place it in the blocking solution for blocking. After the blocking, seal the diluted antibody and the blocked PVDF membrane in a heat-sealable film, and incubate overnight at 4°C with primary antibodies. After the primary antibody incubation is finished, wash the membrane with TBST buffer by shaking 5 times, each for 5 minutes, to remove the residual primary antibody, then add the diluted secondary antibody and incubate for 1 hour at 37°C. Development: After the secondary antibody incubation is finished, wash the membrane with TBST buffer by shaking 5 times, each for 5 minutes, to remove the residual secondary antibody, then use an enhanced chemiluminescence (ECL) detection kit, and

collect the image through the developer.

5.2.4.Statistical analysis

The statistical evaluations were executed utilizing R software, specifically version 4.2.1, in conjunction with the visualization tool RAWGraphs. The computational tasks were powered by a CPU equipped with an AMD Ryzen™ 5 5600X processor. For the presentation of continuous variables, the standard error of the mean was applied, and these variables were subjected to comparative analysis via Student's t-test for normally distributed data or the Wilcoxon rank sum test for non-normally distributed data. The comparison of categorical data was performed using the $\chi 2$-test. Statistical evaluations were conducted using one-way ANOVA complemented by Tukey's post-hoc test for multiple comparisons. The threshold for statistical significance was established at a p-value of less than 0.05, with the significance levels represented by asterisks: * for $p<0.05$, ** for $p<0.01$, *** for $p<0.001$, and **** for $p<0.0001$.

5.3.Results and discussion

5.3.1.Effect of hericenone C on cell viability

5.3.1.1.Hericenone C treatment increased the cell viability of SH-SY5Y cells

This section of the study first assessed the impact of hericenone C treatment at different concentrations on the viability of SH-SY5Y cells after 24 hours. The CCK8 results showed that when the concentration of hericenone C reached 1 μM, the cell viability of SH-SY5Y cells increased significantly ($p<0.05$), and it exhibited a significant promoting effect on SH-SY5Y cells (Figure 24).

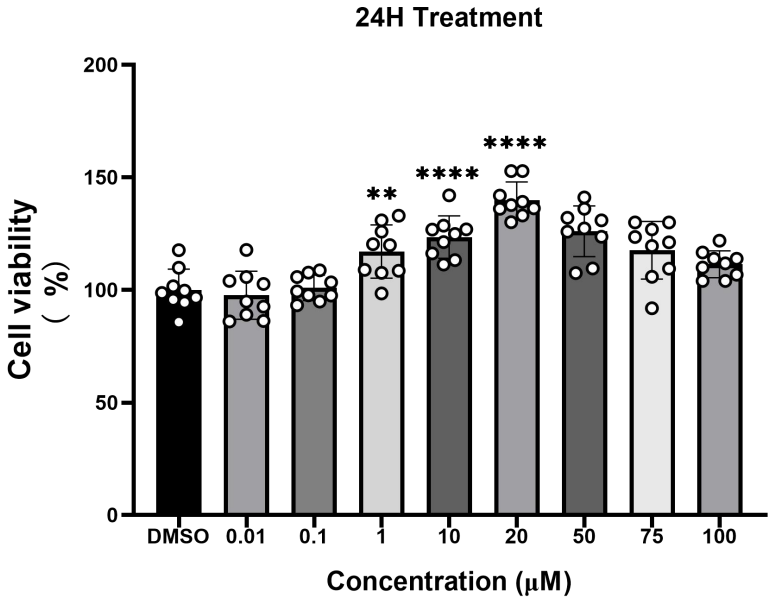

Figure 24. Effect of hericenone C treatment on the viability of SH-SY5Y cells. All data are presented as means ± S.D. *p < 0.05, **p < 0.01, ***p <0.001, ****p <0.0001.

5.3.1.2.Hericenone C can reduce $A\beta_{25-35}$-induced SH-SY5Y cell death

Before evaluating the protective effect of hericenone C on the $A\beta_{25-35}$-induced AD model, we screened the concentration of the modeling agent $A\beta_{25-35}$ and the induction time. The results indicated that the selected concentration and time could significantly reduce the cell activity of SH-SY5Y. To maintain consistency with the treatment time of hericenone C, we chose a 24-hour treatment of SH-SY5Y cells with 5 μM $A\beta_{25-35}$ as the final model (Figure 25).

Finally, we evaluated the protective effect of hericenone C treatment on the $A\beta_{25-35}$-induced AD model. The results showed that when the concentration of hericenone C reached 0.1 μM, the cell viability of SH-SY5Y cells increased significantly ($p<0.05$), and it demonstrated a significant protective effect on SH-SY5Y cells (Figure 26).

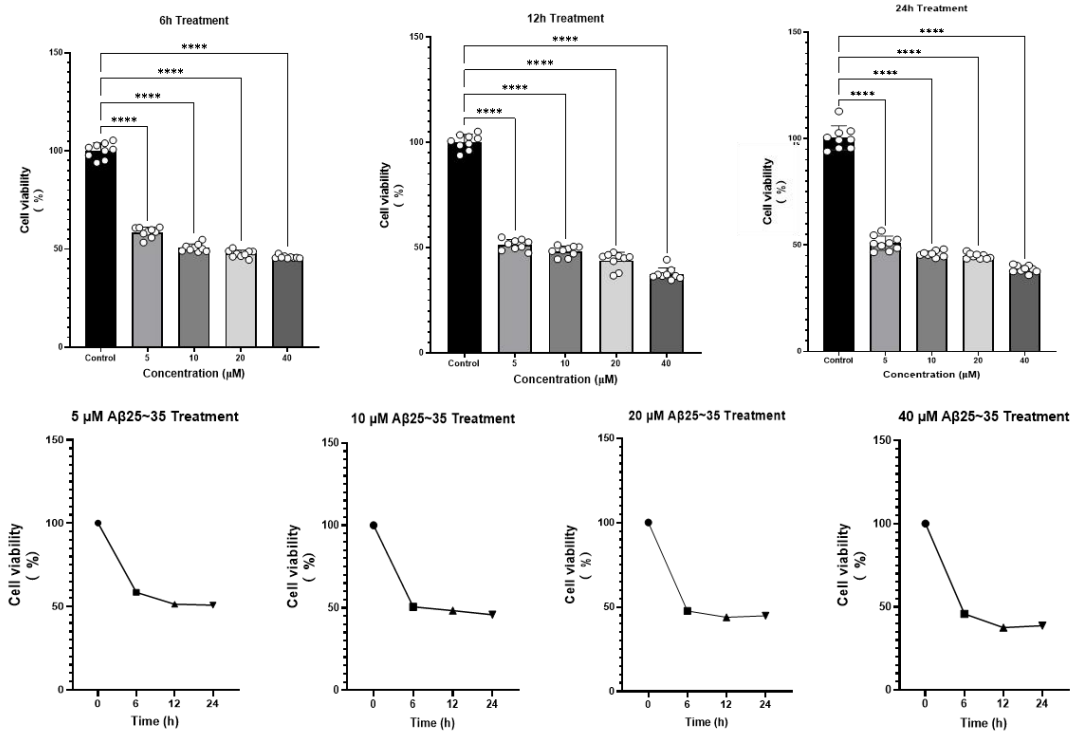

Figure 25. Screening for $A\beta_{25-35}$ treatment concentration and time. All data are presented as means ± S.D. *p < 0.05, **p < 0.01, ***p <0.001, ****p <0.0001.

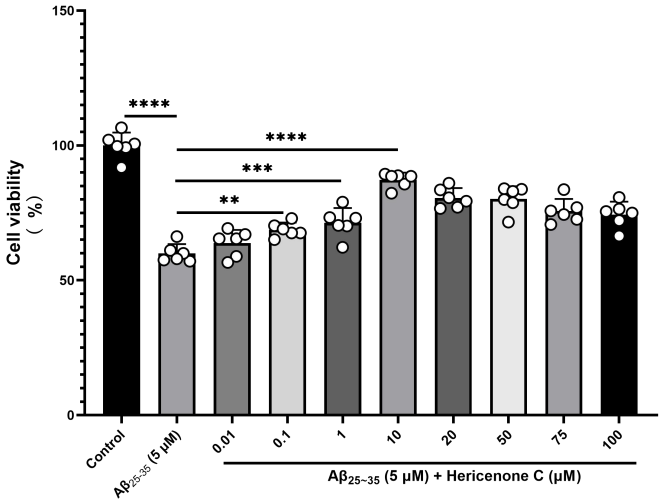

Figure 26. Effect of hericenone C on the viability of SH-SY5Y cells treated with $A\beta_{25-35}$. All data are presented as means ± S.D. *p < 0.05, **p < 0.01, ***p <0.001, ****p <0.0001.

5.3.2.Bioinformatics identified telomere aging targets

5.3.2.1.Identification of ARDEGs and TRDEGs

We sourced a collection of genes associated with aging from the HAGR database. Expression data for 285 genes were derived from the GSE132903 dataset, which was then utilized to formulate a matrix representing the expression patterns of aging-related genes. Through differential expression analysis comparing 97 individuals with AD and 98 without AD, we identified 40 ARDEGs, comprising 23 that were upregulated and 17 that were downregulated (Figure 27A＆B).

Furthermore, we procured a set of telomere-associated genes from TelNet and gathered expression data for 1,886 genes from the same GSE132903 dataset to create a matrix for TRGs. Given the typically low log fold change values observed in this dataset, the analysis primarily focused on the P-values. In the comparison of differential expression profiles between the 97 AD patients and 98 non-AD controls, we recognized a total of 1,142 differentially expressed genes, with 590 being upregulated and 552 being downregulated (Figure 27C＆D).

Based on previous literature research, we inquired whether the NGF-related pathways exist in the databases, and the results are shown in Table 12. Considering the typical log fold change values observed in this dataset, we used a P-value of less than 0.5 as the criterion for significance. It can be found that genes related to NGF, TrkA, ERK, and CREB can all be found in databases related to telomeres and aging, and the related genes all show significant differences in the AD dataset. This indicates a strong correlation between this pathway and telomeres and aging in AD.

Table 12. Genes of NGF-related pathways in aging and telomere databases and expression in GSE132903 dataset.

Genes	P.Value	Source
NGF	0.02164	HAGR
TrkA (NTRK1)	0.00929	TelNet
MAPK1 (ERK2)	4.17×10^{-6}	TelNet
MAPK3 (ERK1)	1.36×10^{-6}	TelNet/HAGR

CREBBP	2.71×10^{-5}	TelNet/HAGR
CREB1	1.10×10^{-7}	HAGR

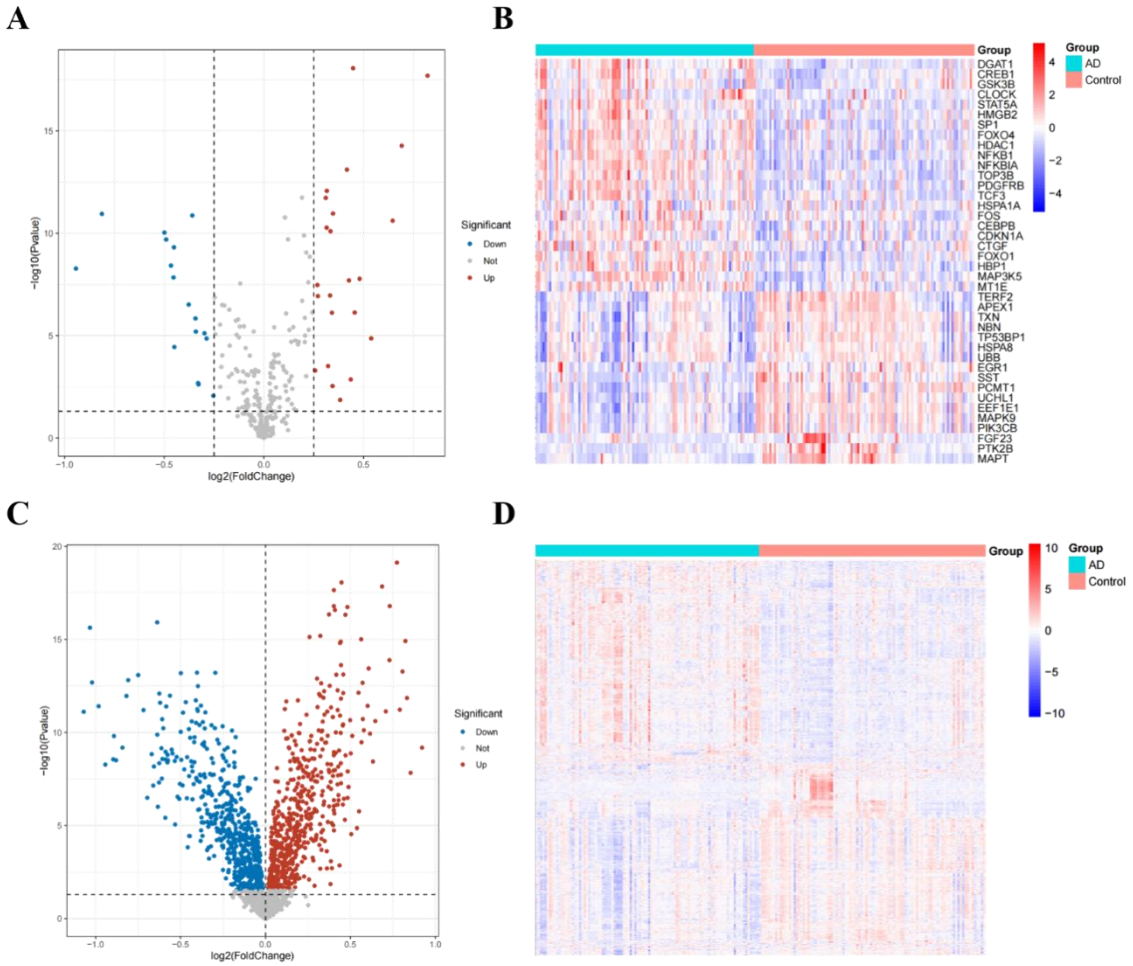

Figure 27. Identification of ARDEGs and TRDEGs implicated in the regulation of AD. (A) Volcano map of screened ARDEGs. (B) The heatmap depicted the expression patterns of 40 ARDEGs. (C) Volcano map of screened TRDEGs. (D) The heatmap depicted the expression patterns of 1142 TRDEGs.

5.3.2.2.Consensus clustering of AD patients

We employed a consensus clustering method to categorize the 97 AD samples into distinct groups, based on the expression patterns of the 40 ARDEGs, aiming to gain a deeper comprehension of the aging-associated expression dynamics within AD. The optimal number of clusters was determined to be two (k=2), as indicated by the most stable configuration (Figure 28A) and the least fluctuation in the cumulative distribution function (CDF) curves across all k-values (Figure 28B). The CDF curves' AUC highlighted the disparities between consecutive k-values (Figure 28C). Moreover, at k=2, each cluster achieved a consistency score exceeding 0.9 (Figure 28D).

With these findings, we segregated the 97 AD patients into two groups, Cluster A with 50 individuals and Cluster B with 47 individuals, guided by the heatmap of the consensus matrix. The t-distributed Stochastic Neighbor Embedding (tSNE) analysis revealed significant distinctions between these clusters (Figure 28E).

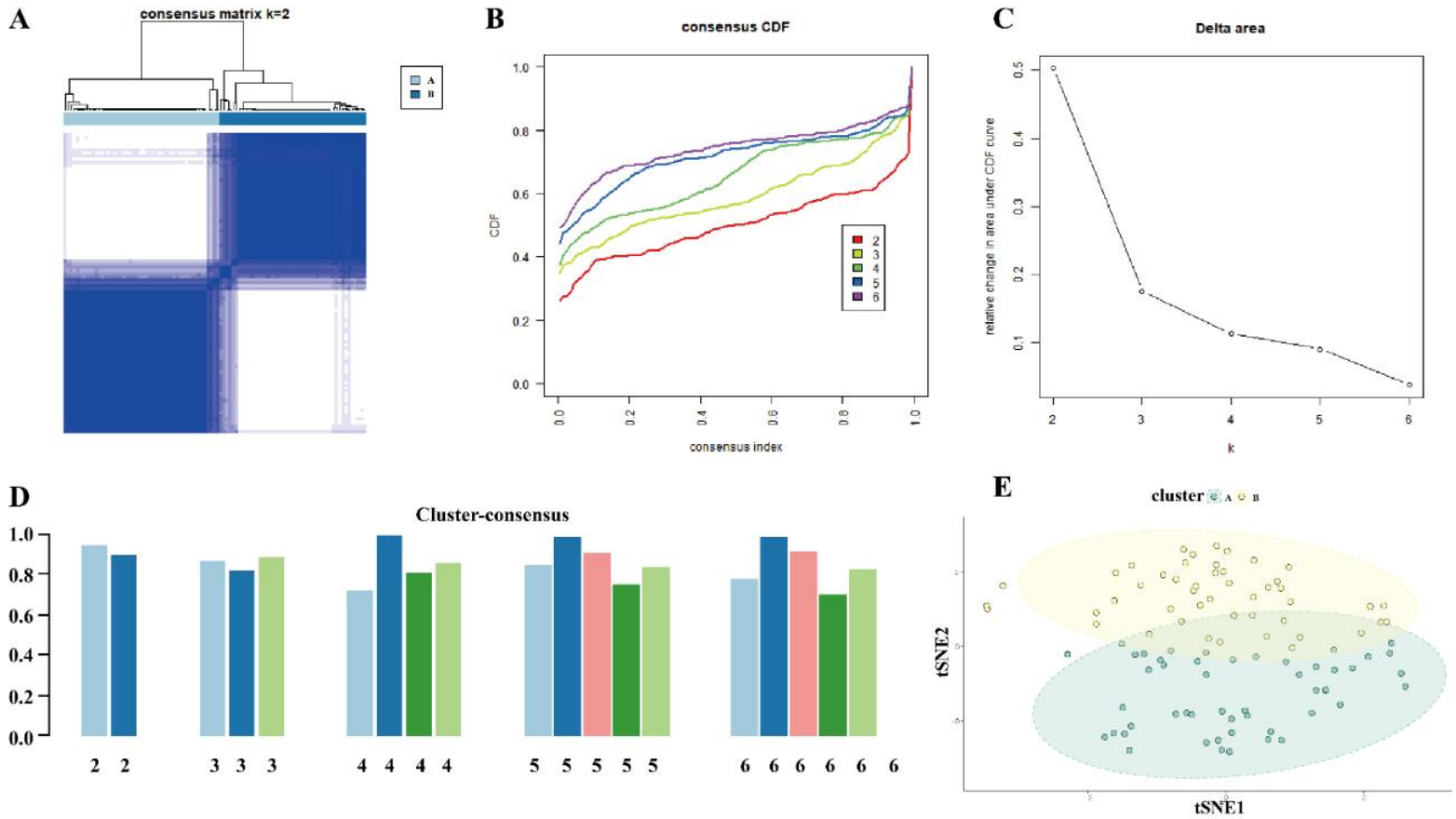

Figure 28. Identification of aging-related molecular clusters in AD patients. (A) Consensus clustering matrix when k = 2. (B) Representative cumulative distribution function (CDF) curves. (C) CDF delta area curves. (D) The score of cluster consensus. (E) The distribution of two subtypes was visualized using t-SNE.

5.3.2.3.WGCNA construction and gene module screening

We constructed a co-expression network and corresponding modules for both control subjects and AD patients using the WGCNA method, with the goal of pinpointing significant gene modules associated with AD. TRGs were sourced from the TelNet database and intersected with the GSE132903 dataset, yielding an expression matrix of 1,886 TRGs suitable for the analysis. Co-expressed gene modules were delineated at a soft power threshold of 4, achieving a scale-free topology R-squared criterion of 0.85 (Figure 29A). Utilizing a dynamic tree-cutting algorithm, we identified five distinct co-expression modules, each represented by a unique color (Figure 29B & C), and also presented the TOM heatmap (Figure 29D). Further analysis of the TRGs within these modules was conducted to assess the co-expression in relation to clinical traits (AD and control), as well as their correlation and topological closeness. The blue module, comprising 480 TRGs, demonstrated the strongest association with AD (Figure 29E). Subsequently, a scatterplot correlating module membership within the blue module with gene significance for AD was created (Figure 29F), facilitating the identification of key hub gene sets based on high gene significance (GS > 0.5) and module membership (MM > 0.5).

Additionally, employing the WGCNA algorithm, we identified essential gene modules that exhibit a robust connection with aging clusters, as defined by TRGs. The soft power was set to 4, and the scale-free R-squared was targeted at 0.85 (Figure 30A). Through the dynamic tree-cutting approach, four co-expression modules emerged, each with a distinct hue (Figure 30B & C), accompanied by a TOM heatmap (Figure 30D). The module-trait relationship heatmap indicated that the blue module correlated most highly

with Cluster A (Figure 30E), and a scatterplot delineated the correlation distribution of 414 TRGs within the blue module (Figure 30F). Ultimately, we filtered and extracted hub genes characterized by significant gene significance (GS > 0.5) and module membership (MM > 0.5).

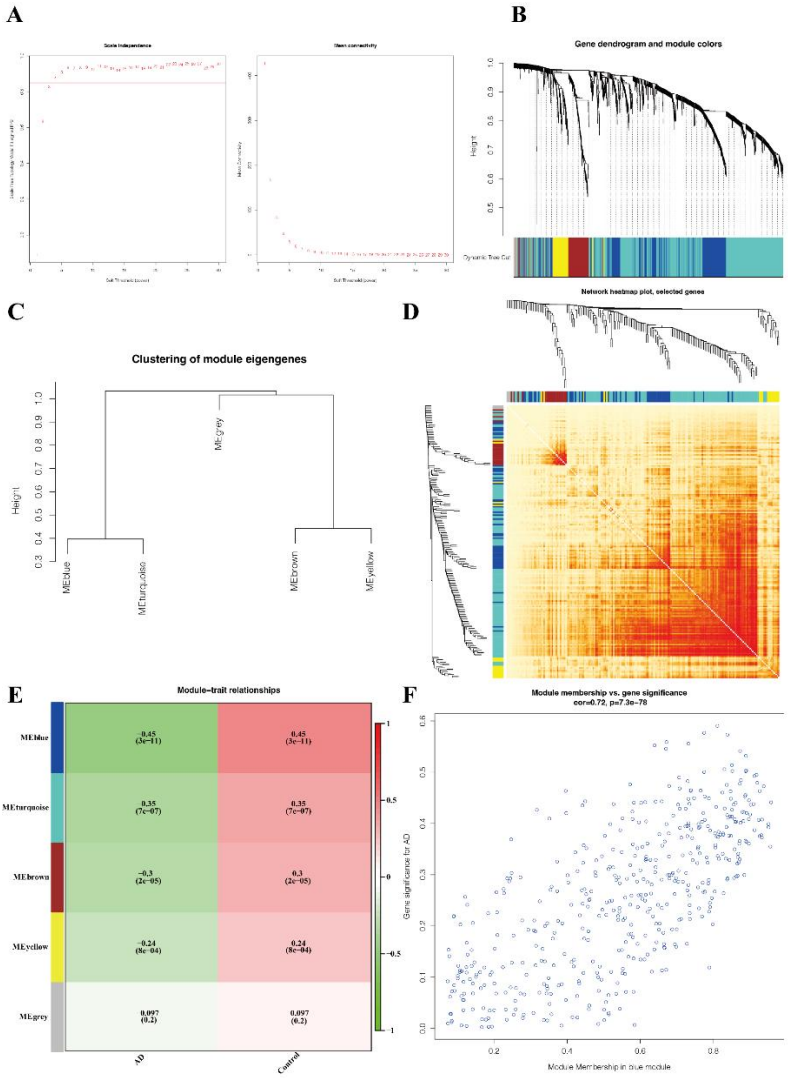

Figure 29. Co-expression network of telomere-related differentially expressed genes in AD patients. (A) The decision of soft threshold power. (B) Cluster tree dendrogram of co-expression modules. Different hues signify various co-expression modules. (C) Clustering of module eigengenes. (D) Heatmap of the correlations among 5 modules. (E) Investigation of the relationship between clinical traits and the module eigengenes. Each row indicates a module and each column indicates a clinical status. (F) The scatter plot represented module membership in the blue module and the gene significance for AD of module eigengenes.

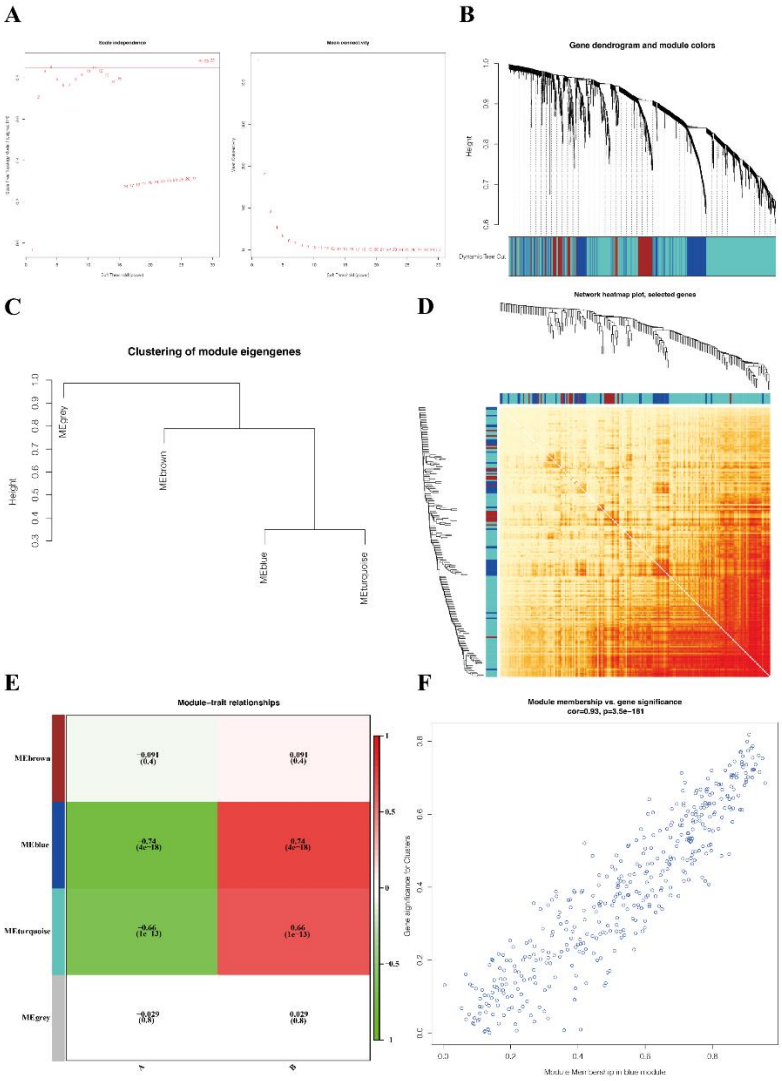

Figure 30. Co-expression network of telomere-related differentially expressed genes between two aging clusters. (A) The decision of soft threshold power. (B) Cluster tree dendrogram of co-expression modules. Different hues signify various co-expression modules. (C) Clustering of module eigengenes. (D) Heatmap of the correlations among 4 modules. (E) Investigation of the relationship between clinical traits and the module eigengenes. Each row indicates a module and each column indicates a clinical status. (F) The scatter plot represented module membership in the blue module and the gene significance for aging clusters of module eigengenes.

5.3.2.4.Construction and validation of machine-learning models

We identified a set of 10 TRGs by intersecting two gene sets with high connectivity (GS >0.5, MM >0.5) from the WGCNA modules. To enhance the diagnostic potential, we leveraged four prevalent machine learning algorithms to construct a diagnostic framework.

Among the models, the GLM demonstrated the lowest residuals (Figure 31A＆B), and the variables MCM7, HMGN5, and CERS1 emerged as significant predictors across all models (Figure 31C). For robust model evaluation, the training data underwent rigorous fivefold cross-validation, repeated 400 times, to ensure the reliability of the machine learning outcomes.

The diagnostic efficacy was assessed through the AUC values derived from the ROC curves of the four models. The GLM outperformed others with AUCs as follows: RF at 0.925, GLM at 0.985, GBM at 0.9, and SVM at 0.9 (Figure 317D–G). Consequently, the GLM was selected as the diagnostic model, with MCM7, HMGN5, and CERS1 as key diagnostic markers for validating AD versus control statuses.

To validate our predictive model, we applied it to two independent brain tissue datasets of AD patients and controls. The model exhibited robust performance, with AUC values of 0.832 in the GSE33000 dataset and 0.879 in the GSE122063 dataset (Figure 31H＆I), confirming the model's efficacy in distinguishing between AD patients and control individuals.

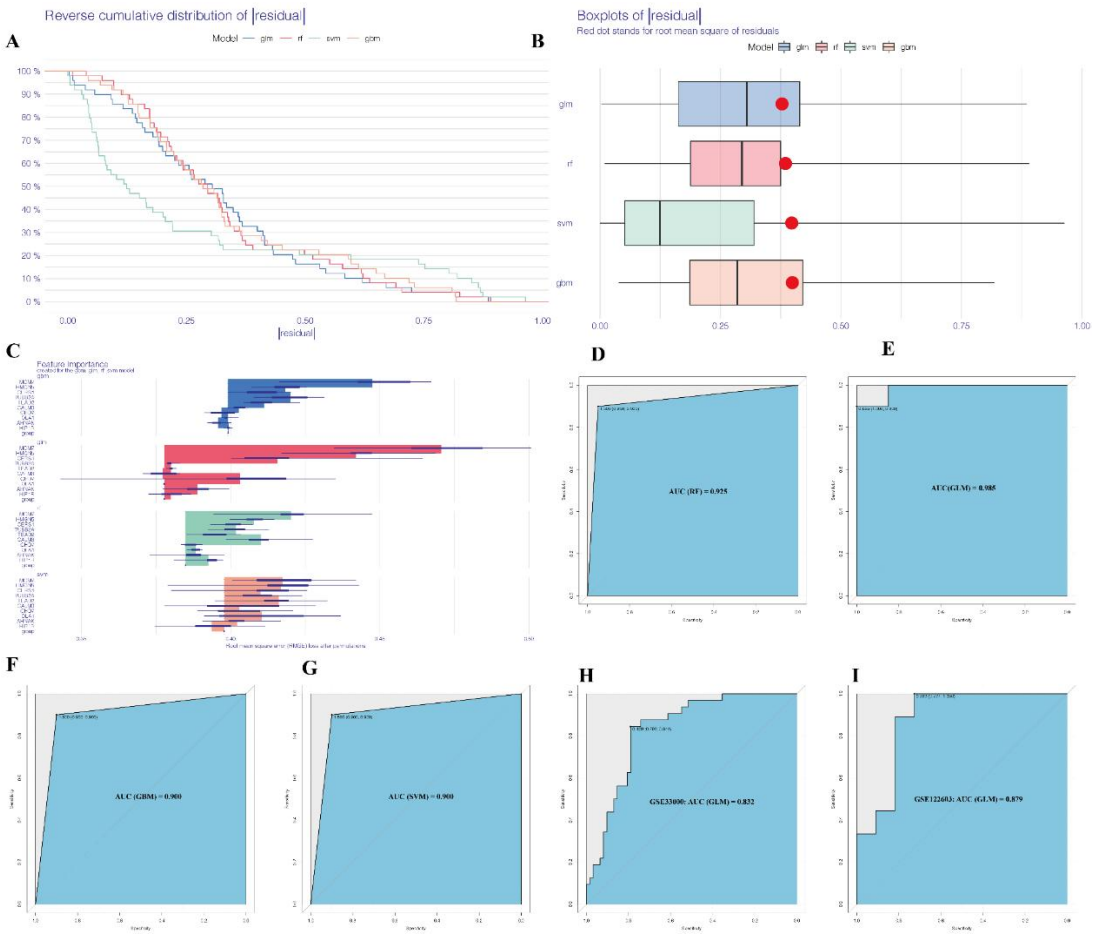

Figure 31. Construction of machine models for RF, GLM, GBM, and SVM. (A) Reverse cumulative residual distribution of each machine learning model. (B) The residuals for each machine-learning model were displayed in boxplots. The root mean square (RMSE) of the residuals was depicted by the red dot. (C) The features importance of RF, GLM, GBM, and SVM machine models. (D-G) ROC analysis of RF (D), GLM (E), GBM (F), and SVM (G) machine learning models based on 400 times 5-fold cross-validation and performed machine learning 2000 times to acquire the training results in the testing cohort. (H, I) ROC analysis of the 3-TRGs-based GLM model based on 400 times 5-fold cross-validation and performed machine learning 2000 times to acquire the validation results in GSE33000 (H) and GSE122063 (I) datasets.

5.3.2.5.Validation of the external method and datasets

We have crafted a prognostic model to differentiate AD from non-AD cases, employing the GLM for its validation, as depicted in Figure 32A. The model's predictive accuracy was scrutinized through a calibration plot and DCA. The calibration plot revealed only slight deviations between the projected and actual risk estimates, with MCM7 yielding the most accurate predictions (Figure 32B-E). The DCA corroborated the model's high level of precision, underscoring its utility as a clinical instrument for evaluating the risk of AD (Figure 32F).

Furthermore, a predictive model based on three genes was devised to forecast AD subtypes linked to the aging process, as shown in Figure 33A. The calibration plot indicated a strong correlation between the actual and projected risks, with MCM7 consistently displaying minimal variance (Figure 33B-E). The DCA demonstrated the model's effectiveness in discerning AD subtypes associated with aging, underscoring its clinical potential (Figure 33F).

To ascertain the diagnosis of AD in patients as opposed to controls, we utilized TRGs to construct ANNs. Our ANN model featured a hidden layer comprising five nodes. The diagnostic accuracy for each TRG was appraised using the ROC curve and the AUC metric. Notably, MCM7 demonstrated the greatest discriminatory power, with AUC values of 0.8449 for MCM7, 0.8335 for CERS1, and 0.8267 for HMGN5 (Figure 34A). For external validation, we leveraged two datasets, GSE33000 and GSE122063, to evaluate the diagnostic efficacy of the TRGs through ANNs. In the GSE33000 dataset, MCM7 once again showed superior discrimination, with AUC values of 0.7972 for MCM7, 0.7200 for CERS1, and 0.7588 for HMGN5. In contrast, in the GSE122063

dataset, CERS1 emerged as the most diagnostically capable, with AUC values of 0.7626 for MCM7, 0.7662 for CERS1, and 0.6668 for HMGN5 (Figure 34B & C). The ANN results validated that these three TRGs are efficacious in distinguishing between AD patients and controls across two distinct brain tissue datasets. Additionally, we developed ANNs to gauge the TRGs' ability to identify aging clusters. The ROC curves and AUC values indicated that these genes can also accurately differentiate AD subtypes related to aging (Figure 34D).

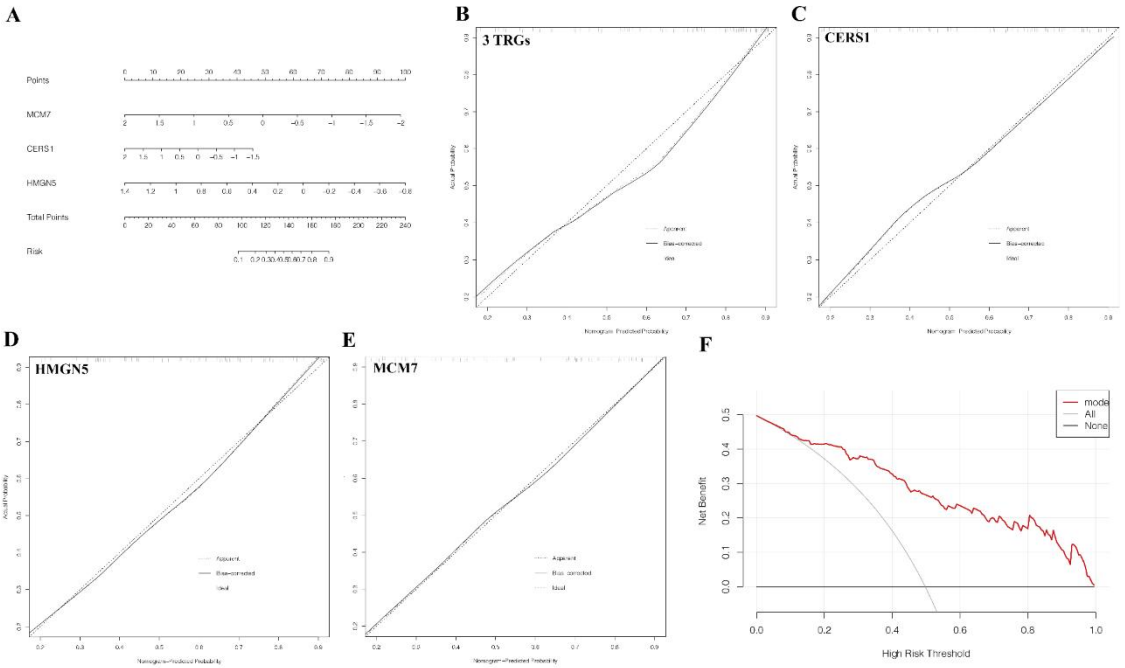

Figure 32. Validation of the diagnostic efficiency with 3 TRGs in AD patients. (A) Construction of a nomogram for predicting the risk of AD patients based on the 3 TRGs by logistic regression. (B-E) Construction of calibration curve with 3 TRGs (B), CERS1 (C), HMGN5 (D), and MCM7 (E), respectively. (F) Construction of decision curve analysis (DCA)

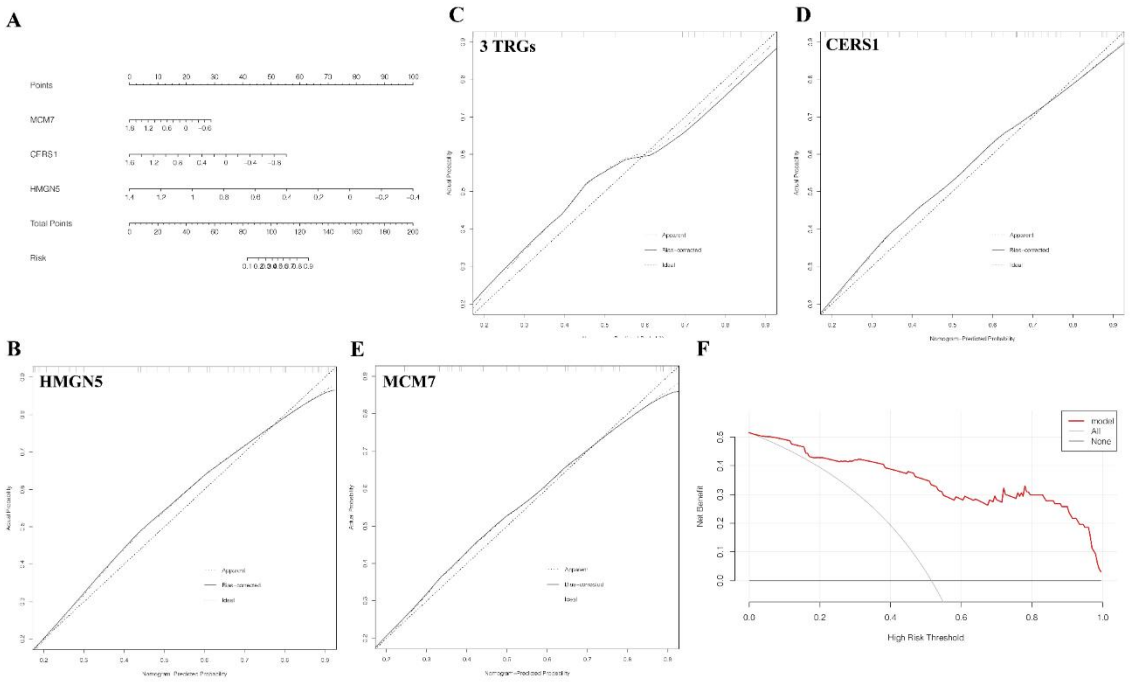

Figure 33. Validation of the diagnostic efficiency with 3 TRGs between aging clusters. (A) Construction of a nomogram for predicting the risk of aging-related AD subtypes based on the 3 TRGs by logistic regression. (B-E) Construction of calibration curve with 3 TRGs (B), CERS1 (C), HMGN5 (D), and MCM7 (E), respectively. (F) Construction of decision curve analysis (DCA).

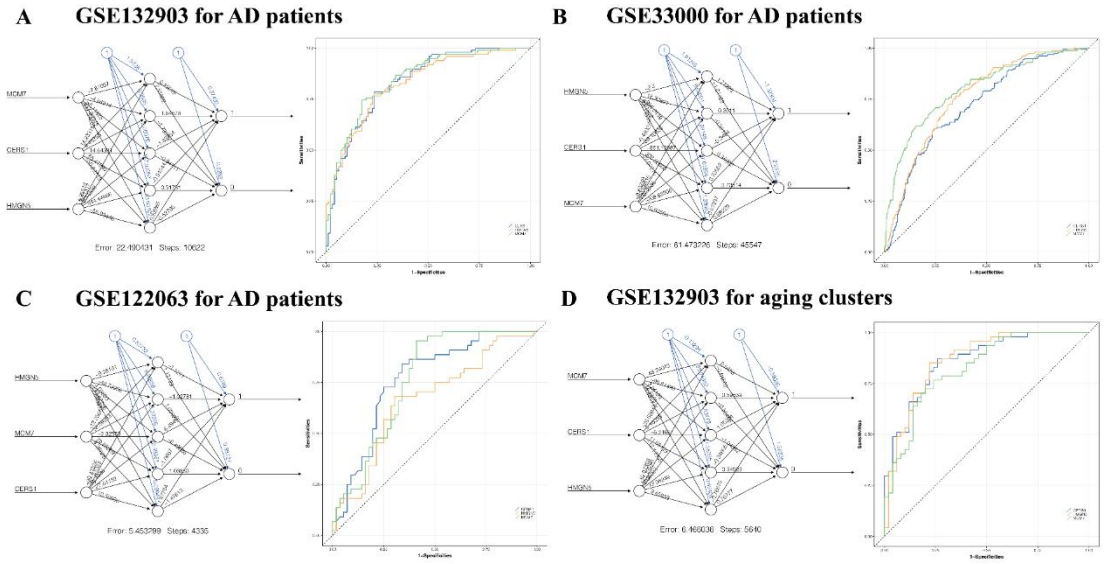

Figure 34. Validation of the diagnostic efficiency with 3 TRGs by ANN. (A) Construction of an ANN model for predicting the risk of AD patients based on the 3 TRGs in the GSE132903 dataset and ROC analysis of the ANN model based on 3 TRGs in the GSE132903 dataset. (B) Construction of an ANN model for predicting the risk of AD patients based on the 3 TRGs in the GSE33000 dataset and ROC analysis of the ANN model based on 3 TRGs in the GSE33000 dataset. (C) Construction of an ANN model for predicting the risk of AD patients based on the 3 TRGs in GSE122063 dataset and ROC analysis of the ANN model based on 3 TRGs in GSE122063 dataset (D) Construction of an ANN model for predicting the risk of aging-related AD subtypes based on the 3 TRGs in GSE132903 dataset and ROC analysis of the ANN model based on 3 TRGs in GSE132903 dataset.

5.3.3.The mechanism by which hericenone C improves the AD cell model induced by $A\beta_{25-35}$

5.3.3.1.Hericenone C can regulate NGF and bioinformatics screening genes to exert neuroprotective effects

We used the three doses of hericenone C (1, 10, 20 μM) in the cell viability experiment of the model induced by Aβ25-35 to detect and verify relevant indicators. First, the mRNA expression of NGF was significantly reduced under the induction of $A\beta_{25-35}$ and was upregulated with the addition of hericenone C (Figure 35A). This is consistent with previous studies. At the same time, the three telomere senescence-related genes, MCM7, CERS1, and HMGN5, which were screened by bioinformatics, showed significantly increased expression in the model group, which is consistent with the results of the human brain transcriptome. Moreover, when hericenone C was added, all three showed improvement. For MCM7, all three doses significantly downregulated its expression, with 10 μM Hericenone C showing the best effect (Figure 35B). For CERS1, only 10 and 20 μM of hericenone C could improve the situation (Figure 35C). Hericenone C can also downregulate the expression of HMGN5, and this effect is dose-dependent (Figure 35D).

The results indicate that hericenone C not only promotes the expression of NGF but also exerts neuroprotective effects on SH-SY5Y cells induced by $A\beta_{25-35}$ through the regulation of telomere senescence-associated genes.

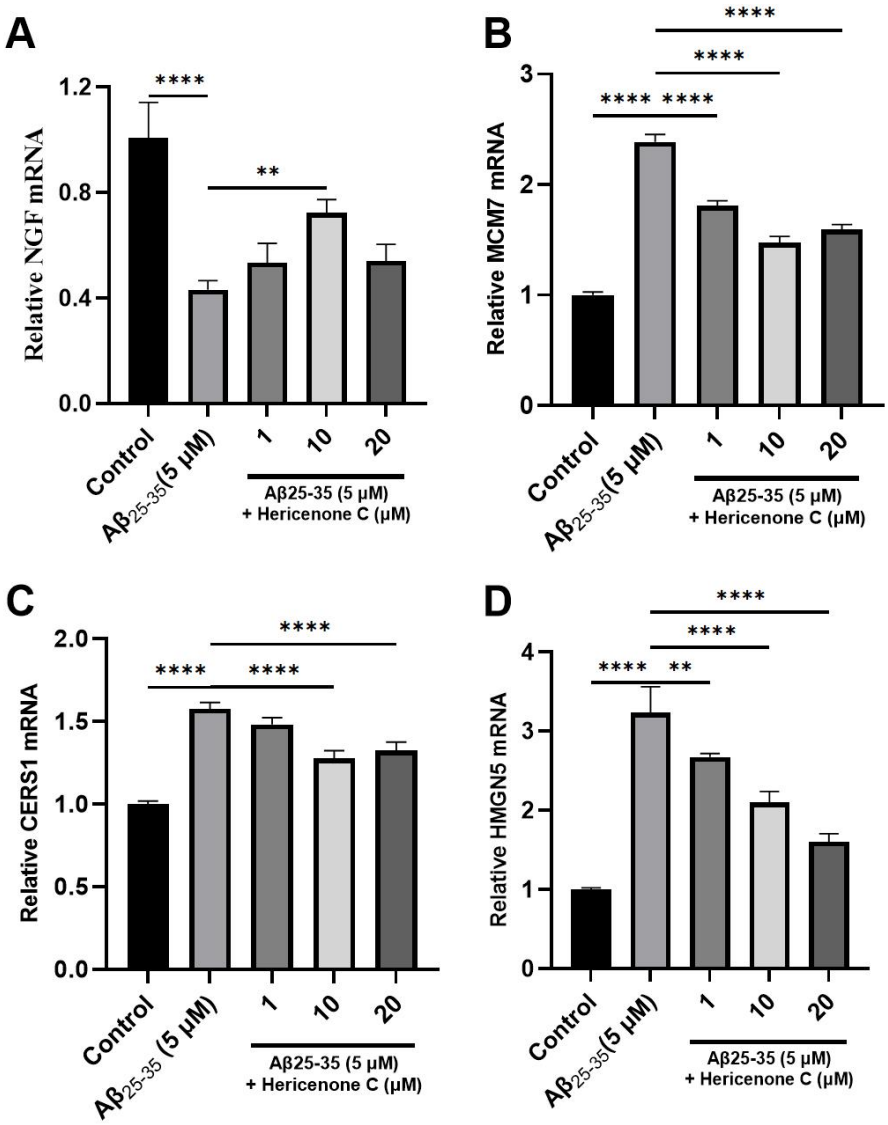

Figure 35. The expression of genes. (A) NGF mRNA relative expression. (B) MCM7 mRNA relative expression. (C) CERS1 mRNA relative expression. (D) HMGN5 mRNA relative expression. All data are presented as means ± S.D. *p < 0.05, **p < 0.01, ***p <0.001, ****p <0.0001.

5.3.3.2.Hericenone C exerts neuroprotective effects by regulating the TrkA/ERK/CREB signaling pathway

In addition to detecting the expression of NGF, we also studied the pathways downstream of NGF. We used the best dose of hericenone C for regulating NGF expression (10 μM) to detect and verify the relevant indicators on the $A\beta_{25-35}$-induced SH-SY5Y cell model.

By detecting the phosphorylated proteins related to the pathway, we can find that the phosphorylation level of proteins in the $A\beta_{25-35}$-induced SH-SY5Y cell model group is suppressed, while the addition of hericenone C promotes the phosphorylation level. This indicates that hericenone C can play a neuroprotective role through the NGF/TrkA/ERK/CREB pathway (Figure 36).

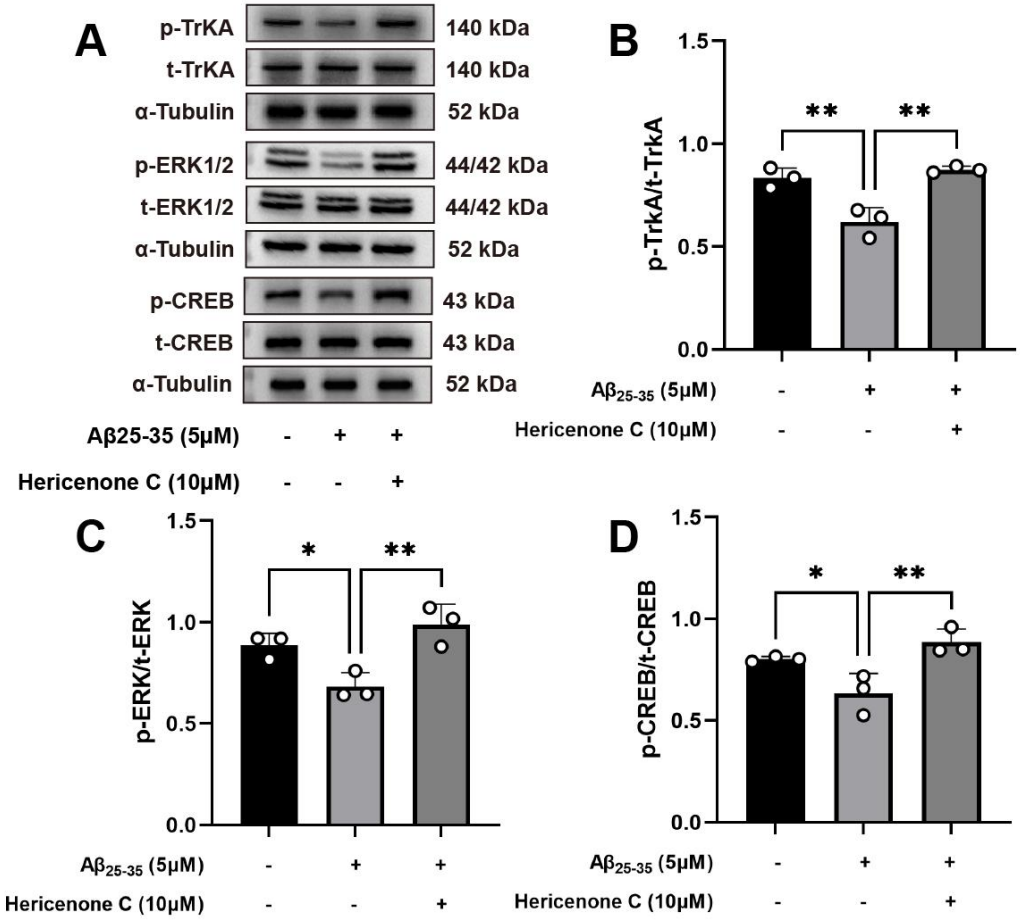

Figure 36. The expression of the downstream pathways of NGF has been altered by hericenone C. (A) The expression profiles of the prototype and phosphorylated forms of Trk A, ERK1/2, and CREB proteins. (B) The expression of phosphorylated TrkA protein. (C) The expression of phosphorylated ERK1/2 protein. (D) The expression of phosphorylated CREB protein. All data are presented as means ± S.D. *p < 0.05, **p < 0.01, ***p <0.001, ****p <0.0001.

5.4.Conclusion

In this chapter, we conducted a study on the neuroprotective activity of hericenone C using a variety of methods. Initially, we explored the impact of hericenone C on the viability of SH-SY5Y cells and found that hericenone C could promote the proliferation of SH-SY5Y cells. Subsequently, we established an AD model using $A\beta_{25-35}$ on neuronal cells and discovered that hericenone C could ameliorate cell death caused by $A\beta_{25-35}$.

According to past literature, hericenone C not only promotes the synthesis of NGF in vitro[63], but a mixture rich in hericenone C also has a protective effect on the cognition of aged mice [65] . Furthermore, our literature review revealed a very close connection between aging, AD, and telomeres, leading us to hypothesize that hericenone C could regulate targets and pathways related to telomere aging to exert neuroprotective effects.

To verify this hypothesis, we performed bioinformatics research using public database transcriptome data from AD brains, combining gene sets related to aging and telomeres. We found that targets related to the NGF/TrkA/ERK/CREB pathway were present in gene sets from aging or telomere databases. Through bioinformatics analysis, we identified telomere genes most relevant to aging and AD, namely MCM7, HMGN5, and CERS1, and validated the related targets through cell models, finding that hericenone C could improve the expression of these genes, further supporting the anti-aging effects of hericenone C.

Finally, we measured the targets of the NGF pathway and found that hericenone C could promote the phosphorylation levels of related targets, promoting the growth of neurons, which further elucidates the neuroprotective activity of hericenone C.

Chapter 6 Conclusion and prospective

6.1.Conclusion

This study delves into the medicinal and edible fungus, Hericium erinaceus (*H. erinaceus*), with a systematic exploration of its hydrophobic components and an in-depth investigation of their anti-inflammatory and neuroprotective mechanisms. Utilizing dichloromethane (DCM) as the extraction solvent, coupled with column chromatography, mass spectrometry (MS), and nuclear magnetic resonance (NMR), we have successfully isolated and identified a series of novel secondary metabolites, including hericenones and sterols. Among these, hericenone C, a derivative with a high content, has been a focal point of this research due to its neuroprotective activity and potential anti-aging effects.

Metabolomics analysis has enabled us to identify components in the *H. erinaceus* dichloromethane extract (HEDE) that can enter the bloodstream in their original form. Notably, hericenone C has been confirmed to enter the mouse circulatory system intact, providing a foundation for subsequent pharmacological activity studies. In the context of the ongoing COVID-19 pandemic, lung protection has become a critical area of focus. We have constructed an acute lung injury (ALI) mouse model to evaluate the anti-inflammatory activity of HEDE. Integrating plasma pharmacochemistry with network pharmacology analysis, we have revealed that HEDE may exert anti-inflammatory effects via the TLR4/NFKB1/STAT3/HIF-1α signaling pathway, a hypothesis that was corroborated using molecular biological methods. These findings offer a scientific rationale for the development of *H. erinaceus* as a functional food with potential lung protective properties.

In the realm of neuroprotection, this study has established an Alzheimer's disease (AD) cell model induced by amyloid β-protein ($A\beta_{25-35}$) and demonstrated that hericenone C

can ameliorate neuronal cell death triggered by $A\beta_{25-35}$. A literature review has shed light on the anti-aging and neurotrophic effects of hericenone, prompting us to explore its application in treating AD, the most prevalent neurodegenerative disorder. Bioinformatics analysis has unveiled a close link between aging, telomeres, and AD, identifying new targets and suggesting that the NGF/TrkA/ERK/CREB pathway is intertwined with telomere aging. Our molecular biology studies have shown that hericenone C can exert neuroprotective effects by modulating targets associated with telomere aging and the NGF/TrkA/ERK/CREB pathway. These findings not only offer new insights into the neuroprotective mechanisms of hericenone C but also present it as a promising candidate for the development of AD therapeutics.

6.2.Prospective

Despite the significant strides made in understanding the active components and pharmacological effects of *H. erinaceus*, several areas warrant further investigation. The pharmacokinetics and metabolic profile of hericenone C in vivo remain to be fully elucidated, necessitating future research into its absorption, distribution, metabolism, and excretion. Although hericenone C's neuroprotective effects have been validated in cellular models, its in vivo efficacy and safety must be assessed through preclinical and clinical trials. Additionally, the precise molecular targets of hericenone C's action require more in-depth exploration to uncover its full therapeutic potential. Furthermore, the bioinformatics-identified targets need to be experimentally validated to understand their roles in AD progression.

The study also highlights the need to explore other secondary metabolites present in *H. erinaceus*. Questions such as whether the other hericenones isolated possess similar or distinct biological activities, their potential as new drug candidates, and the existence

and activity of hericenone C metabolites in the bloodstream are all critical areas for future research.

By addressing these research gaps, we aim to fully harness the medicinal potential of *H. erinaceus*, contributing significantly to advancements in human health and disease management.

REFERENCE

1. Abdel-Razek, A. S., El-Naggar, M. E., Allam, A., Morsy, O. M. & Othman, S. I. Microbial Natural Products in Drug Discovery. *Processes 2020, Vol. 8, Page 470* **8**, 470 (2020).
2. Yuan, H., Ma, Q., Ye, L. & Piao, G. The Traditional Medicine and Modern Medicine from Natural Products. *Molecules 2016, Vol. 21, Page 559* **21**, 559 (2016).
3. Chopra, B. & Dhingra, A. K. Natural products: A lead for drug discovery and development. *Phytotherapy Research* **35**, 4660–4702 (2021).
4. Harvey, A. L. Natural products in drug discovery. *Drug Discov Today* **13**, 894–901 (2008).
5. Butler, M. S. The role of natural product chemistry in drug discovery. *J Nat Prod* **67**, 2141–2153 (2004).
6. Harvey, A. L., Clark, R. L., Mackay, S. P. & Johnston, B. F. Current strategies for drug discovery through natural products. *Expert Opin Drug Discov* **5**, 559–568 (2010).
7. Wright, G. D. Unlocking the potential of natural products in drug discovery. *Microb Biotechnol* **12**, 55–57 (2019).
8. Vainio, H. & Mutanen, M. Functional foods - blurring the distinction between food and medicine. *Scand J Work Environ Health* **26**, 178–180 (2000).
9. Vo, T. S. & Kim, S. K. Fucoidans as a natural bioactive ingredient for functional foods. *J Funct Foods* **5**, 16–27 (2013).
10. Reis, F. S., Martins, A., Vasconcelos, M. H., Morales, P. & Ferreira, I. C. F. R. Functional foods based on extracts or compounds derived from mushrooms. *Trends Food Sci Technol* **66**, 48–62 (2017).
11. Zhang, Q. W., Lin, L. G. & Ye, W. C. Techniques for extraction and isolation of natural

products: a comprehensive review. *Chin Med* **13**, 20 (2018).

12. De Vita, D. *et al.* Water as Green Solvent: Methods of Solubilisation and Extraction of Natural Products—Past, Present and Future Solutions. *Pharmaceuticals 2022, Vol. 15, Page 1507* **15**, 1507 (2022).
13. Jiang, Z., Kempinski, C. & Chappell, J. Extraction and Analysis of Terpenes/Terpenoids. *Curr Protoc Plant Biol* **1**, 345 (2016).
14. Dev, S. Terpenoids. 691–807 (1989) doi:10.1007/978-3-642-74075-6_19.
15. Ludwiczuk, A., Skalicka-Woźniak, K. & Georgiev, M. I. Terpenoids. *Pharmacognosy: Fundamentals, Applications and Strategy* 233–266 (2017) doi:10.1016/B978-0-12-802104-0.00011-1.
16. Dias, M. C., Pinto, D. C. G. A. & Silva, A. M. S. Plant Flavonoids: Chemical Characteristics and Biological Activity. *Molecules 2021, Vol. 26, Page 5377* **26**, 5377 (2021).
17. Panche, A. N., Diwan, A. D. & Chandra, S. R. Flavonoids: an overview. *J Nutr Sci* **5**, e47 (2016).
18. Pietta, P. G. Flavonoids as antioxidants. *J Nat Prod* **63**, 1035–1042 (2000).
19. Kime, D. E. The Steroids. *Fundamentals of Comparative Vertebrate Endocrinology* 3–56 (1987) doi:10.1007/978-1-4899-3617-2_1.
20. Rabizadeh, F., Mirian, M. S., Doosti, R., Kiani-Anbouhi, R. & Eftekhari, E. Phytochemical Classification of Medicinal Plants Used in the Treatment of Kidney Disease Based on Traditional Persian Medicine. *Evid Based Complement Alternat Med* **2022**, (2022).
21. Patel Assistant Professor, S. S., Savjani Assistant Professor, J. K., Patel, S. S. & Savjani, J. K. Systematic review of plant steroids as potential anti-inflammatory agents: Current

status and future perspectives. *The Journal of Phytopharmacology* **4**, 121–125 (2015).

22. McGaw, L. J., Jäger, A. K. & Van Staden, J. Antibacterial effects of fatty acids and related compounds from plants. *South African Journal of Botany* **68**, 417–423 (2002).

23. Ackman, R. G. Marine Biogenic Lipids, Fats & Oils, Volume 1. 472 (1989).

24. De Carvalho, C. C. C. R. & Caramujo, M. J. The Various Roles of Fatty Acids. *Molecules 2018, Vol. 23, Page 2583* **23**, 2583 (2018).

25. STURGEON, R. J. Monosaccharides. **2**, 1–37 (1990).

26. Disaccharides. **2**, 111–188 (1990).

27. Ukai, S., Kiho, T., Hara, C., Kuruma, I. & Tanaka, Y. POLYSACCHARIDES IN FUNGI. XIV. ANTI-INFLAMMATORY EFFECT OF THE POLYSACCHARIDES FROM THE FRUIT BODIES OF SEVERAL FUNGI. *J Pharmacobiodyn* **6**, 983–990 (1983).

28. Hromádková, Z., Ebringerová, A. & Valachovič, P. Comparison of classical and ultrasound-assisted extraction of polysaccharides from Salvia officinalis L. *Ultrason Sonochem* **5**, 163–168 (1999).

29. Chemat, S., Lagha, A., AitAmar, H., Bartels, P. V. & Chemat, F. Comparison of conventional and ultrasound-assisted extraction of carvone and limonene from caraway seeds. *Flavour Fragr J* **19**, 188–195 (2004).

30. Tian, Y. *et al.* Ultrasonic-assisted extraction and antioxidant activity of polysaccharides recovered from white button mushroom (Agaricus bisporus). *Carbohydr Polym* **88**, 522–529 (2012).

31. Gamal-Eldeen, A. M., Ahmed, E. F. & Abo-Zeid, M. A. In vitro cancer chemopreventive properties of polysaccharide extract from the brown alga, Sargassum latifolium. *Food and Chemical Toxicology* **47**, 1378–1384 (2009).

32. Alban, S. & Franz, G. Characterization of the Anticoagulant Actions of a Semisynthetic Curdlan Sulfate. *Thromb Res* **99**, 377–388 (2000).

33. Li, S. *et al.* Molecular Modification of Polysaccharides and Resulting Bioactivities. *Compr Rev Food Sci Food Saf* **15**, 237–250 (2016).

34. Wu, G. Amino acids: metabolism, functions, and nutrition. *Amino Acids 2009 37:1* **37**, 1–17 (2009).

35. Li, P., Yin, Y. L., Li, D., Kim, W. S. & Wu, G. Amino acids and immune function. *British Journal of Nutrition* **98**, 237–252 (2007).

36. Oakenfull, D. & Sidhu, G. S. SAPONINS. *Toxicants of Plant Origin: Glycosides: Volume II* 97–141 (2023) doi:10.1201/9781003418276-4/SAPONINS-DAVID-OAKENFULL-GURCHARN-SIDHU.

37. Chen, Y., Guo, Q., Zhu, Z. & Zhang, L. Changes in bioactive components related to the harvest time from the spicas of Prunella vulgaris. *Pharm Biol* **50**, 1118–1122 (2012).

38. Xia, E. Q. *et al.* Ultrasound-assisted extraction of oleanolic acid and ursolic acid from Ligustrum lucidum Ait. *Ultrason Sonochem* **19**, 772–776 (2012).

39. Yang, B., Yang, H., Chen, F., Hua, Y. & Jiang, Y. Phytochemical analyses of Ziziphus jujuba Mill. var. spinosa seed by ultrahigh performance liquid chromatography-tandem mass spectrometry and gas chromatography-mass spectrometry. *Analyst* **138**, 6881–6888 (2013).

40. Kim, S. Y. *et al.* Enhanced biotransformation of the minor ginsenosides in red ginseng extract by Penicillium decumbens β-glucosidase. *Enzyme Microb Technol* **153**, 109941 (2022).

41. Kang, K. Bin *et al.* Combined Application of UHPLC-QTOF/MS, HPLC-ELSD and

1H–NMR Spectroscopy for Quality Assessment of DA-9801, A Standardised Dioscorea Extract. *Phytochemical Analysis* **28**, 185–194 (2017).

42. Subramani, B. & Sathiyarajeswaran, P. Current update on herbal sources of antithrombotic activity—a comprehensive review. *The Egyptian Journal of Internal Medicine 2022 34:1* **34**, 1–12 (2022).

43. Gupta, J., Ahuja, A. & Gupta, R. Green Approaches for Cancers Management: An Effective Tool for Health Care. *Anticancer Agents Med Chem* **22**, 101–114 (2021).

44. Lim, H. M. & Park, S. H. Regulation of reactive oxygen species by phytochemicals for the management of cancer and diabetes. *Crit Rev Food Sci Nutr* **63**, 5911–5936 (2023).

45. Adeoye, R. I., Joel, E. B., Igunnu, A., Arise, R. O. & Malomo, S. O. A review of some common African spices with antihypertensive potential. *J Food Biochem* **46**, e14003 (2022).

46. Hamed, K. A., El-Fiky, S. A., Gawish, A. M., Khalil, W. K. B. & Mohamed, H. R. H. Alleviation of nicotine-induced reproductive disorder, clastogenicity, and histopathological alterations by fenugreek saponin bulk and nanoparticles in male rats. *Environmental Science and Pollution Research* **29**, 47488–47501 (2022).

47. Kumar, N. & Goel, N. Phenolic acids: Natural versatile molecules with promising therapeutic applications. *Biotechnology Reports* **24**, e00370 (2019).

48. Alam, M. *et al.* Therapeutic Implications of Caffeic Acid in Cancer and Neurological Diseases. *Front Oncol* **12**, 860508 (2022).

49. Cal, M., Szakonyi, Z. & Pavlíková, N. Caffeic Acid and Diseases—Mechanisms of Action. *International Journal of Molecular Sciences 2023, Vol. 24, Page 588* **24**, 588 (2022).

50. Tajik, N., Tajik, M., Mack, I. & Enck, P. The potential effects of chlorogenic acid, the

main phenolic components in coffee, on health: a comprehensive review of the literature. *European Journal of Nutrition 2017 56:7* **56**, 2215–2244 (2017).

51. Kück, U., Bloemendal, S. & Teichert, I. Putting Fungi to Work: Harvesting a Cornucopia of Drugs, Toxins, and Antibiotics. *PLoS Pathog* **10**, e1003950 (2014).
52. Yuan, S. *et al.* Anticancer fungal natural products: Mechanisms of action and biosynthesis. *Eur J Med Chem* **202**, 112502 (2020).
53. Öztürk, M., Tel-Çayan, G., Muhammad, A., Terzioɨlu, P. & Duru, M. E. Mushrooms: A Source of Exciting Bioactive Compounds. *Studies in Natural Products Chemistry* **45**, 363–456 (2015).
54. Zhao, S. *et al.* Immunomodulatory Effects of Edible and Medicinal Mushrooms and Their Bioactive Immunoregulatory Products. *Journal of Fungi 2020, Vol. 6, Page 269* **6**, 269 (2020).
55. Sánchez, C. Reactive oxygen species and antioxidant properties from mushrooms. *Synth Syst Biotechnol* **2**, 13–22 (2017).
56. Muszyńska, B., Grzywacz-Kisielewska, A., Kała, K. & Gdula-Argasińska, J. Anti-inflammatory properties of edible mushrooms: A review. *Food Chem* **243**, 373–381 (2018).
57. Chugh, R. M. *et al.* Fungal Mushrooms: A Natural Compound With Therapeutic Applications. *Front Pharmacol* **13**, 925387 (2022).
58. Mizuno, T. Bioactive Substances in *Hericium erinaceus* (Bull.: Fr.) Pers. (Yamabushitake), and Its Medicinal Utilization. *Int J Med Mushrooms* **1**, 105–119 (1999).
59. Thongbai, B., Rapior, S., Hyde, K. D., Wittstein, K. & Stadler, M. Hericium erinaceus, an amazing medicinal mushroom. *Mycological Progress 2015 14:10* **14**, 1–23 (2015).

60. Sofroniew, M. V., Howe, C. L. & Mobley, W. C. Nerve growth factor signaling, neuroprotection, and neural repair. *Annu Rev Neurosci* **24**, 1217–1281 (2001).

61. Lad, S. P., Neet, K. E. & Mufson, E. J. Nerve Growth Factor: Structure, Function and Therapeutic Implications for Alzheimer's Disease. *Curr Drug Targets CNS Neurol Disord* **2**, 315–334 (2003).

62. Lübke, J. H. *et al.* Neurotrophic factors in Alzheimer's disease: pathogenesis and therapy. *Acta Neurobiol Exp (Wars)* **81**, 314–327 (2021).

63. Kawagishi, H. *et al.* Hericenones C, D and E, stimulators of nerve growth factor (NGF)-synthesis, from the mushroom Hericium erinaceum. *Tetrahedron Lett* **32**, 4561–4564 (1991).

64. Ratto, D. *et al.* Hericium erinaceus Improves Recognition Memory and Induces Hippocampal and Cerebellar Neurogenesis in Frail Mice during Aging. *Nutrients 2019, Vol. 11, Page 715* **11**, 715 (2019).

65. Roda, E. *et al.* Neuroprotective Metabolites of Hericium erinaceus Promote Neuro-Healthy Aging. *International Journal of Molecular Sciences 2021, Vol. 22, Page 6379* **22**, 6379 (2021).

66. Roda, E. *et al.* Searching for a Longevity Food, We Bump into Hericium erinaceus Primordium Rich in Ergothioneine: The "Longevity Vitamin" Improves Locomotor Performances during Aging. *Nutrients 2022, Vol. 14, Page 1177* **14**, 1177 (2022).

67. Martínez-Mármol, R. *et al.* Hericerin derivatives activates a pan-neurotrophic pathway in central hippocampal neurons converging to ERK1/2 signaling enhancing spatial memory. *J Neurochem* **165**, 791–808 (2023).

68. Ren, Z. *et al.* Immunomodulatory effects of hydroxyethylated Hericium erinaceus polysaccharide on macrophages RAW264.7. *Int J Biol Macromol* **105**, 879–885 (2017).

69. Wu, F. *et al.* Structure characterization of a novel polysaccharide from Hericium erinaceus fruiting bodies and its immunomodulatory activities. *Food Funct* **9**, 294–306 (2018).

70. Lee, J. S., Min, K. M., Cho, J. Y. & Hong, E. K. Study of macrophage activation and structural characteristics of purified polysaccharides from the fruiting body of Hericium erinaceus. *J Microbiol Biotechnol* **19**, 951–959 (2009).

71. Wu, D. *et al.* Structural Properties and Macrophage Activation of Cell Wall Polysaccharides from the Fruiting Bodies of Hericium erinaceus. *Polymers 2018, Vol. 10, Page 850* **10**, 850 (2018).

72. Liu, Z. *et al.* Transcriptome analysis of the effects of Hericium erinaceus polysaccharide on the lymphocyte homing in Muscovy duck reovirus-infected ducklings. *Int J Biol Macromol* **140**, 697–708 (2019).

73. Liu, Z. *et al.* Effects of Hericium erinaceus polysaccharide on immunity and apoptosis of the main immune organs in Muscovy duck reovirus-infected ducklings. *Int J Biol Macromol* **171**, 448–456 (2021).

74. Wu, F. & Huang, H. Surface morphology and protective effect of Hericium erinaceus polysaccharide on cyclophosphamide-induced immunosuppression in mice. *Carbohydr Polym* **251**, 116930 (2021).

75. Li, H. *et al.* Polysaccharides from an edible mushroom, Hericium erinaceus, alleviate ulcerative colitis in mice by inhibiting the NLRP3 inflammasomes and reestablish intestinal homeostasis. *Int J Biol Macromol* **267**, 131251 (2024).

76. Cui, W., Song, X., Li, X., Jia, L. & Zhang, C. Structural characterization of Hericium erinaceus polysaccharides and the mechanism of anti-T2DM by modulating the gut microbiota and metabolites. *Int J Biol Macromol* **242**, 125165 (2023).

77. Wu, Y. *et al.* Hericium erinaceus polysaccharide facilitates restoration of injured intestinal mucosal immunity in Muscovy duck reovirus-infected Muscovy ducklings. *Int J Biol Macromol* **107**, 1151–1161 (2018).

78. Qin, M. *et al.* Anti-Inflammatory Effects of Ethanol Extract of Lion's Mane Medicinal Mushroom, *Hericium erinaceus* (Agaricomycetes), in Mice with Ulcerative Colitis. *Int J Med Mushrooms* **18**, 227–234 (2016).

79. Noh, H. J. *et al.* Benzyl alcohol derivatives from the mushroom Hericium erinaceum attenuate LPS-stimulated inflammatory response through the regulation of NF-κB and AP-1 activity. *Immunopharmacol Immunotoxicol* **36**, 349–354 (2014).

80. Xie, G., Tang, L., Xie, Y. & Xie, L. Secondary Metabolites from Hericium erinaceus and Their Anti-Inflammatory Activities. *Molecules 2022, Vol. 27, Page 2157* **27**, 2157 (2022).

81. Priori, E. C. *et al.* Hericium erinaceus Extract Exerts Beneficial Effects on Gut–Neuroinflammaging–Cognitive Axis in Elderly Mice. *Biology (Basel)* **13**, 18 (2024).

82. Tu, J. qiu, Liu, H. ping, Wen, Y. hui, Chen, P. & Liu, Z. tian. A novel polysaccharide from Hericium erinaceus: Preparation, structural characteristics, thermal stabilities, and antioxidant activities in vitro. *J Food Biochem* **45**, e13871 (2021).

83. Han, Z. H., Ye, J. M. & Wang, G. F. Evaluation of in vivo antioxidant activity of Hericium erinaceus polysaccharides. *Int J Biol Macromol* **52**, 66–71 (2013).

84. Chang, H. C. *et al.* Hericium erinaceus inhibits TNF- α -induced angiogenesis and ROS generation through suppression of MMP-9/NF-κB signaling and activation of Nrf2-mediated antioxidant genes in human EA.hy926 endothelial cells. *Oxid Med Cell Longev* **2016**, (2016).

85. Hou, X. X. *et al.* Fruiting body polysaccharides of Hericium erinaceus induce apoptosis in human colorectal cancer cells via ROS generation mediating caspase-9-dependent signaling pathways. *Food Funct* **11**, 6128–6138 (2020).

86. Ma, B. J. *et al.* Cytotoxic aromatic compounds from Hericium erinaceum. *The Journal of Antibiotics 2010 63:12* **63**, 713–715 (2010).

87. Li, W. *et al.* Isolation and identification of aromatic compounds in Lion's Mane Mushroom and their anticancer activities. *Food Chem* **170**, 336–342 (2015).

88. Kimura, Y. *et al.* Hericerin, a New Pollen Growth Inhibitor from the Mushroom Hericium erinaceum. *Agric Biol Chem* **55**, 2673–2674 (1991).

89. Mori, K. *et al.* Inhibitory effect of hericenone B from Hericium erinaceus on collagen-induced platelet aggregation. *Phytomedicine* **17**, 1082–1085 (2010).

90. Wong, K. H., Sabaratnam, V., Abdullah, N., Kuppusamy, U. R. & Naidu, M. Effects of Cultivation Techniques and Processing on Antimicrobial and Antioxidant Activities of Hericium erinaceus (Bull.:Fr.) Pers. Extracts. *Food Technol Biotechnol* **47**, 47–55 (2009).

91. Kim, S. P., Moon, E., Nam, S. H. & Friedman, M. Hericium erinaceus mushroom extracts protect infected mice against Salmonella Typhimurium-induced liver damage and mortality by stimulation of innate immune cells. *J Agric Food Chem* **60**, 5590–5596 (2012).

92. Miyazawa, M., Takahashi, T., Horibe, I. & Ishikawa, R. Two new aromatic compounds and a new d-arabinitol ester from the mushroom Hericium erinaceum. *Tetrahedron* **68**, 2007–2010 (2012).

93. Wang, K. *et al.* Erinacerins c-l, isoindolin-1-ones with α-glucosidase inhibitory activity from cultures of the medicinal mushroom hericium erinaceus. *J Nat Prod* **78**, 146–154

(2015).

94. Chen, L. *et al.* Isoindolinone-containing meroterpenoids with α-glucosidase inhibitory activity from mushroom Hericium caput-medusae. *Fitoterapia* **122**, 107–114 (2017).

95. Wang, K. *et al.* Eight new alkaloids with PTP1B and α-glucosidase inhibitory activities from the medicinal mushroom Hericium erinaceus. *Tetrahedron* **71**, 9557–9563 (2015).

96. Kawagishi, H., Ando, M. & Mizuno, T. Hericenone A and B as cytotoxic principles from the mushroom hericium erinaceum. *Tetrahedron Lett* **31**, 373–376 (1990).

97. Kawagishi, H. *et al. CHROMANS, HERICENONES F, G AND H FROM THE MUSHROOM HERICIUM ERINACEUM*. vol. 32 (1993).

98. Ma, B. J. *et al.* Cytotoxic aromatic compounds from Hericium erinaceum. *The Journal of Antibiotics 2010 63:12* **63**, 713–715 (2010).

99. Ueda, K. *et al.* An endoplasmic reticulum (ER) stress-suppressive compound and its analogues from the mushroom Hericium erinaceum. *Bioorg Med Chem* **16**, 9467–9470 (2008).

100. Zhang, C. C. *et al.* Chemical constituents from Hericium erinaceus and their ability to stimulate NGF-mediated neurite outgrowth on PC12 cells. *Bioorg Med Chem Lett* **25**, 5078–5082 (2015).

101. Ruan, Y. *et al.* New benzaldehyde derivatives from the fruiting bodies of Hericium erinaceus with cytotoxic activity. *Nat Prod Res* **37**, 4089–4098 (2023).

102. Mori, K., Inatomi, S., Ouchi, K., Azumi, Y. & Tuchida, T. Improving effects of the mushroom Yamabushitake (Hericium erinaceus) on mild cognitive impairment: a double-blind placebo-controlled clinical trial. *Phytotherapy Research* **23**, 367–372 (2009).

103. Shevchuk, Y., Kuypers, K. & Janssens, G. E. Fungi as a source of bioactive molecules

for the development of longevity medicines. *Ageing Res Rev* **87**, 101929 (2023).

104. Wang, X. Y., Zhang, D. D., Yin, J. Y., Nie, S. P. & Xie, M. Y. Recent developments in Hericium erinaceus polysaccharides: extraction, purification, structural characteristics and biological activities. *Crit Rev Food Sci Nutr* **59**, S96–S115 (2019).

105. Wong, K. H., Naidu, M., David, P., Bakar, R. & Sabaratnam, V. Neuroregenerative Potential of Lion's Mane Mushroom, *Hericium erinaceus* (Bull.: Fr.) Pers. (Higher Basidiomycetes), in the Treatment of Peripheral Nerve Injury (Review). *Int J Med Mushrooms* **14**, 427–446 (2012).

106. Nagano, M. *et al.* Reduction of depression and anxiety by 4 weeks Hericium erinaceus intake. *Biomedical Research* **31**, 231–237 (2010).

107. Saitsu, Y., Nishide, A., Kikushima, K., Shimizu, K. & Ohnuki, K. Improvement of cognitive functions by oral intake of Hericium erinaceus. *Biomedical Research* **40**, 125–131 (2019).

108. Hiraki, E. *et al.* Anti-obesity activity of Yamabushitake (Hericium erinaceus) powder in ovariectomized mice, and its potentially active compounds. *J Nat Med* **71**, 482–491 (2017).

109. Yamashina, K. *et al.* Suppressive Effect of Fruiting Bodies of Medicinal Mushrooms on Demyelination and Motor Dysfunction in a Cuprizone-Induced Multiple Sclerosis Mouse Model. *Int J Med Mushrooms* **24**, 15–24 (2022).

110. Friedman, M. Chemistry, Nutrition, and Health-Promoting Properties of Hericium erinaceus (Lion's Mane) Mushroom Fruiting Bodies and Mycelia and Their Bioactive Compounds. *J Agric Food Chem* **63**, 7108–7123 (2015).

111. Hsu, P. C. *et al.* Erinacine A attenuates glutamate transporter 1 downregulation and protects against ischemic brain injury. *Life Sci* **306**, 120833 (2022).

112. Hsu, C. L. *et al.* Neuroprotective Effects of Erinacine A on an Experimental Model of Traumatic Optic Neuropathy. *International Journal of Molecular Sciences 2023, Vol. 24, Page 1504* **24**, 1504 (2023).

113. Lin, C.-Y. ; *et al.* Erinacine S from Hericium erinaceus mycelium promotes neuronal regeneration by inducing neurosteroids accumulation. *J Food Drug Anal* **31**, 32–54 (2023).

114. Tsai-Teng, T. *et al.* Erinacine A-enriched Hericium erinaceus mycelium ameliorates Alzheimer's disease-related pathologies in APPswe/PS1dE9 transgenic mice. *J Biomed Sci* **23**, 1–12 (2016).

115. Rascher, M. *et al.* Erinacine C Activates Transcription from a Consensus ETS DNA Binding Site in Astrocytic Cells in Addition to NGF Induction. *Biomolecules 2020, Vol. 10, Page 1440* **10**, 1440 (2020).

116. Lee, K. F. *et al.* Post-Treatment with Erinacine A, a Derived Diterpenoid of *H. erinaceus*, Attenuates Neurotoxicity in MPTP Model of Parkinson's Disease. *Antioxidants 2020, Vol. 9, Page 137* **9**, 137 (2020).

117. Lee, L.-Y. *et al.* Erinacine A-Enriched Hericium erinaceus Mycelium Delays Progression of Age-Related Cognitive Decline in Senescence Accelerated Mouse Prone 8 (SAMP8) Mice. *Nutrients 2021, Vol. 13, Page 3659* **13**, 3659 (2021).

118. Tsai, P. C. *et al.* Preclinical Bioavailability, Tissue Distribution, and Protein Binding Studies of Erinacine A, a Bioactive Compound from Hericium erinaceus Mycelia Using Validated LC-MS/MS Method. *Molecules 2021, Vol. 26, Page 4510* **26**, 4510 (2021).

119. Wu, Y. L. *et al.* The protective effect of erinacine A–enriched Hericium erinaceus mycelium ethanol extract on oxidative Stress–Induced neurotoxicity in cell and Drosophila models of spinocerebellar ataxia type 3. *Free Radic Biol Med* **195**, 1–12

(2023).

120. Lee, S. L. *et al.* Erinacine A Prevents Lipopolysaccharide-Mediated Glial Cell Activation to Protect Dopaminergic Neurons against Inflammatory Factor-Induced Cell Death In Vitro and In Vivo. *International Journal of Molecular Sciences 2022, Vol. 23, Page 810* **23**, 810 (2022).

121. Kobayashi, S. *et al.* Total Synthesis, Structure Revision, and Neuroprotective Effect of Hericenones C-H and Their Derivatives. *Journal of Organic Chemistry* **86**, 2602–2620 (2021).

122. Hak, C. K., Sang, D. Z., Sae, Y. C., Sang, U. C. & Kang, R. L. Cytotoxic ergosterols from Paecilomyces sp. J300. *Arch Pharm Res* **25**, 851–855 (2002).

123. Nowak, R. *et al.* A New Method for the Isolation of Ergosterol and Peroxyergosterol as Active Compounds of Hygrophoropsis aurantiaca and in Vitro Antiproliferative Activity of Isolated Ergosterol Peroxide. *Molecules 2016, Vol. 21, Page 946* **21**, 946 (2016).

124. Yu, S. M., Kim, H. J., Woo, E. R. & Park, H. Some sesquiterpenoids and 5α,8α-epidioxysterols from Solanum lyratum. *Arch Pharm Res* **17**, 1–4 (1994).

125. Dhama, K. *et al.* Medicinal and Therapeutic Potential of Herbs and Plant Metabolites / Extracts Countering Viral Pathogens - Current Knowledge and Future Prospects. *Curr Drug Metab* **19**, (2018).

126. Li, F. S. & Weng, J. K. Demystifying traditional herbal medicine with modern approach. *Nature Plants 2017 3:8* **3**, 1–7 (2017).

127. El-Amir, M. *et al.* Modern Approaches in the Discovery and Development of Plant-Based Natural Products and Their Analogues as Potential Therapeutic Agents. *Molecules 2022, Vol. 27, Page 349* **27**, 349 (2022).

128. Atanasov, A. G. *et al.* Natural products in drug discovery: advances and opportunities.

Nature Reviews Drug Discovery 2021 20:3 **20**, 200–216 (2021).

129. Zhou, K. *et al.* Integrated plasma pharmacochemistry and network pharmacology to explore the mechanism of Gerberae Piloselloidis Herba in treatment of allergic asthma. *J Ethnopharmacol* **298**, 115624 (2022).

130. Guan, H. *et al.* A multistep approach for exploring quality markers of Shengjiang Xiexin decoction by integrating plasma pharmacochemistry-pharmacokinetics-pharmacology. *J Pharm Biomed Anal* **241**, 115999 (2024).

131. Ren, J. ling *et al.* Network pharmacology combined with metabolomics approach to investigate the protective role and detoxification mechanism of Yunnan Baiyao formulation. *Phytomedicine* **77**, 153266 (2020).

132. Liu, C. S. *et al.* Network pharmacology and pharmacokinetics integrated strategy to investigate the pharmacological mechanism of Xianglian pill on ulcerative colitis. *Phytomedicine* **82**, 153458 (2021).

133. Wang, M. *et al.* Sharing and community curation of mass spectrometry data with Global Natural Products Social Molecular Networking. *Nature Biotechnology 2016 34:8* **34**, 828–837 (2016).

134. Sawada, Y. *et al.* RIKEN tandem mass spectral database (ReSpect) for phytochemicals: A plant-specific MS/MS-based data resource and database. *Phytochemistry* **82**, 38–45 (2012).

135. Horai, H. *et al.* MassBank: a public repository for sharing mass spectral data for life sciences. *Journal of Mass Spectrometry* **45**, 703–714 (2010).

136. Dunn, W. B. *et al.* Mass appeal: Metabolite identification in mass spectrometry-focused untargeted metabolomics. *Metabolomics* **9**, 44–66 (2013).

137. Liang, L. *et al.* Metabolic Dynamics and Prediction of Gestational Age and Time to Delivery in Pregnant Women. *Cell* **181**, 1680-1692.e15 (2020).

138. Hakeem Said, I. *et al.* LC-MS/MS based molecular networking approach for the identification of cocoa phenolic metabolites in human urine. *Food Research International* **132**, 109119 (2020).

139. Fan, S., Shahid, M., Jin, P., Asher, A. & Kim, J. Identification of Metabolic Alterations in Breast Cancer Using Mass Spectrometry-Based Metabolomic Analysis. *Metabolites 2020, Vol. 10, Page 170* **10**, 170 (2020).

140. Kim, H. W. *et al.* NPClassifier: A Deep Neural Network-Based Structural Classification Tool for Natural Products. *J Nat Prod* **84**, 2795–2807 (2021).

141. Badraoui, R., Alrashedi, M. M., El-May, M. V. & Bardakci, F. Acute respiratory distress syndrome: a life threatening associated complication of SARS-CoV-2 infection inducing COVID-19. *J Biomol Struct Dyn* **39**, 6842–6851 (2021).

142. SARS-CoV-2 causing pneumonia-associated respiratory disorder (COVID-19): diagnostic and proposed therapeutic options.

143. Boechat, J. L., Chora, I., Morais, A. & Delgado, L. The immune response to SARS-CoV-2 and COVID-19 immunopathology – Current perspectives. *Pulmonology* **27**, 423–437 (2021).

144. Melenotte, C. *et al.* Immune responses during COVID-19 infection. *Oncoimmunology* **9**, (2020).

145. Polidoro, R. B., Hagan, R. S., de Santis Santiago, R. & Schmidt, N. W. Overview: Systemic Inflammatory Response Derived From Lung Injury Caused by SARS-CoV-2 Infection Explains Severe Outcomes in COVID-19. *Front Immunol* **11**, (2020).

146. Wei, J. *et al.* Integrated Serum Pharmacochemistry and Network Pharmacology

Approach to Explore the Effective Components and Potential Mechanisms of Menispermi Rhizoma Against Myocardial Ischemia. *Front Chem* **10**, (2022).

147. Zhang, Y. *et al.* Uncovering pharmacological mechanisms of Wu-tou decoction acting on rheumatoid arthritis through systems approaches: drug-target prediction, network. *nature.comY Zhang, M Bai, B Zhang, C Liu, Q Guo, Y Sun, D Wang, C Wang, Y Jiang, N Lin, S LiScientific reports, 2015•nature.com*.

148. Zhang, Y. *et al.* Uncovering pharmacological mechanisms of Wu-tou decoction acting on rheumatoid arthritis through systems approaches: drug-target prediction, network analysis and experimental validation. *Scientific Reports 2015 5:1* **5**, 1–15 (2015).

149. Xu, T. *et al.* Systematically characterize the absorbed effective substances of Wutou Decoction and their metabolic pathways in rat plasma using UHPLC-Q-TOF-MS combined with a target network pharmacological analysis. *J Pharm Biomed Anal* **141**, 95–107 (2017).

150. Suo, T. *et al.* Combining Chemical Profiling and Network Analysis to Investigate the Pharmacology of Complex Prescriptions in Traditional Chinese Medicine. *Sci Rep* **7**, (2017).

151. D'Alessio, F. R. Mouse models of acute lung injury and ARDS. *Methods in Molecular Biology* **1809**, 341–350 (2018).

152. Nickel, J. *et al.* SuperPred: update on drug classification and target prediction. *Nucleic Acids Res* **42**, W26–W31 (2014).

153. Piñero, J. *et al.* The DisGeNET knowledge platform for disease genomics: 2019 update. *Nucleic Acids Res* **48**, D845–D855 (2020).

154. Amberger, J. S., Bocchini, C. A., Schiettecatte, F., Scott, A. F. & Hamosh, A. OMIM.org: Online Mendelian Inheritance in Man (OMIM®), an online catalog of human genes and

genetic disorders. *Nucleic Acids Res* **43**, D789–D798 (2015).

155. Chen, X., Wu, J., Fu, X., Wang, P. & Chen, C. Fructus mori polysaccharide alleviates diabetic symptoms by regulating intestinal microbiota and intestinal barrier against TLR4/NF-κB pathway. *Int J Biol Macromol* **249**, 126038 (2023).

156. Wang, Y., Ren, K., Tan, J. & Mao, Y. Alginate oligosaccharide alleviates aging-related intestinal mucosal barrier dysfunction by blocking FGF1-mediated TLR4/NF-κB p65 pathway. *Phytomedicine* **116**, 154806 (2023).

157. Gaojian, T. *et al.* Parthenolide promotes the repair of spinal cord injury by modulating M1/M2 polarization via the NF-κB and STAT 1/3 signaling pathway. *Cell Death Discovery 2020 6:1* **6**, 1–16 (2020).

158. Chen, M. *et al.* Baicalein is a novel TLR4-targeting therapeutics agent that inhibits TLR4/HIF-1α/VEGF signaling pathway in colorectal cancer. *Clin Transl Med* **11**, e564 (2021).

159. Pekarova, M. *et al.* Asymmetric dimethyl arginine induces pulmonary vascular dysfunction via activation of signal transducer and activator of transcription 3 and stabilization of hypoxia-inducible factor 1-alpha. *Vascul Pharmacol* **73**, 138–148 (2015).

160. Hodson, R. Alzheimer's disease. *Nature* **559**, S1–S1 (2018).

161. Scheltens, P. *et al.* Alzheimer's disease. *The Lancet* **397**, 1577–1590 (2021).

162. Zhang, P. *et al.* Senolytic therapy alleviates Aβ-associated oligodendrocyte progenitor cell senescence and cognitive deficits in an Alzheimer's disease model. *Nature Neuroscience 2019 22:5* **22**, 719–728 (2019).

163. Yu, G., Lu, L., Ma, Z. & Wu, S. Genetically Predicted Telomere Length and Its Relationship With Alzheimer's Disease. *Front Genet* **12**, 595864 (2021).

164. Cai, Z., Yan, L. J. & Ratka, A. Telomere Shortening and Alzheimer's Disease. *NeuroMolecular Medicine 2012 15:1* **15**, 25–48 (2012).

165. Fan, W. *et al.* Mining big data. *ACM SIGKDD Explorations Newsletter* **14**, 1–5 (2013).

166. Sah, S. Machine Learning: A Review of Learning Types. (2020) doi:10.20944/PREPRINTS202007.0230.V1.

167. Nies, H. W. *et al.* Enhanced directed random walk for the identification of breast cancer prognostic markers from multiclass expression data. *Entropy* **23**, 1232 (2021).

168. Zeng, Z. *et al.* Deep learning for cancer type classification and driver gene identification. *BMC Bioinformatics* **22**, 1–13 (2021).

169. Wang, H. *et al.* A cost-effective machine learning-based method for preeclampsia risk assessment and driver genes discovery. *Cell Biosci* **13**, 1–12 (2023).

170. Kaplan, D. R. & Miller, F. D. Neurotrophin signal transduction in the nervous system. *Curr Opin Neurobiol* **10**, 381–391 (2000).

171. Ip, N. Y., Li, Y., Yancopoulos, G. D. & Lindsay, R. M. Cultured hippocampal neurons show responses to BDNF, NT-3, and NT-4, but not NGF. *Journal of Neuroscience* **13**, 3394–3405 (1993).

172. Chao, M. V. Neurotrophins and their receptors: A convergence point for many signalling pathways. *Nature Reviews Neuroscience 2003 4:4* **4**, 299–309 (2003).

173. Hirose, M., Kuroda, Y. & Murata, E. NGF/TrkA Signaling as a Therapeutic Target for Pain. *Pain Practice* **16**, 175–182 (2016).

174. Limpert, A. S., Karlo, J. C. & Landreth, G. E. Nerve Growth Factor Stimulates the Concentration of TrkA within Lipid Rafts and Extracellular Signal-Regulated Kinase Activation through c-Cbl-Associated Protein. *Mol Cell Biol* **27**, 5686–5698 (2007).

175. Riccio, A., Pierchala, B. A., Ciarallo, C. L. & Ginty, D. D. An NGF-TrkA-mediated

retrograde signal to transcription factor CREB in sympathetic neurons. *Science (1979)* **277**, 1097–1100 (1997).

176. Chen, K. S. & Gage, F. H. Somatic gene transfer of NGF to the aged brain: behavioral and morphological amelioration. *Journal of Neuroscience* **15**, 2819–2825 (1995).

177. Lärkfors, L. *et al.* Decreased level of nerve growth factor (NGF) and its messenger RNA in the aged rat brain. *Molecular Brain Research* **3**, 55–60 (1987).

178. Budni, J., Bellettini-Santos, T., Mina, F., Garcez, M. L. & Zugno, A. I. The involvement of BDNF, NGF and GDNF in aging and Alzheimer's disease. *Aging Dis* **6**, 331 (2015).

179. Koh, S. & Loy, R. Age-related loss of nerve growth factor sensitivity in rat basal forebrain neurons. *Brain Res* **440**, 396–401 (1988).

180. Tamrakar, S. *et al.* Deacylated Derivative of Hericenone C Treated by Lipase Shows Enhanced Neuroprotective Properties Compared to Its Parent Compound. *Molecules* **28**, 4549 (2023).

181. Kim, M. J., Kim, J. H., Kim, J. H., Lee, S. & Cho, E. J. Amelioration effects of Cirsium japonicum var. maackii extract/fractions on amyloid beta25–35-induced neurotoxicity in SH-SY5Y cells and identification of the main bioactive compound. *Food Funct* **11**, 9651–9661 (2020).

182. Jia, G., Diao, Z., Liu, Y., Sun, C. & Wang, C. Neural stem cell-conditioned medium ameliorates Aβ25–35-induced damage in SH-SY5Y cells by protecting mitochondrial function. *Biomolecules and Biomedicine* **21**, 179–186 (2021).

183. Maurice, T., Lockhart, B. P. & Privat, A. Amnesia induced in mice by centrally administered β-amyloid peptides involves cholinergic dysfunction. *Brain Res* **706**, 181–193 (1996).

184. Lee, A. Y., Lee, M. H., Lee, S. & Cho, E. J. Alpha-Linolenic Acid from Perilla

frutescens var. japonica Oil Protects Aβ-Induced Cognitive Impairment through Regulation of APP Processing and Aβ Degradation. *J Agric Food Chem* **65**, 10719–10729 (2017).

185. Tacutu, R. *et al.* Human Ageing Genomic Resources: new and updated databases. *Nucleic Acids Res* **46**, D1083–D1090 (2018).

186. Wilkerson, M. D. & Hayes, D. N. ConsensusClusterPlus: a class discovery tool with confidence assessments and item tracking. *Bioinformatics* **26**, 1572–1573 (2010).

187. Langfelder, P. & Horvath, S. WGCNA: An R package for weighted correlation network analysis. *BMC Bioinformatics* **9**, 1–13 (2008).

Appendices

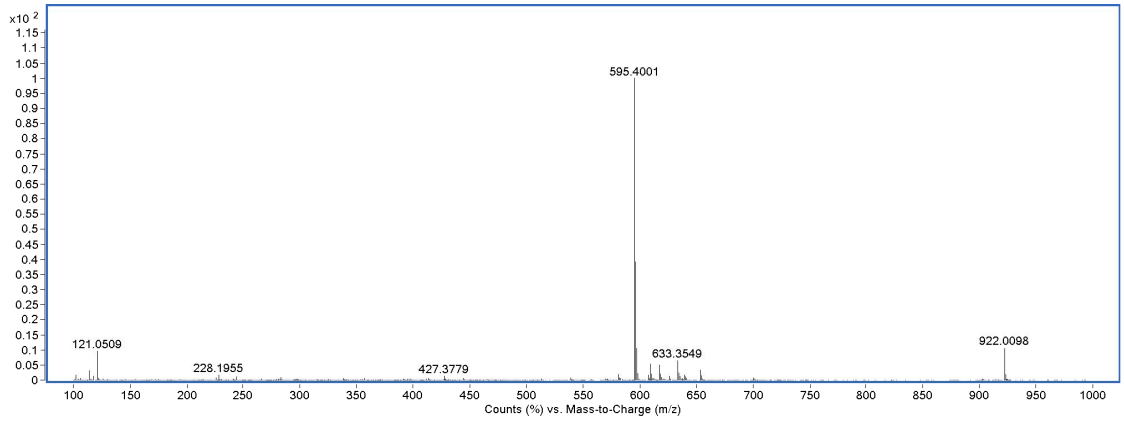

Figure S1. HRESIMS spectrum of compound **1**.

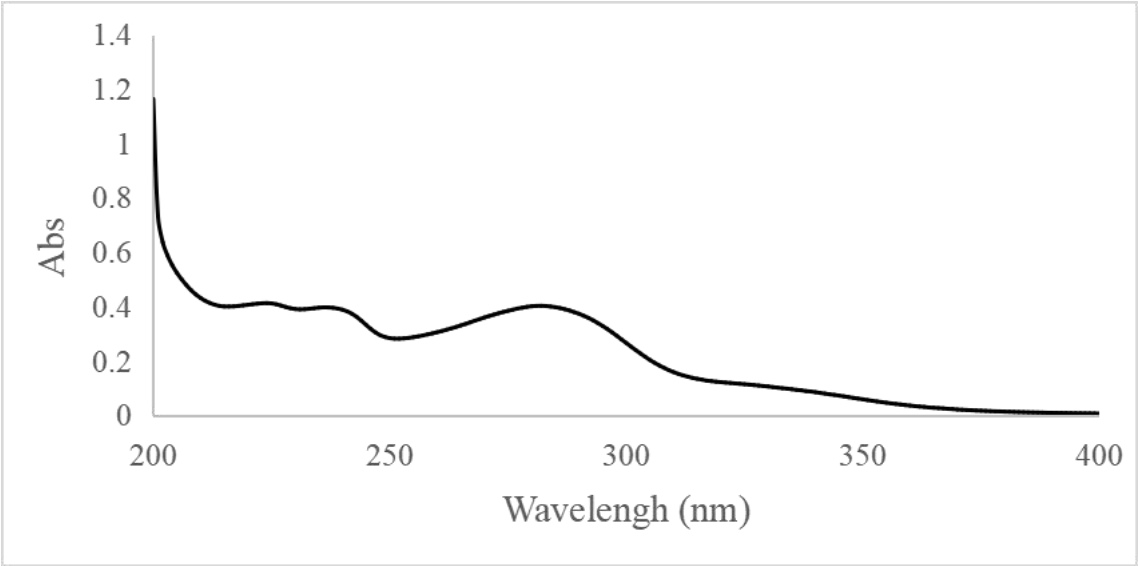

Figure S2. UV spectrum of compound **1**.

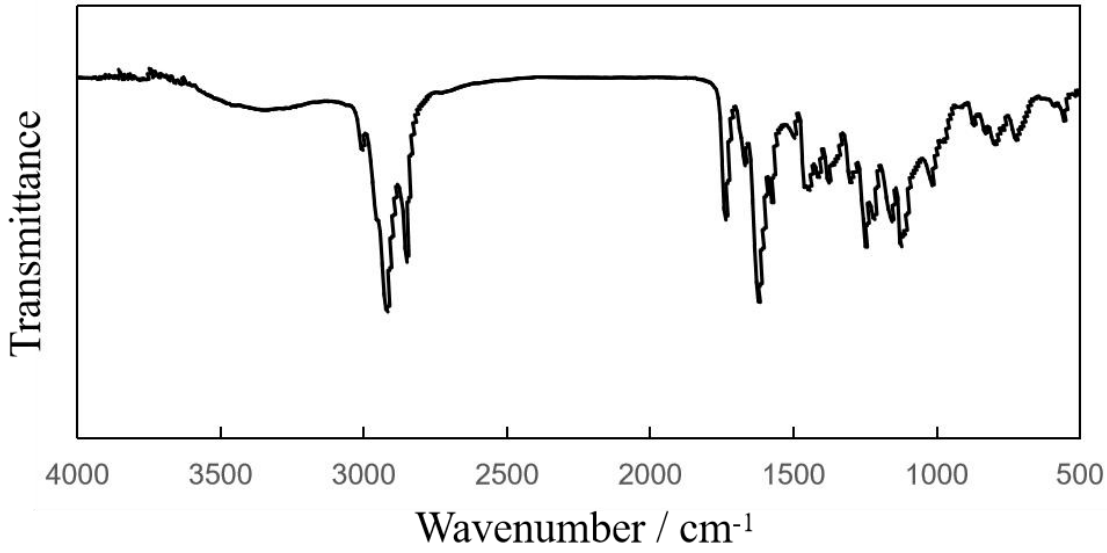

Figure S3. IR spectrum of compound **1**.

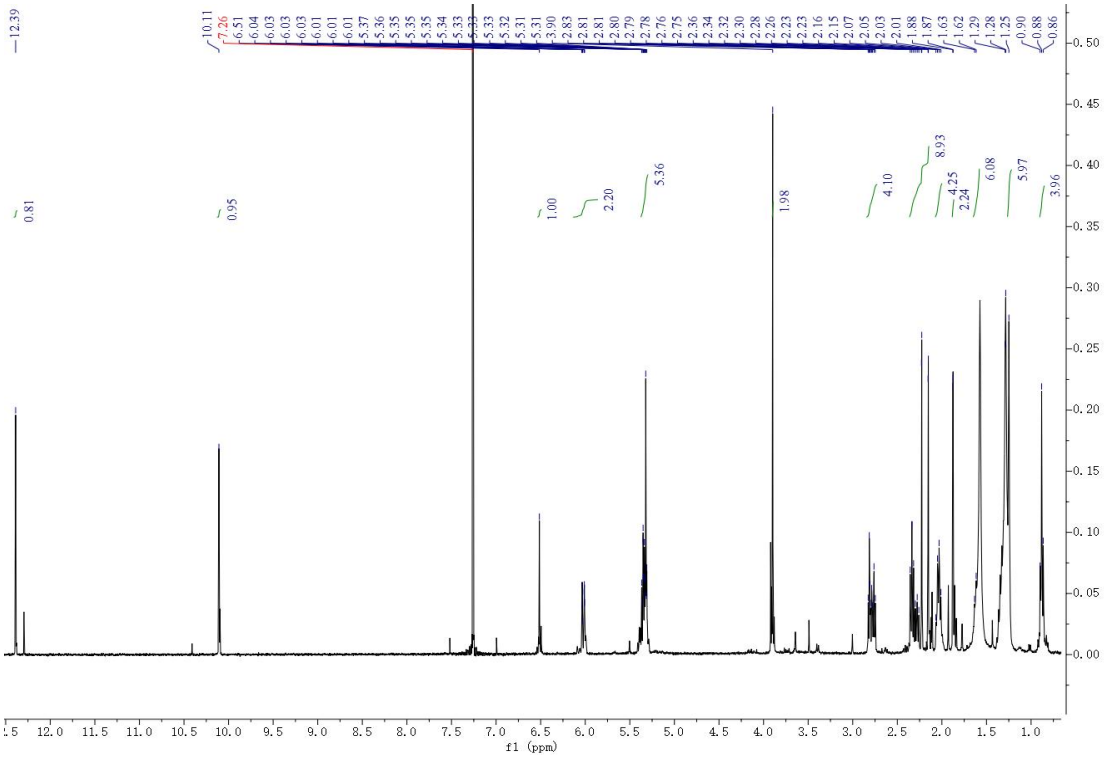

Figure S4. ^{1}H NMR spectrum (400 MHz) of compound **1** in $CDCl_3$.

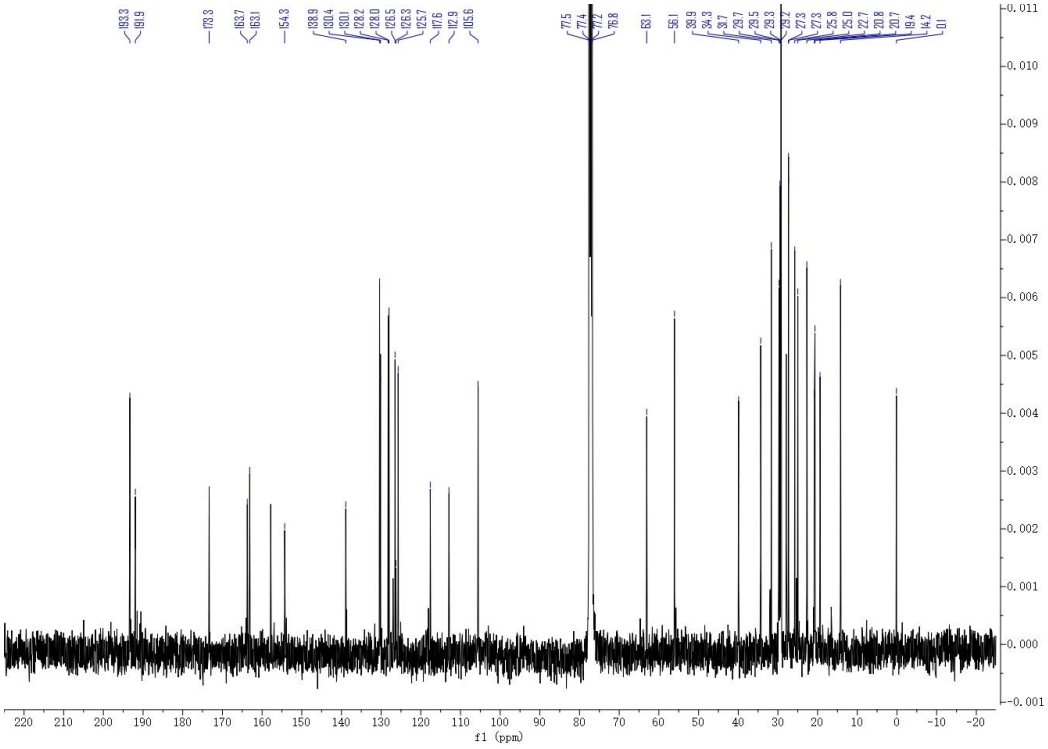

Figure S5. ^{13}C NMR spectrum (100 MHz) of compound **1** in $CDCl_3$.

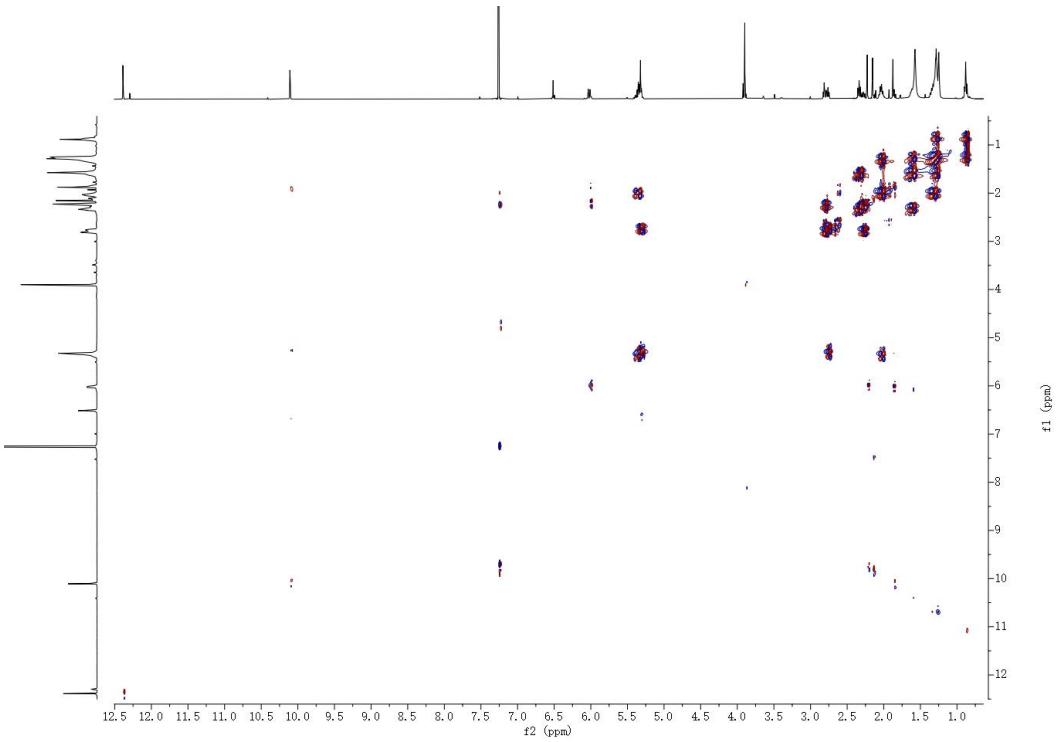

Figure S6. COSY spectrum (400 MHz) of compound **1** in $CDCl_3$.

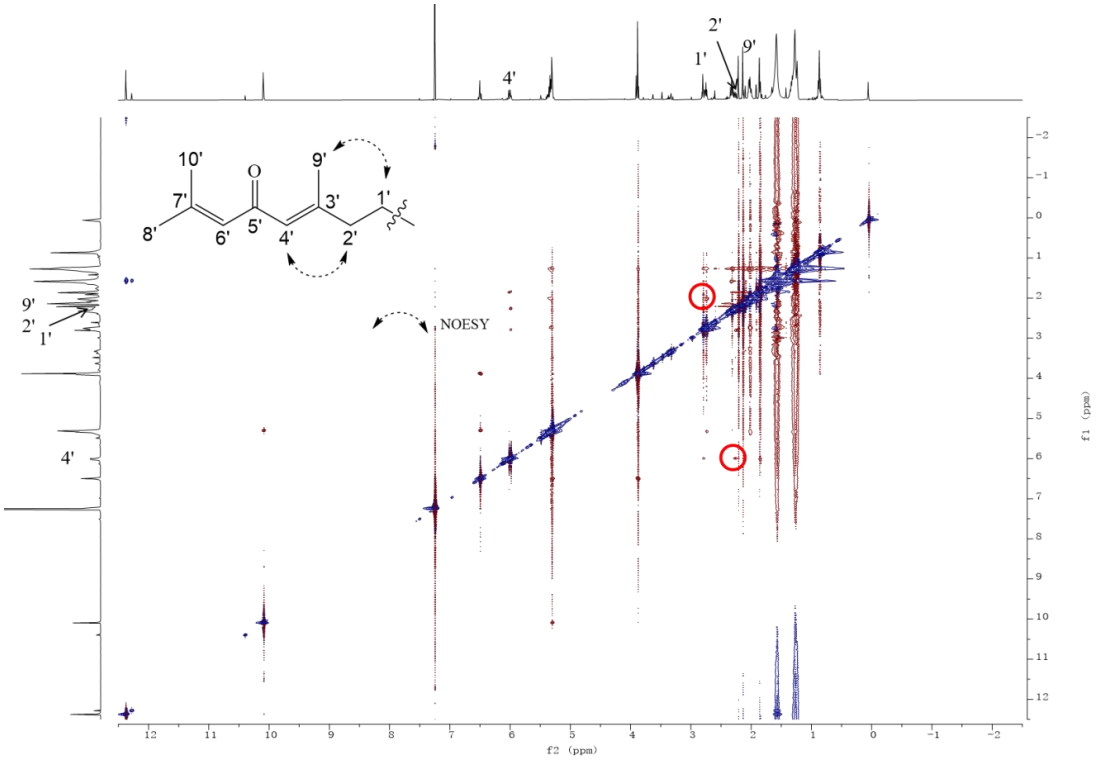

Figure S7. NOESY spectrum (400 MHz) of compound **1** in $CDCl_3$.

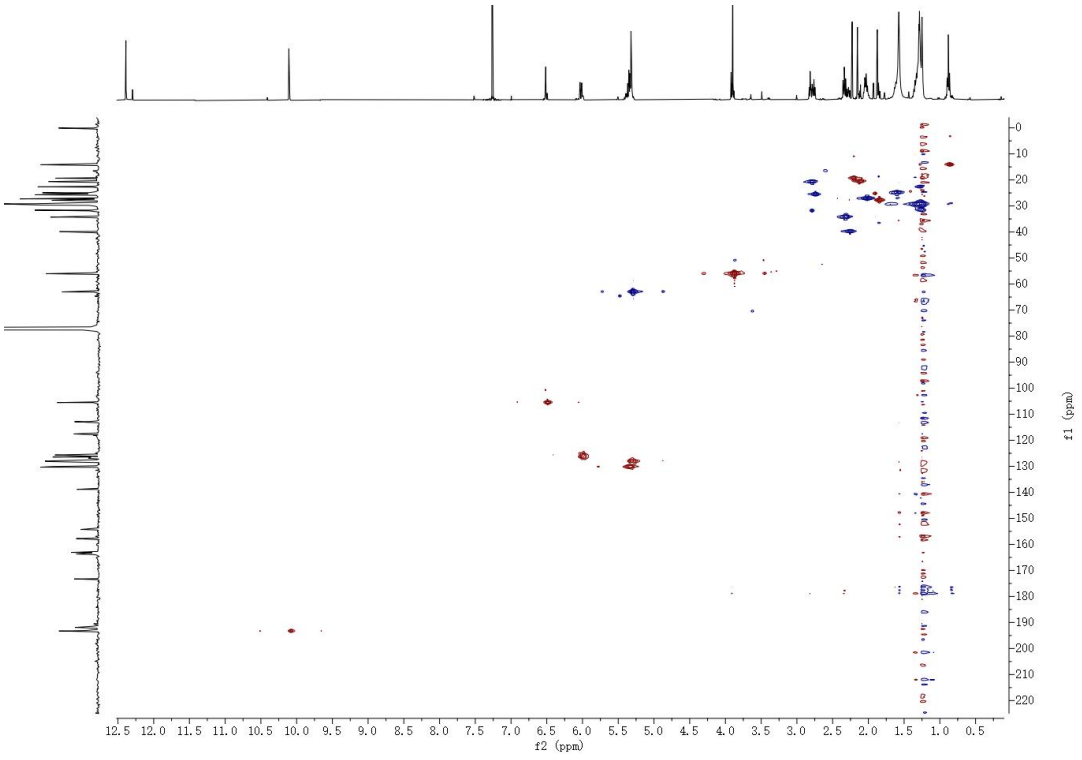

Figure S8. HSQC spectrum of compound **1** in $CDCl_3$.cc

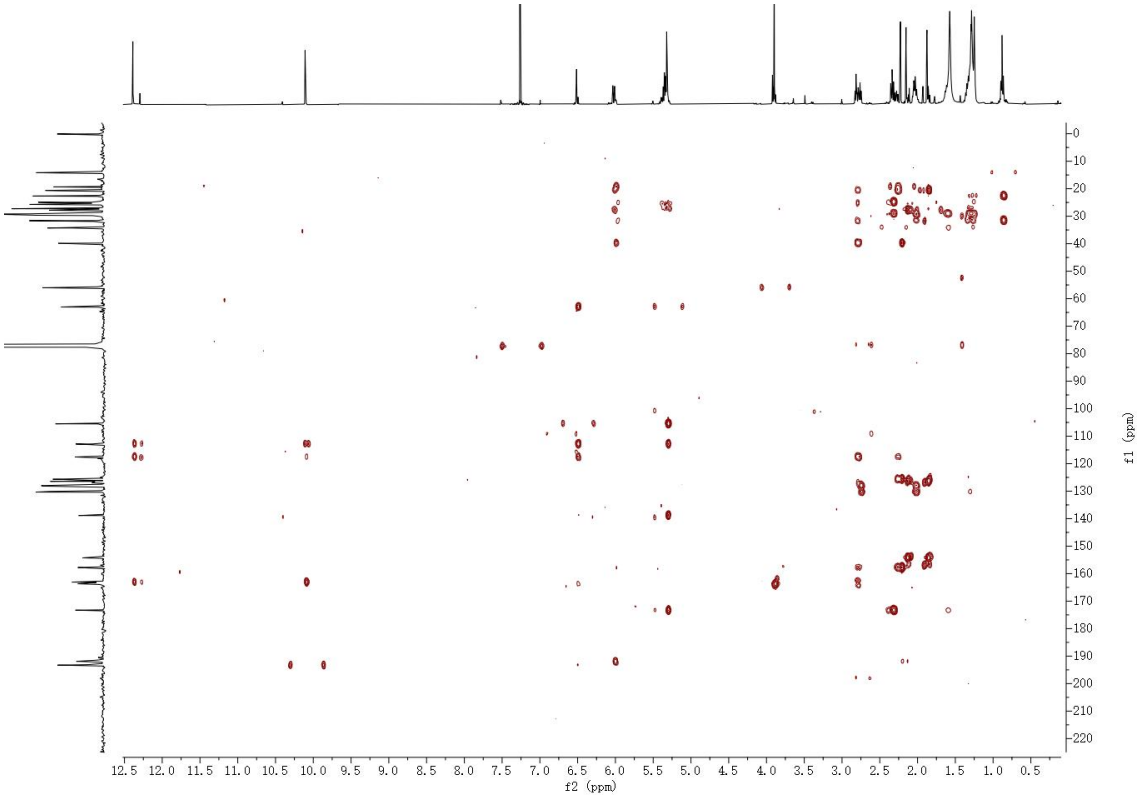

Figure S9. HMBC spectrum of compound **1** in $CDCl_3$.

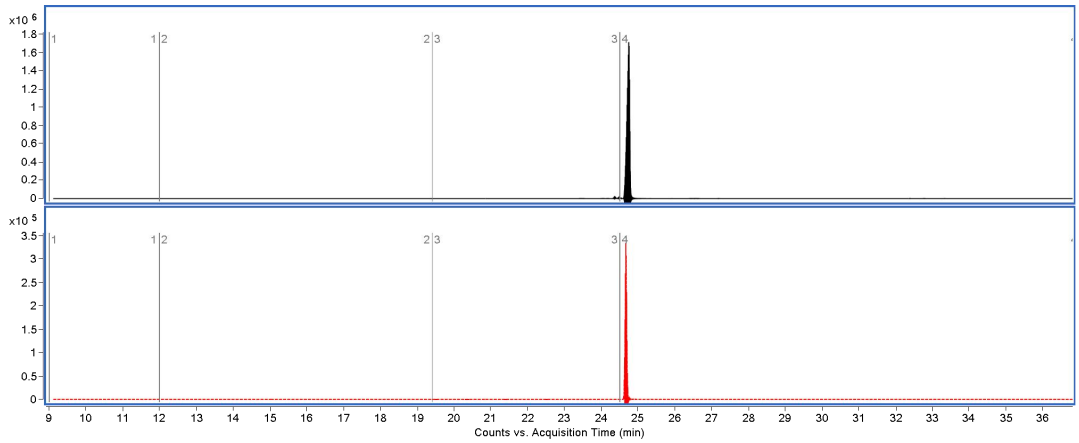

Figure S10. EIC chromatograph of authentic linoleic acid (A) and compound **1** (B) after using hydrolysis kit.

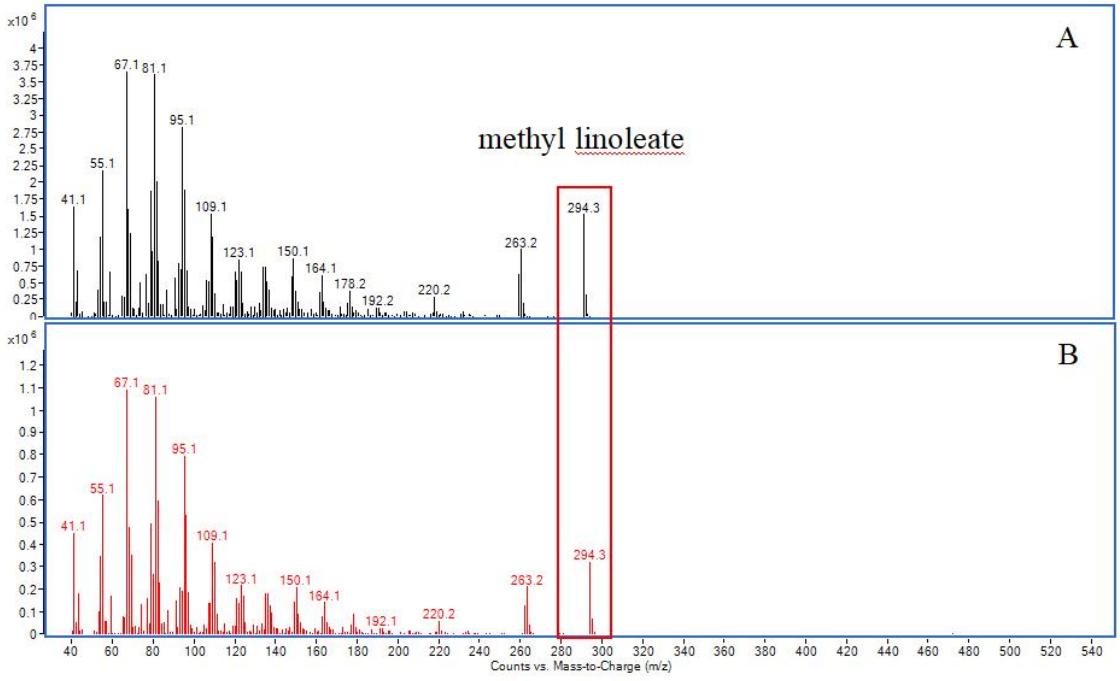

Figure S11. MS spectrum of authentic linoleic acid (A) and compound **1** (B) after using hydrolysis kit.

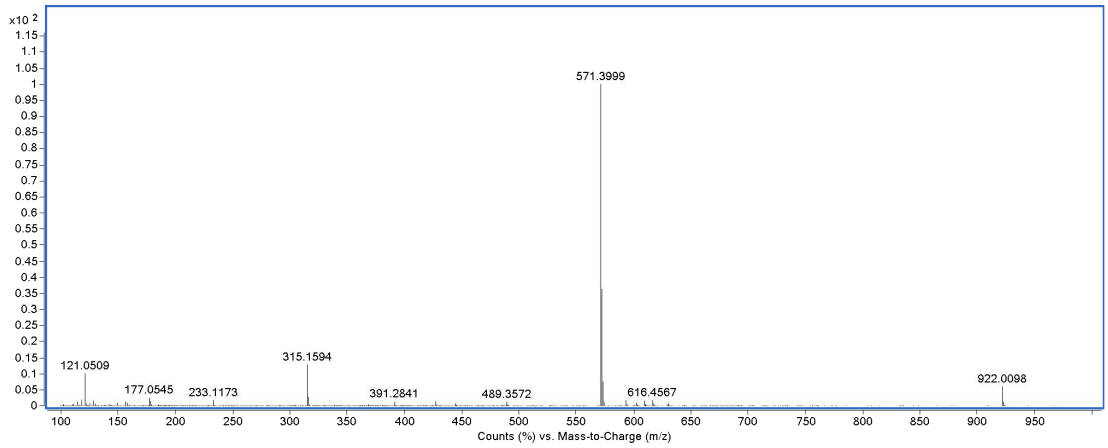

Figure S12. HRESIMS spectrum of compound **2**.

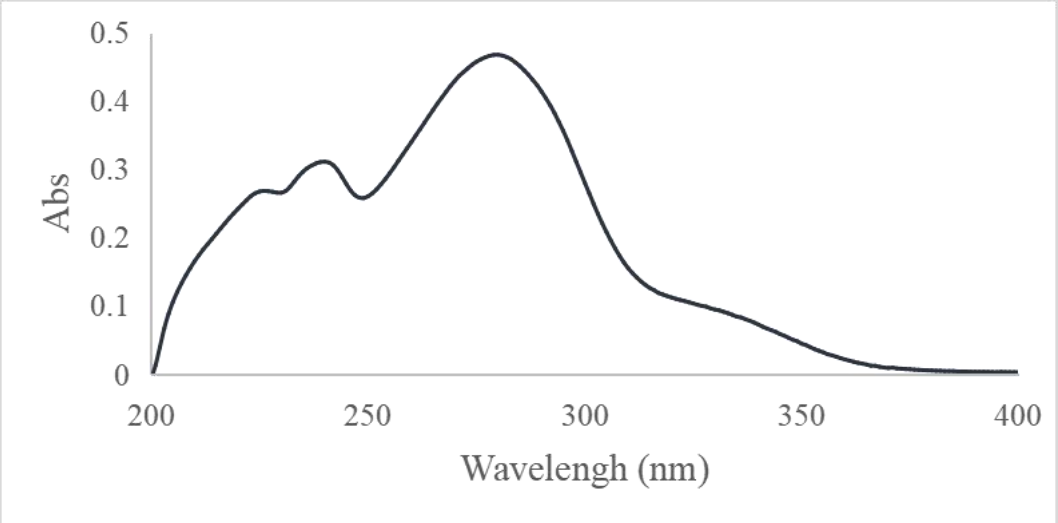

Figure S13. UV spectrum of compound **2**.

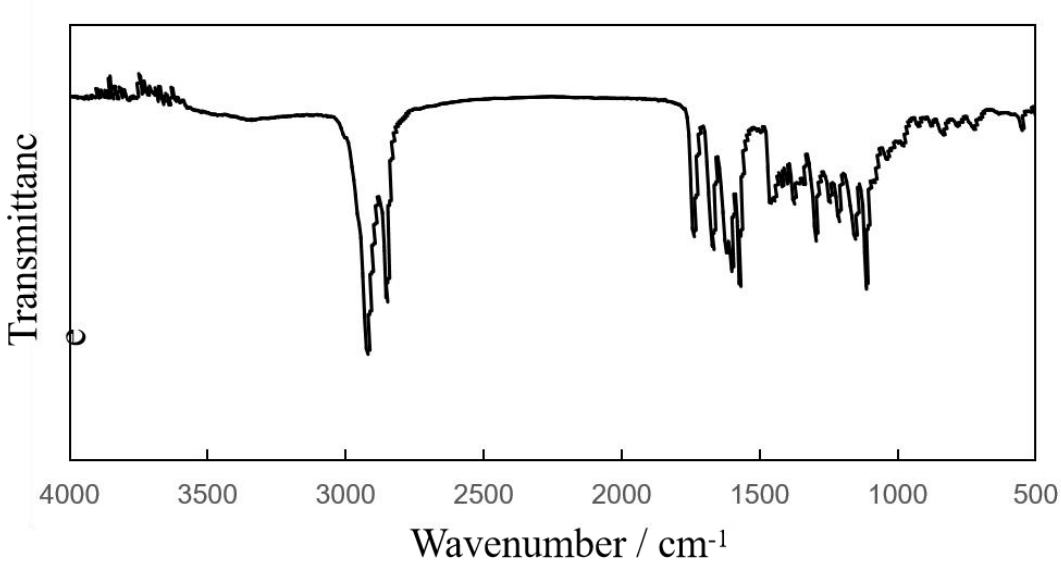

Figure S 14. IR spectrum of compound **2**.

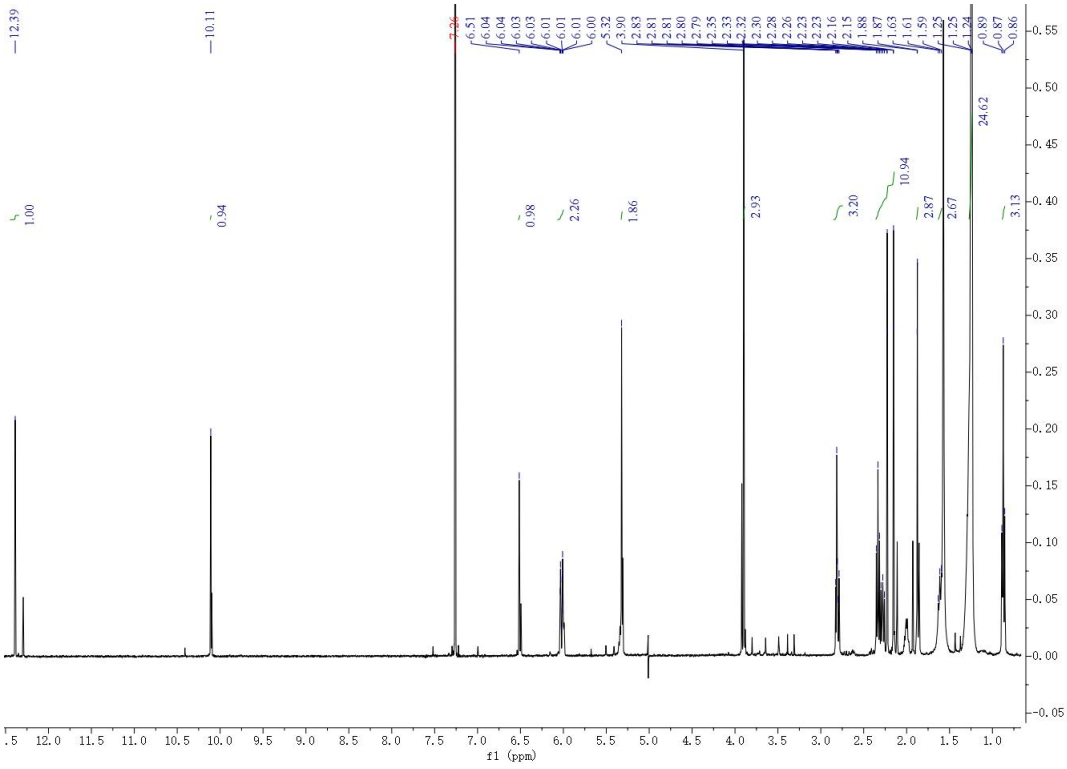

Figure S15. ^{1}H NMR spectrum (400 MHz) of compound **2** in $CDCl_3$.

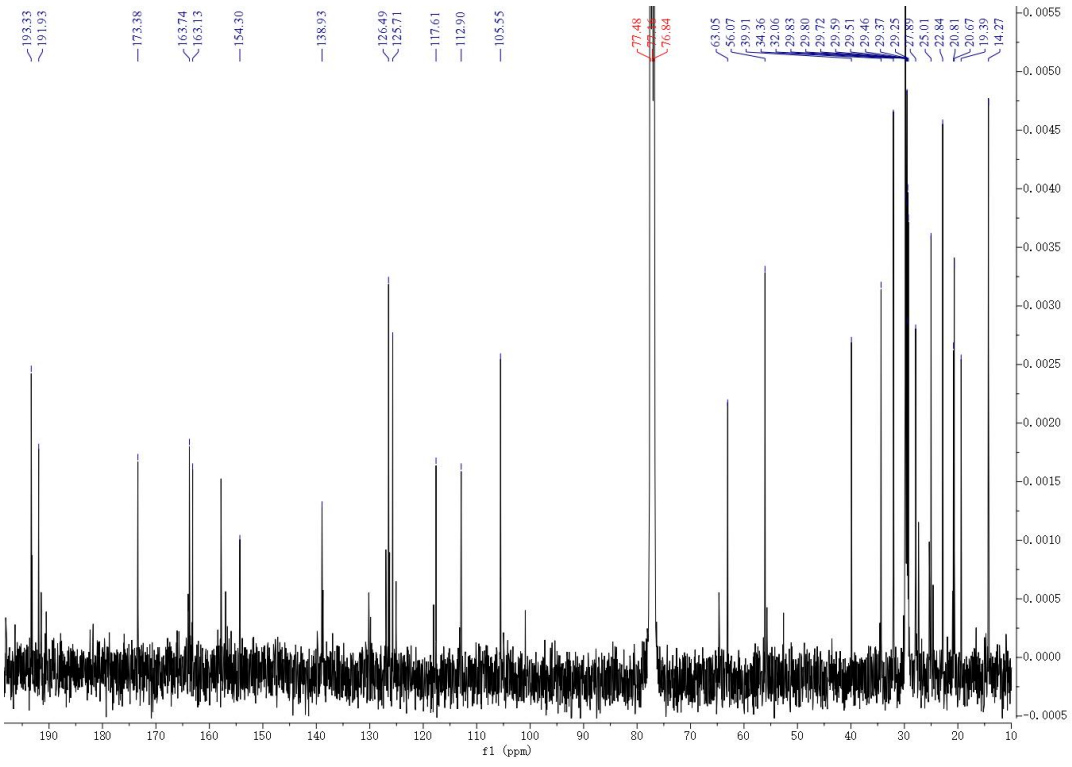

Figure S16. ^{13}C NMR spectrum (100 MHz) of compound **2** in $CDCl_3$.

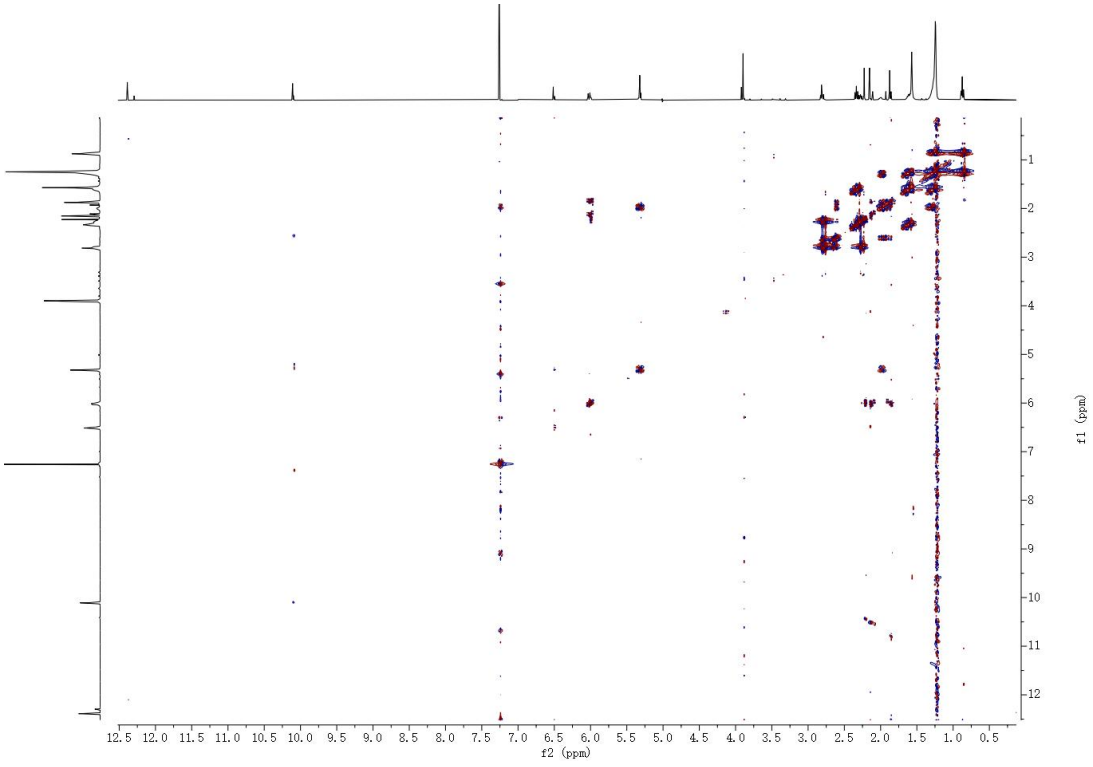

Figure S17. COSY spectrum (400 MHz) of compound **2** in $CDCl_3$.

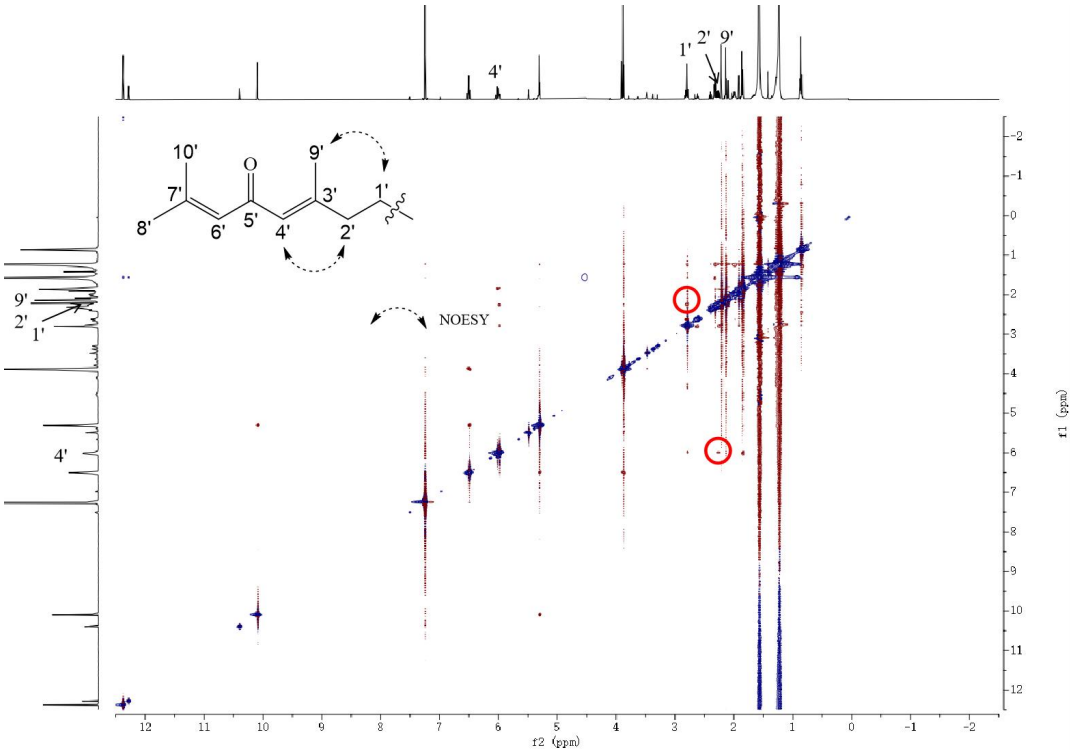

Figure S18. NOESY spectrum (400 MHz) of compound **2** in $CDCl_3$.

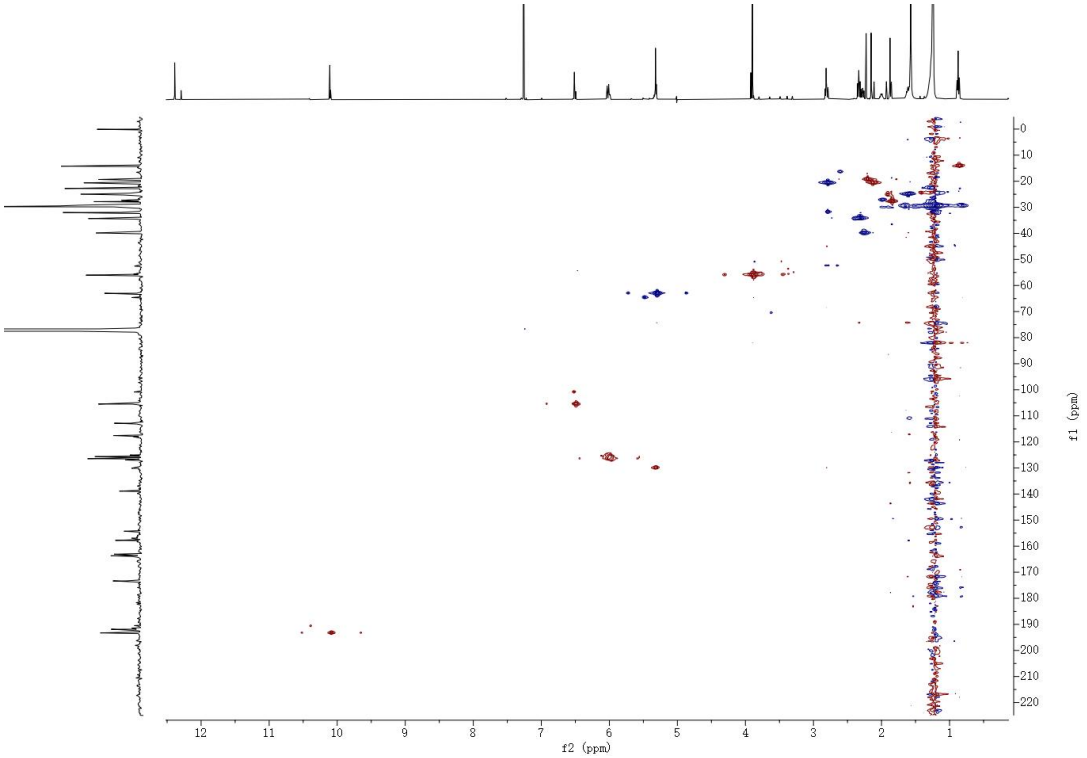

Figure S19. HSQC spectrum of compound **2** in $CDCl_3$.

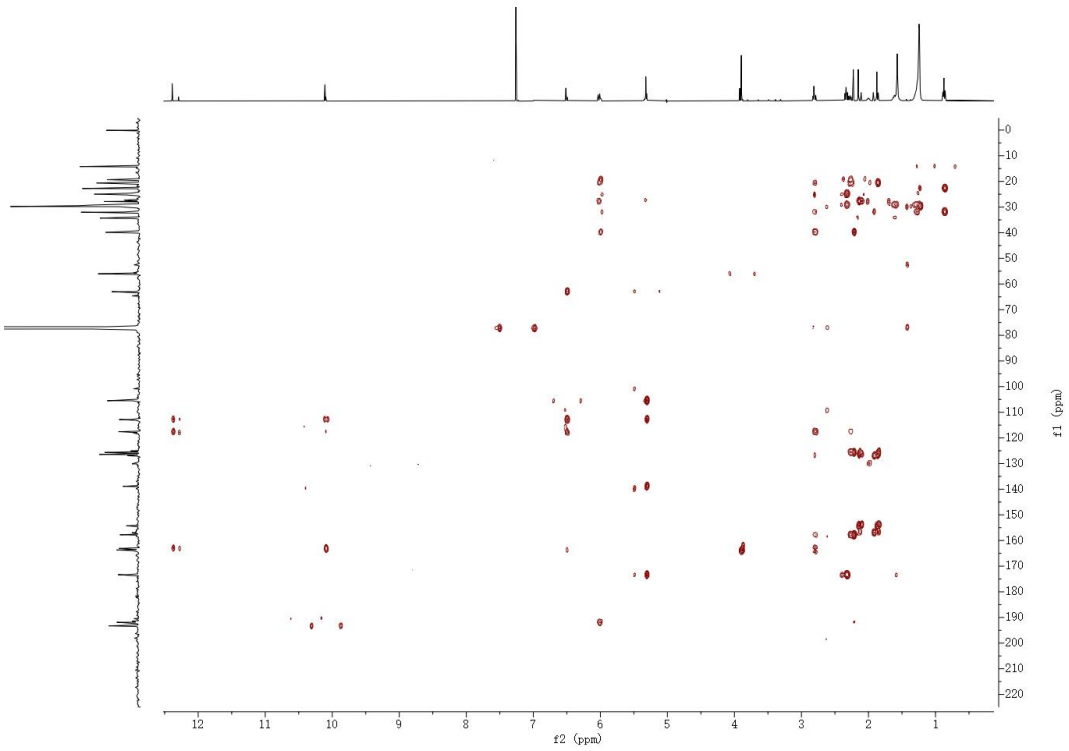

Figure S20. HMBC spectrum of compound **2** in $CDCl_3$.

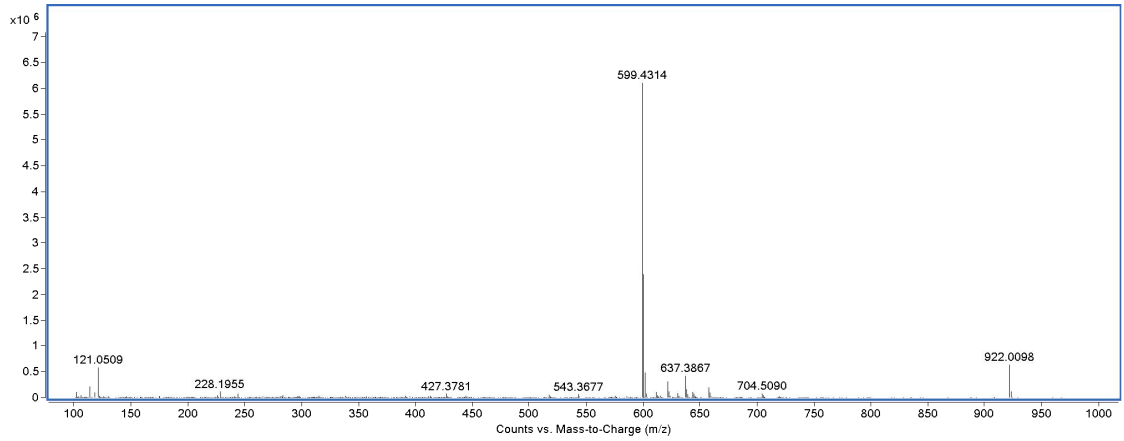

Figure S21. HRESIMS spectrum of compound **3**.

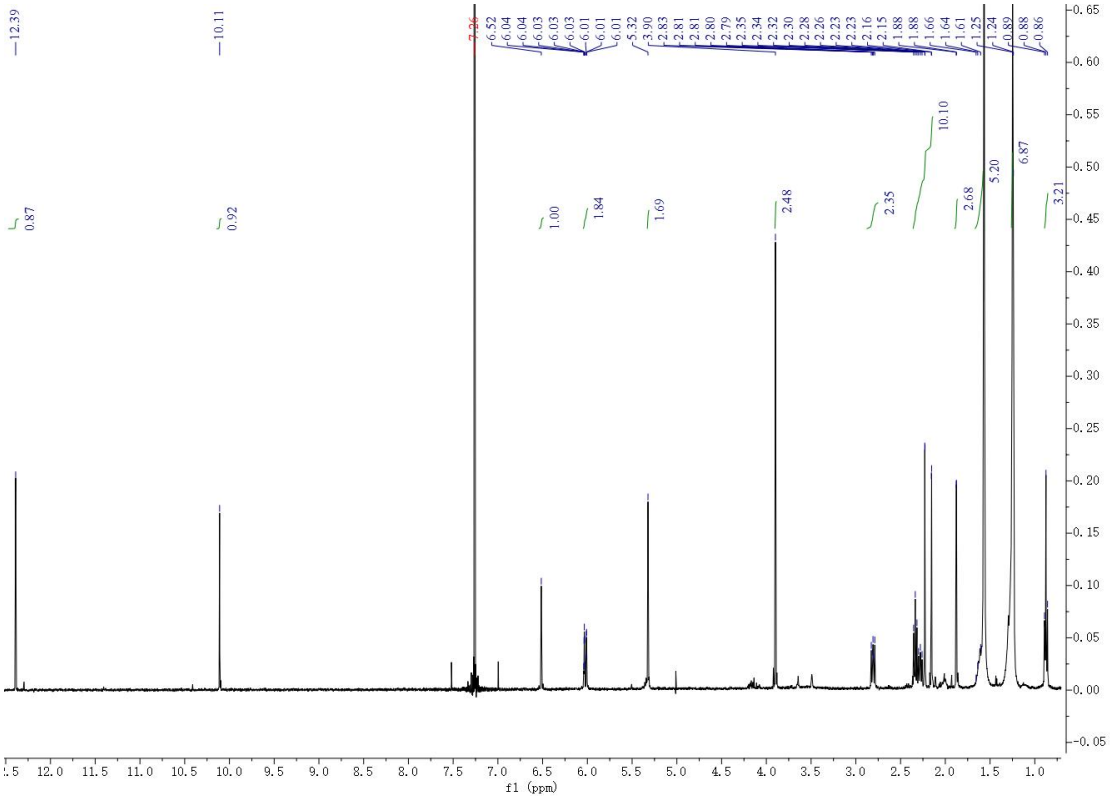

Figure S22. ^{1}H NMR spectrum (400 MHz) of compound **3** in $CDCl_3$.

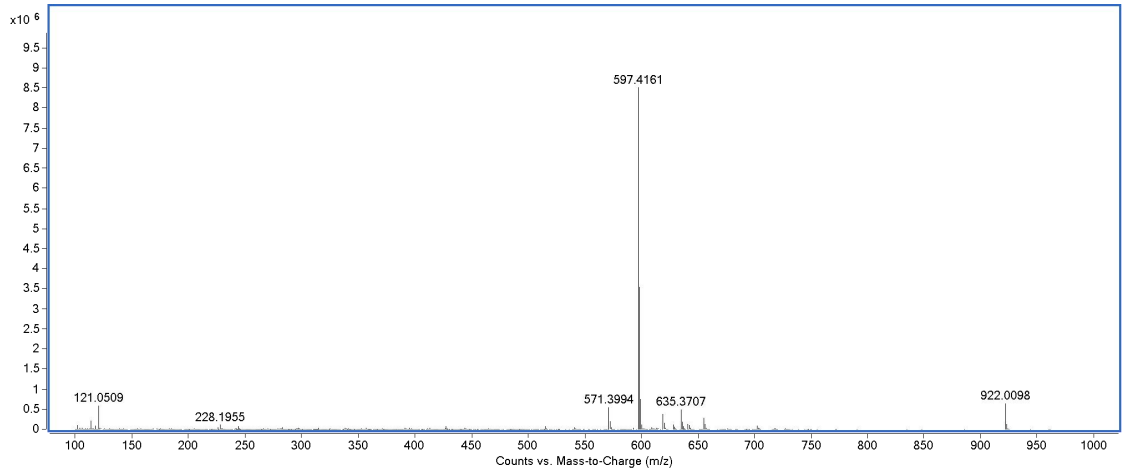

Figure S23. HRESIMS spectrum of compound **4**.

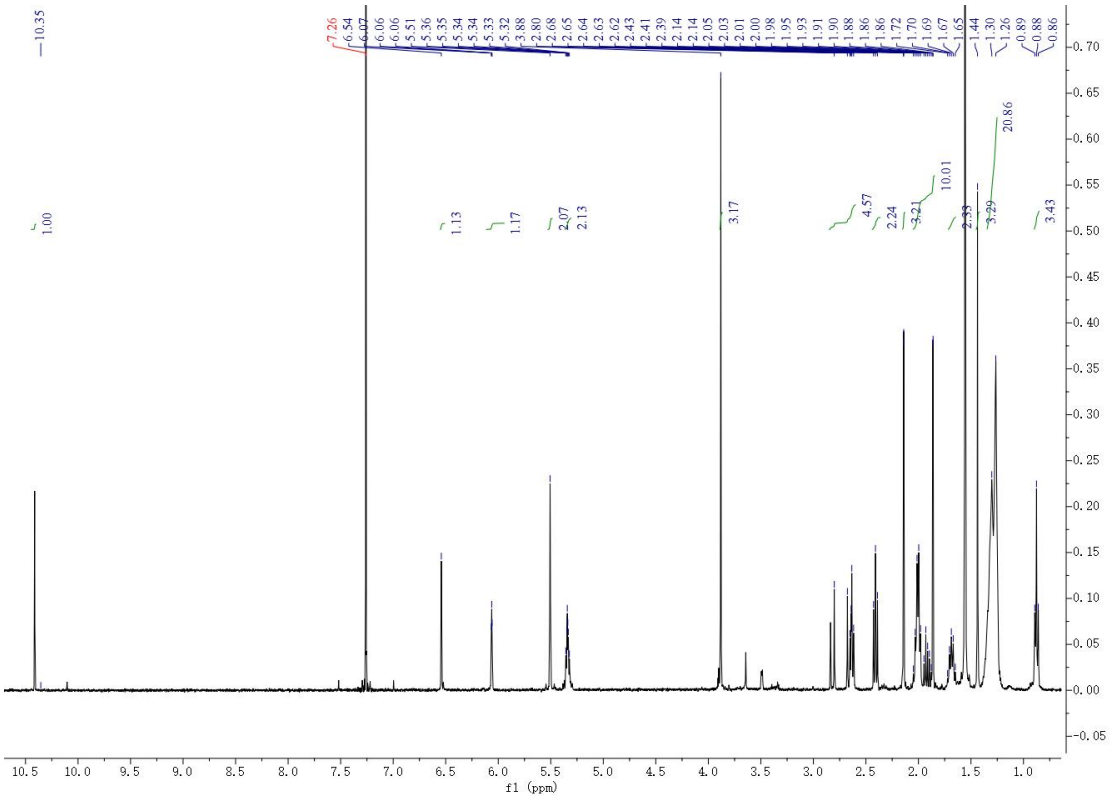

Figure S24. ^{1}H NMR spectrum (400 MHz) of compound **4** in $CDCl_3$.

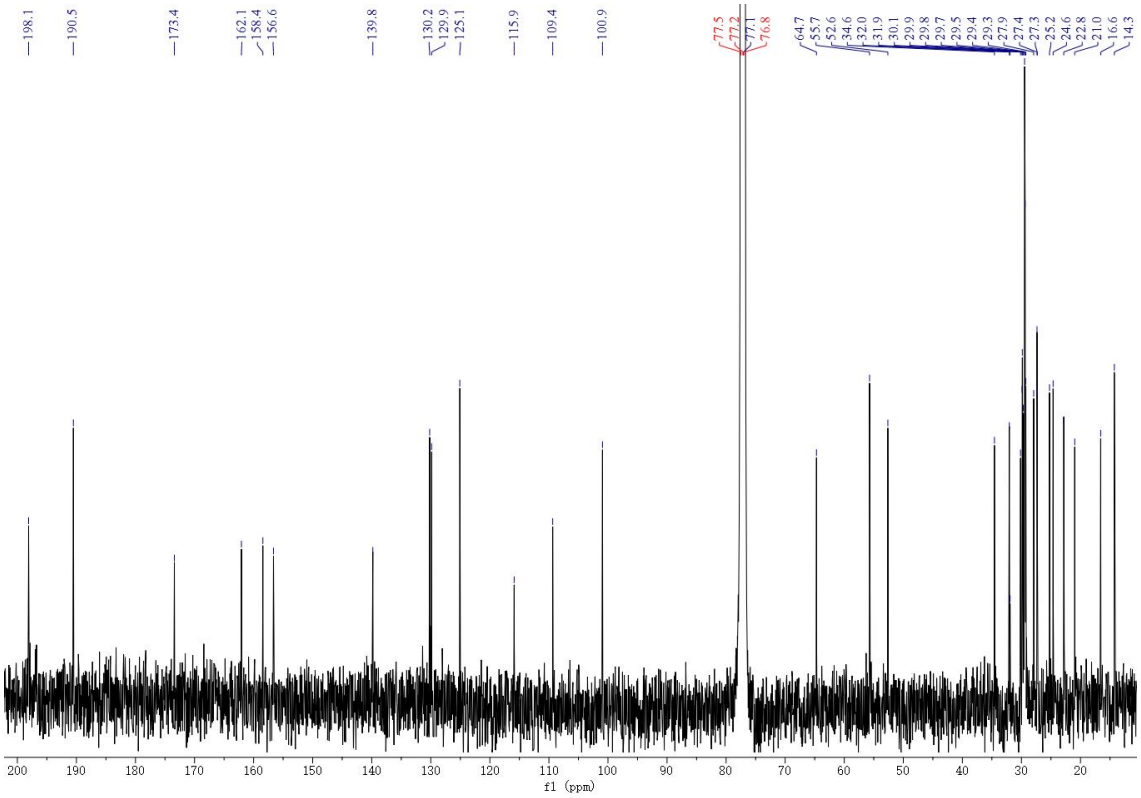

Figure S25. ^{13}C NMR spectrum (100 MHz) of compound **4** in $CDCl_3$.

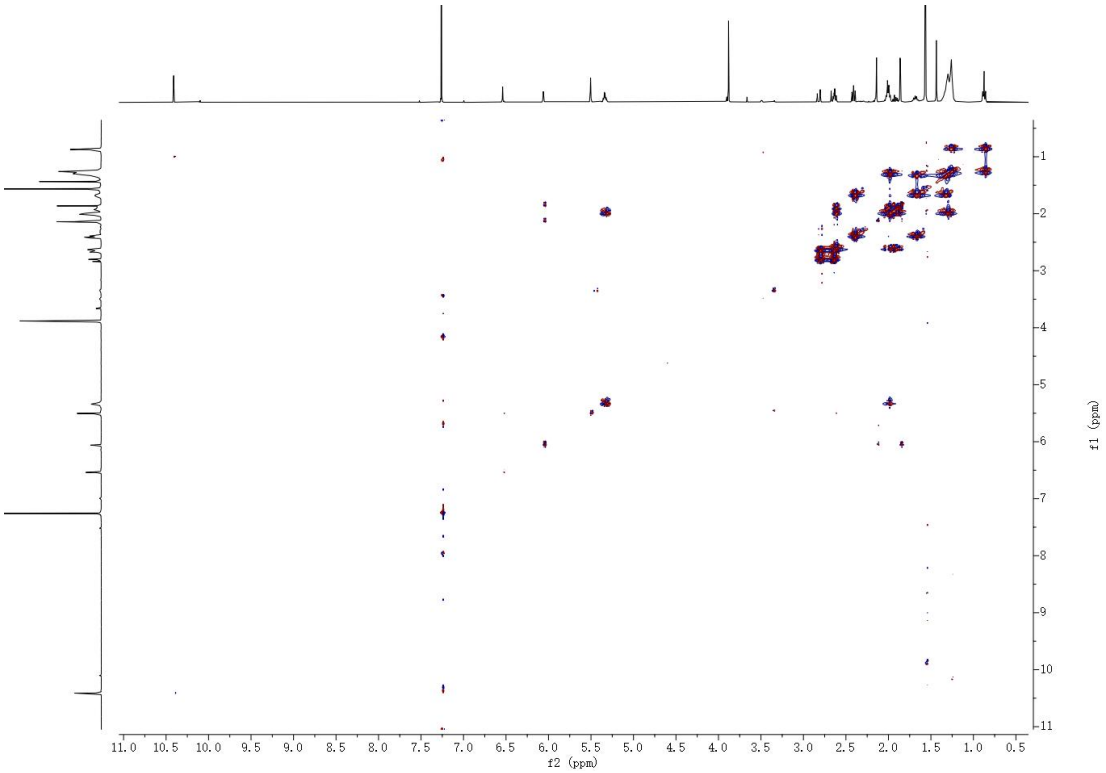

Figure S26. COSY spectrum (400 MHz) of compound **4** in $CDCl_3$.

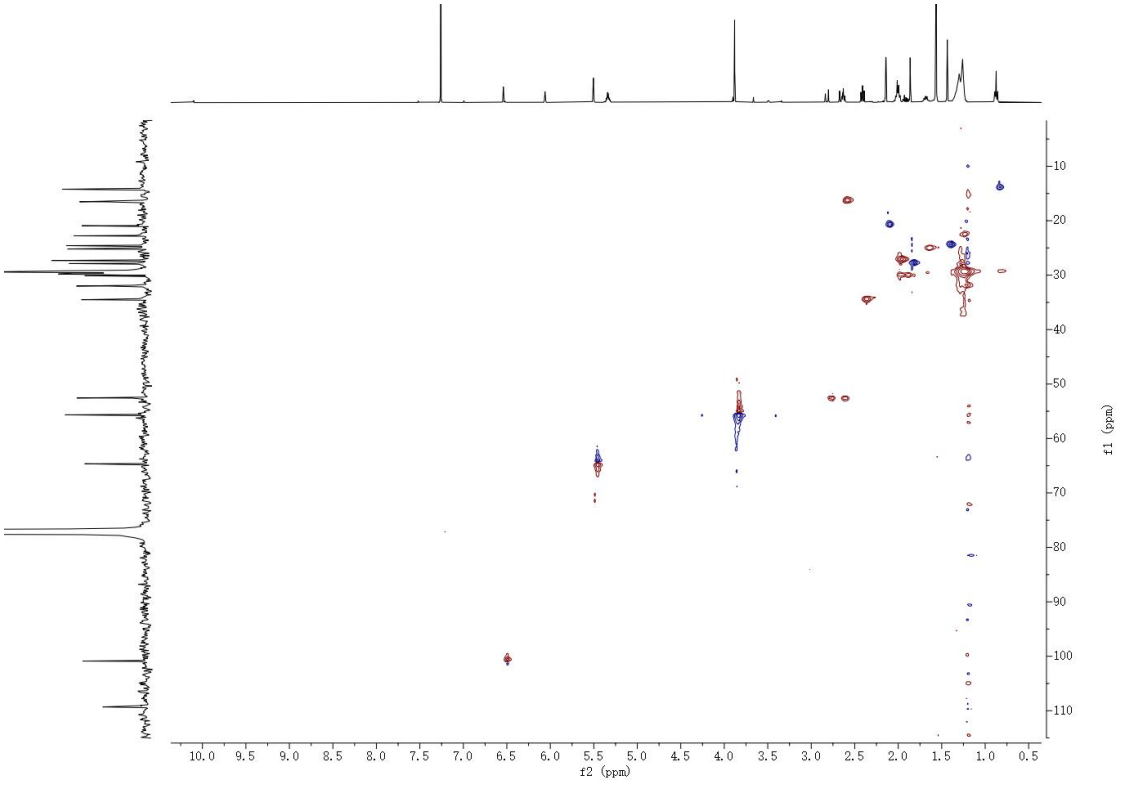

Figure S27. HSQC spectrum of compound **4** in $CDCl_3$.

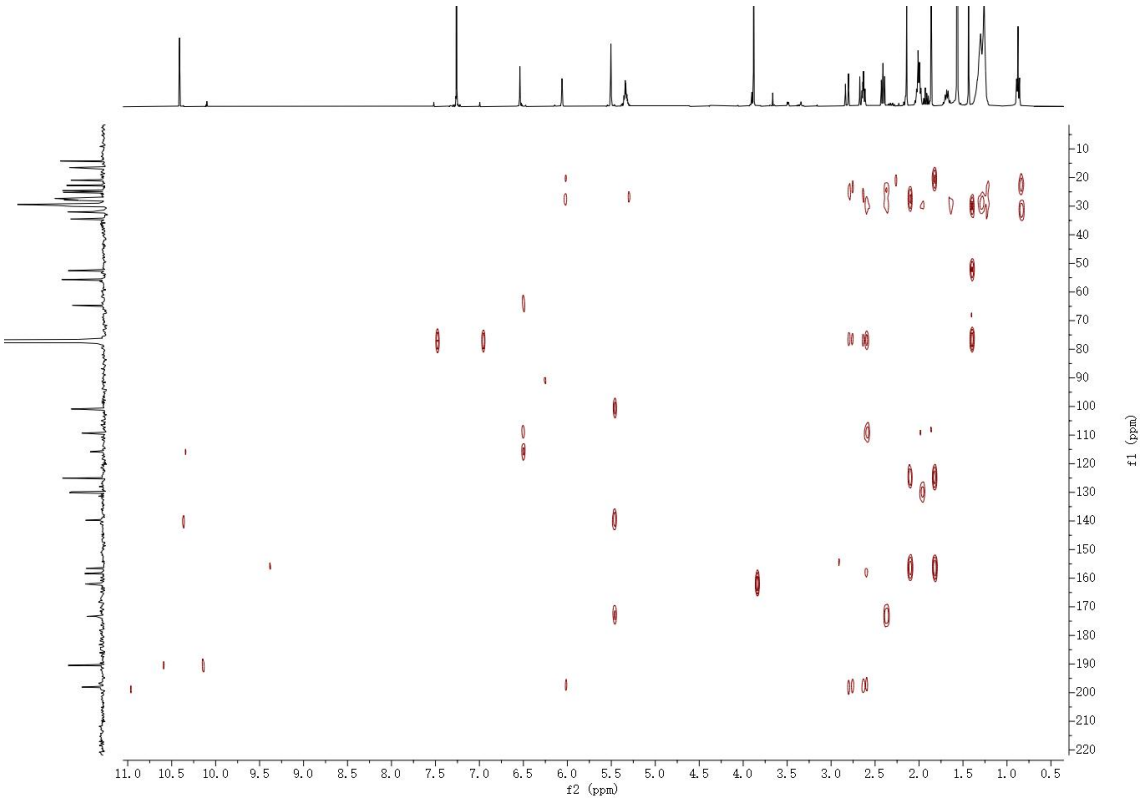

Figure S28. HMBC spectrum of compound **4** in $CDCl_3$.

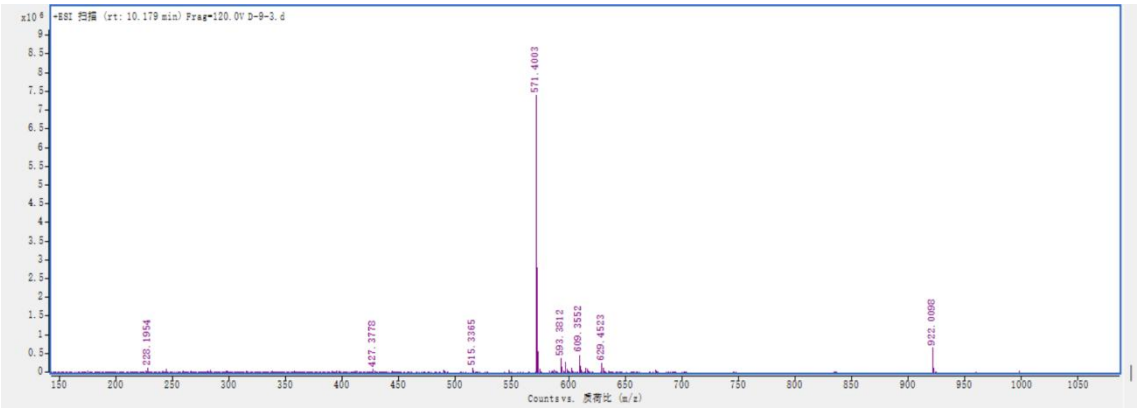

Figure S29. HRESIMS spectrum of compound **5**.

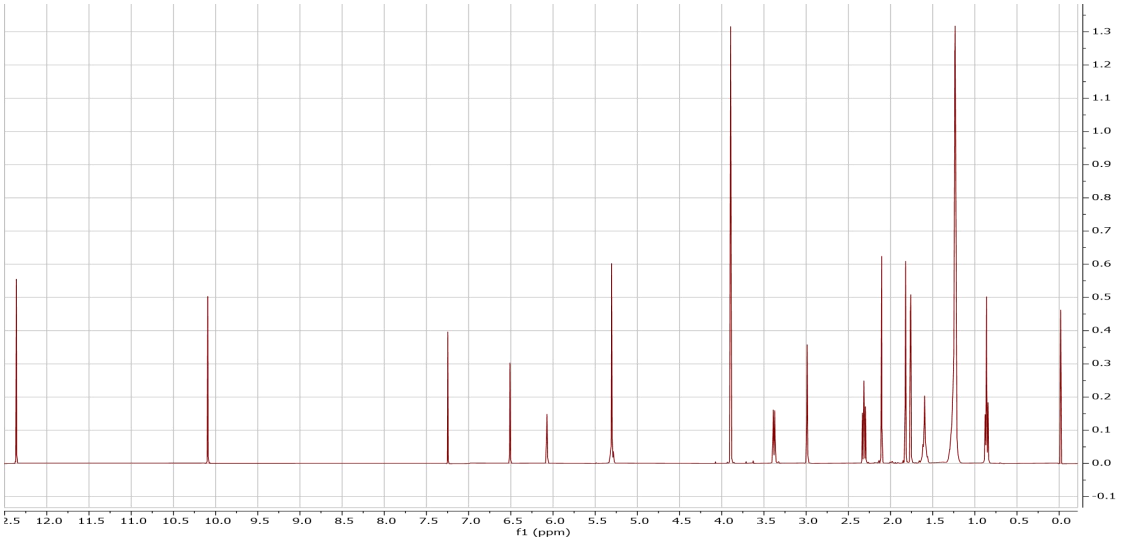

Figure S30. ^{1}H NMR spectrum (400 MHz) of compound **5** in $CDCl_3$.

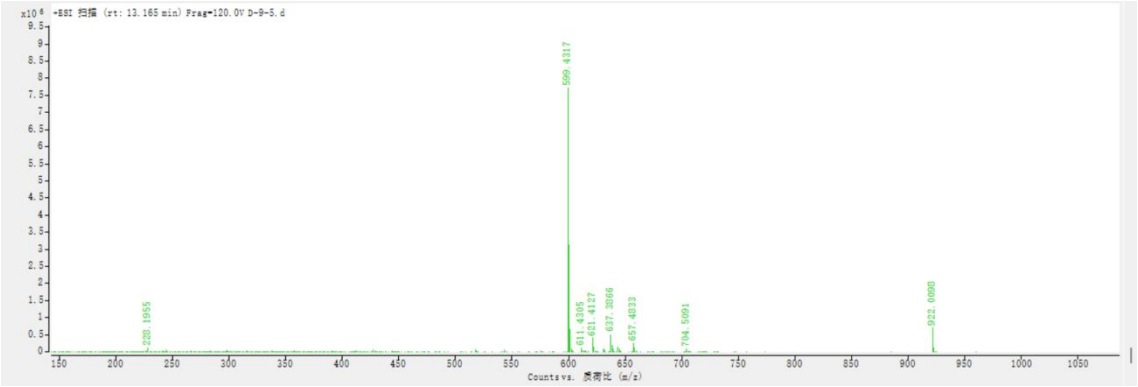

Figure S31. HRESIMS spectrum of compound 6.

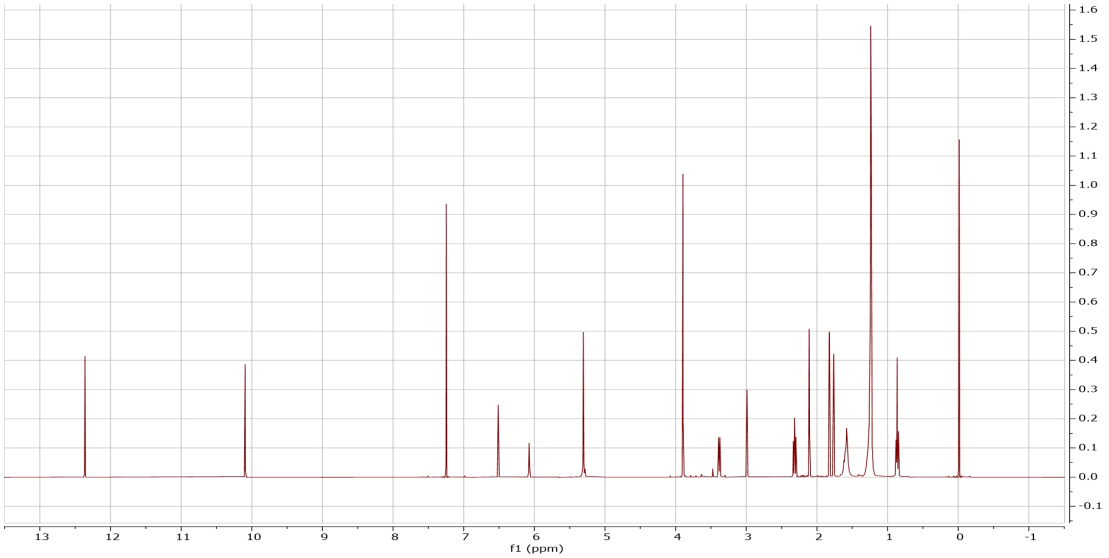

Figure S32. ^{1}H NMR spectrum (400 MHz) of compound **6** in $CDCl_3$.\

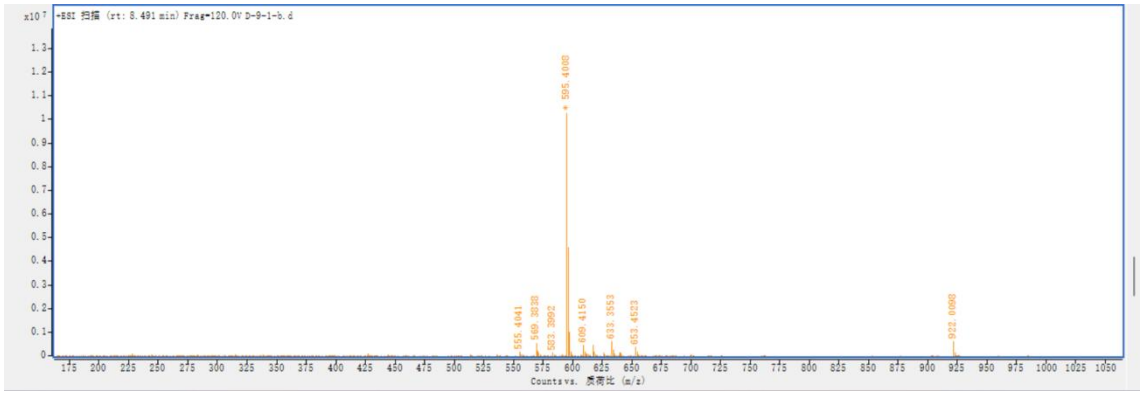

Figure S33. HRESIMS spectrum of compound **7**.

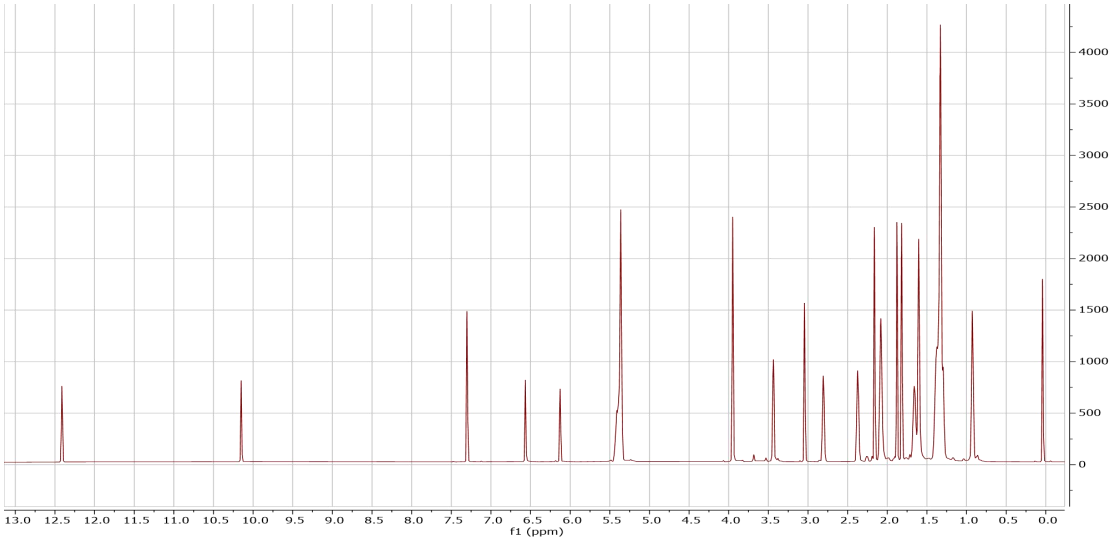

Figure S34. ^{1}H NMR spectrum (400 MHz) of compound **7** in $CDCl_3$.

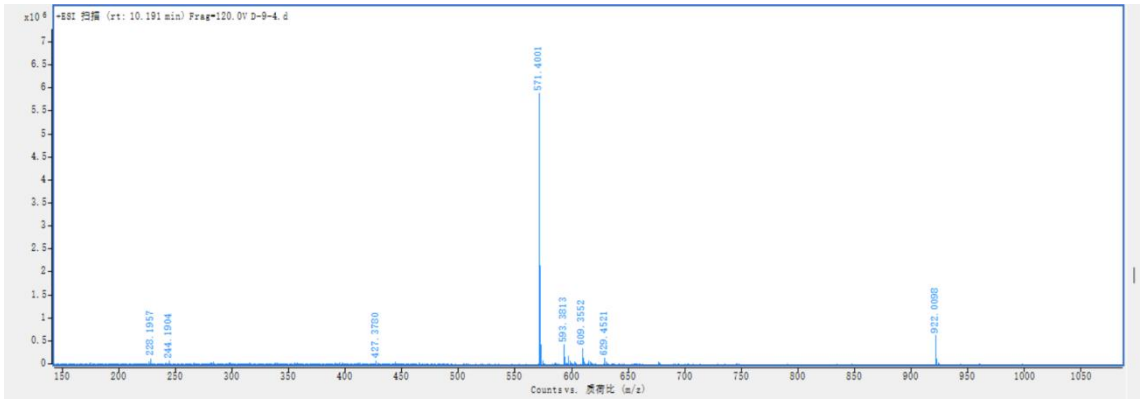

Figure S35. HRESIMS spectrum of compound **8**.

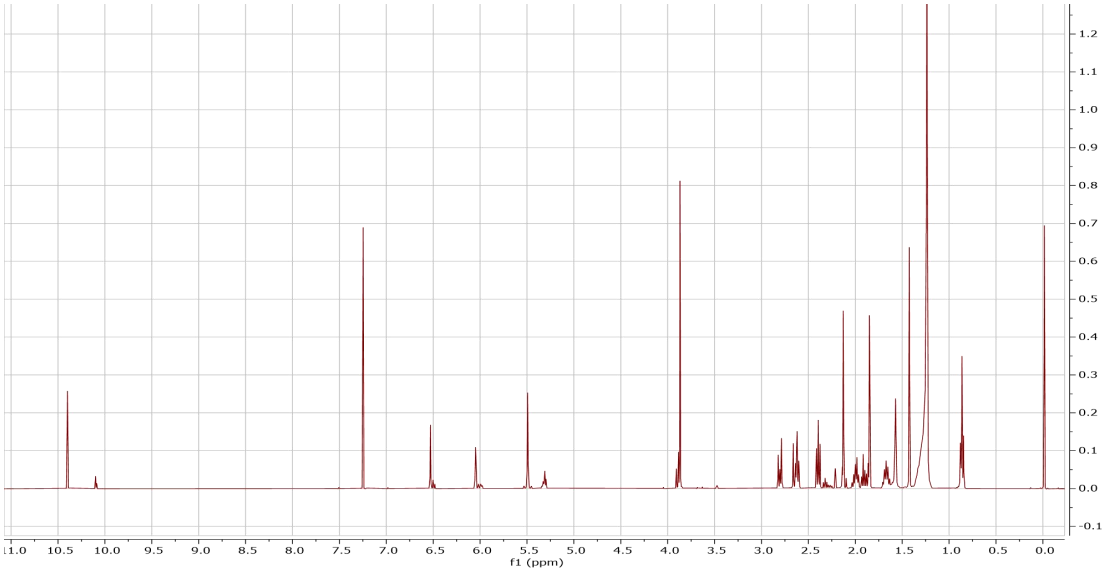

Figure S36. ^{1}H NMR spectrum (400 MHz) of compound **8** in $CDCl_3$.

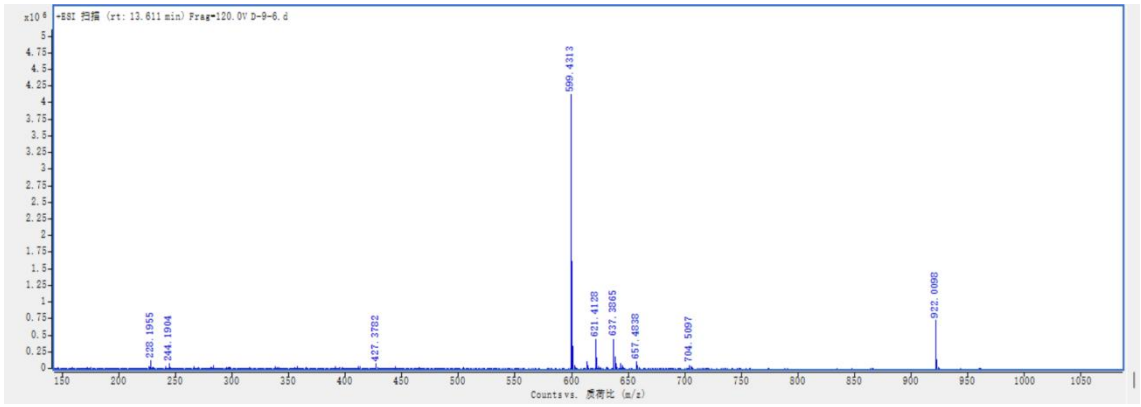

Figure S37. HRESIMS spectrum of compound **9**.

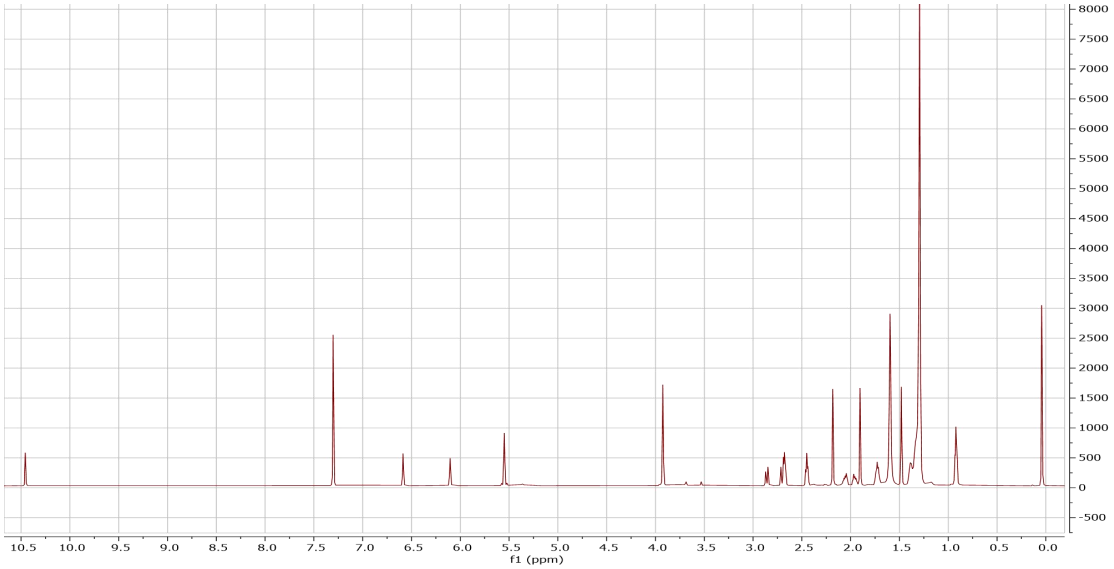

Figure S38. ^{1}H NMR spectrum (400 MHz) of compound **9** in $CDCl_3$.

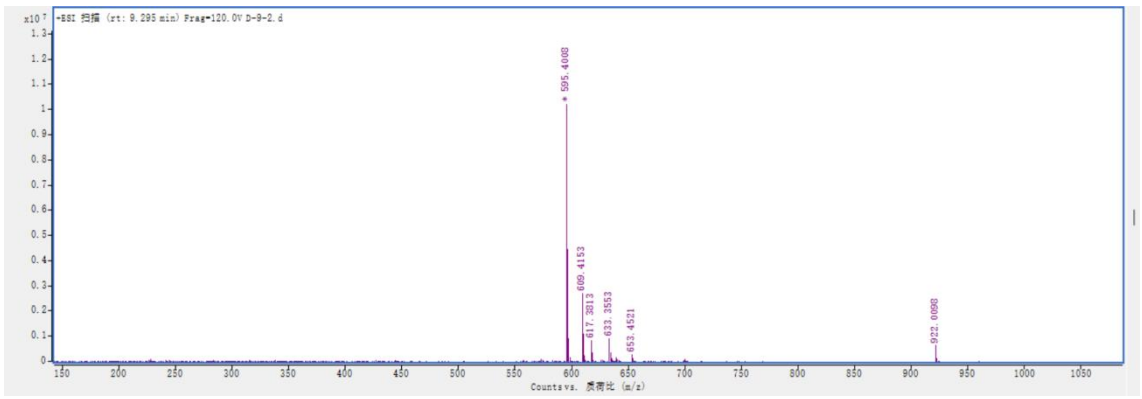

Figure S39. HRESIMS spectrum of compound **10**.

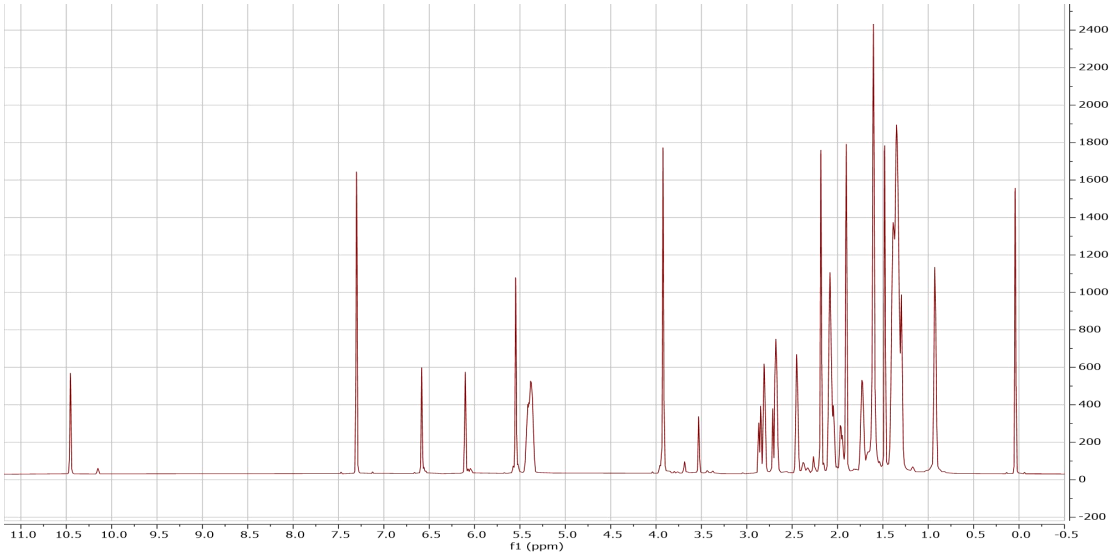

Figure S40. ^{1}H NMR spectrum (400 MHz) of compound **10** in $CDCl_3$.

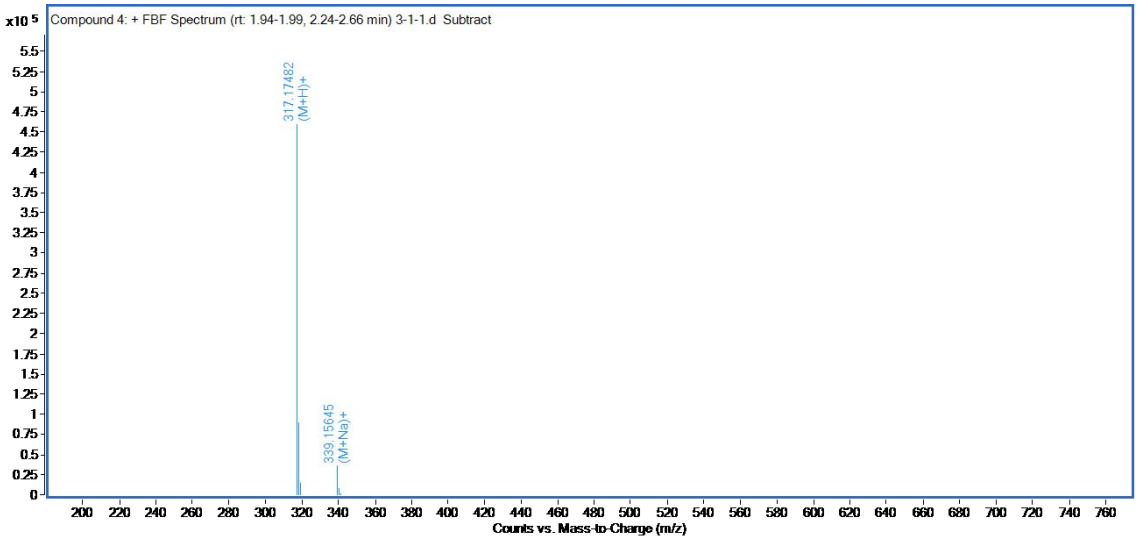

Figure S41. HRESIMS spectrum of compound **12**.

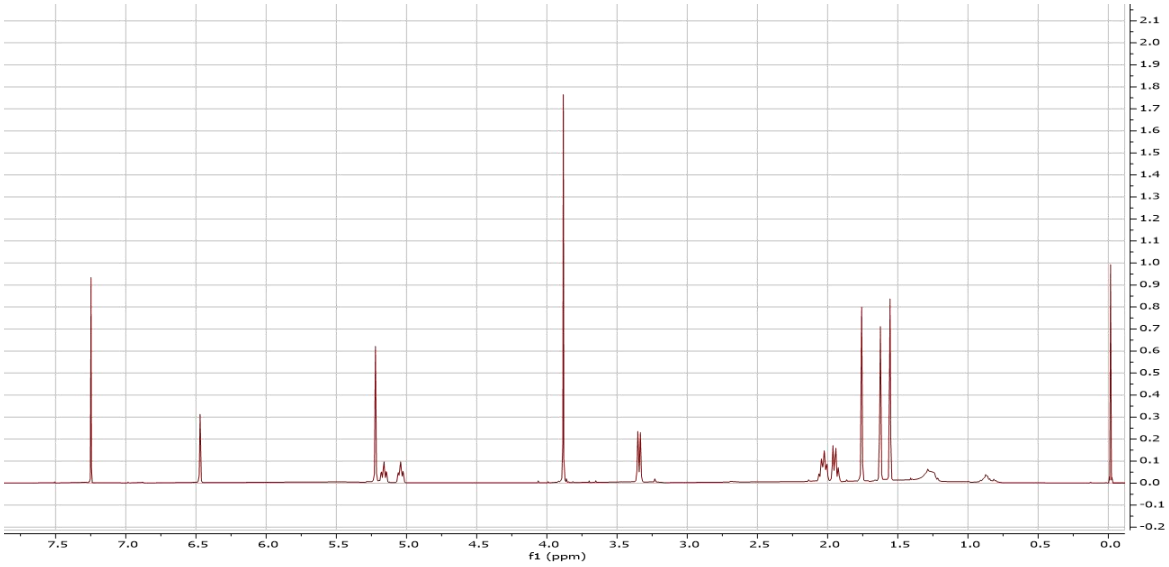

Figure S42. ^{1}H NMR spectrum (400 MHz) of compound **12** in $CDCl_3$.

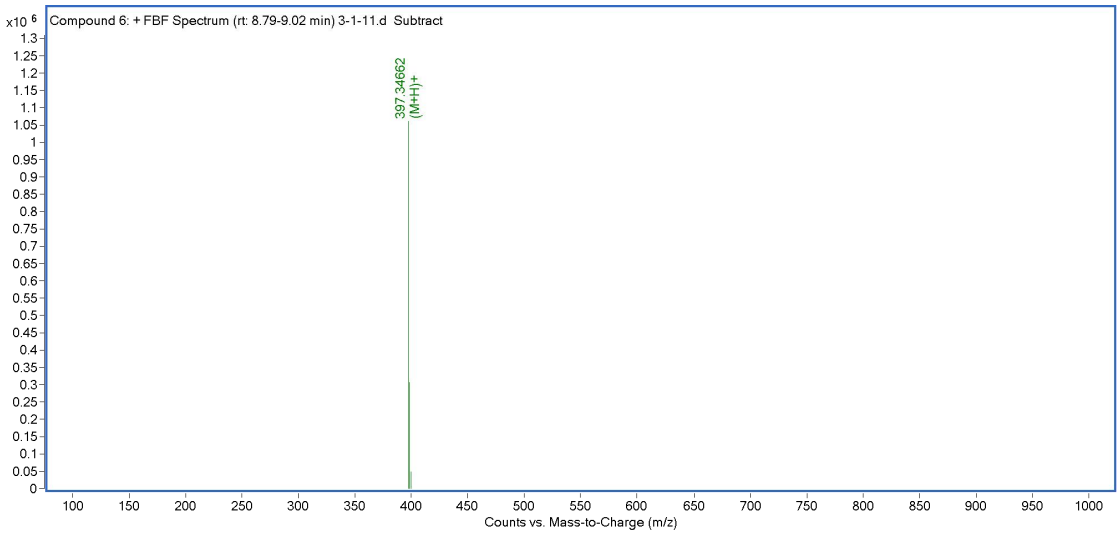

Figure S43. HRESIMS spectrum of compound 13.

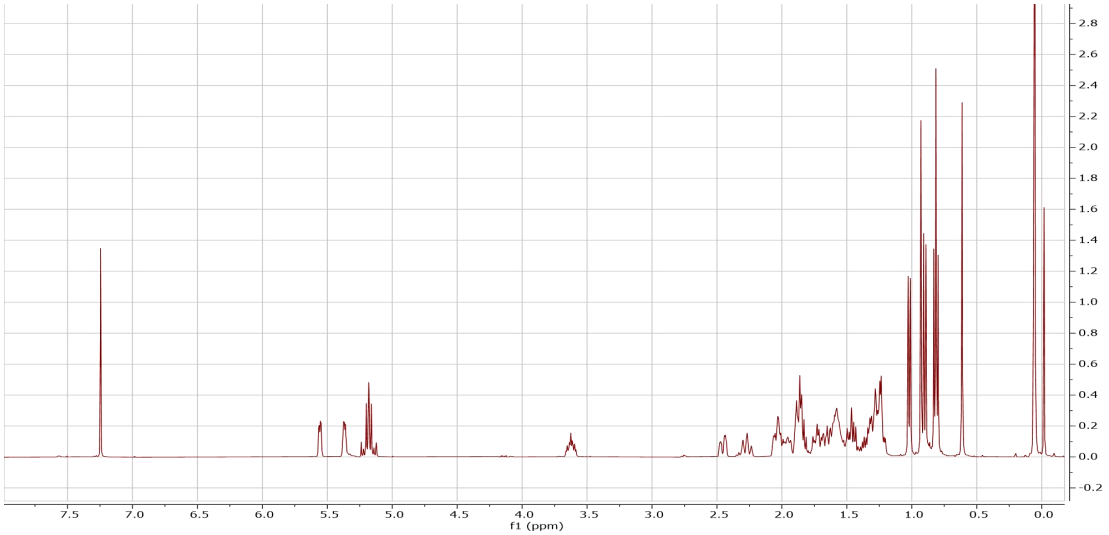

Figure S44. ^{1}H NMR spectrum (400 MHz) of compound **13** in $CDCl_3$

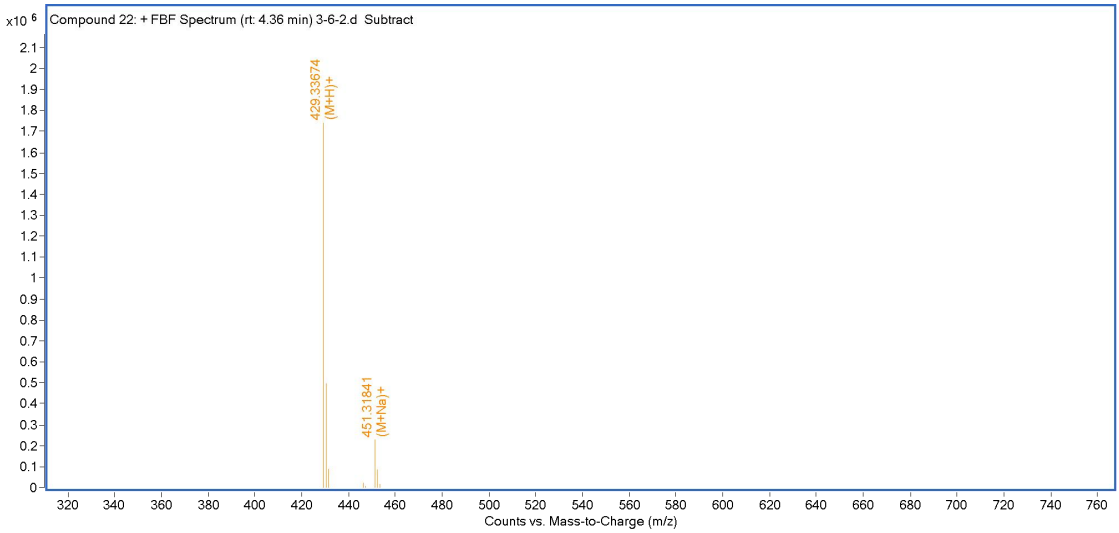

Figure S45. HRESIMS spectrum of compound **14**.

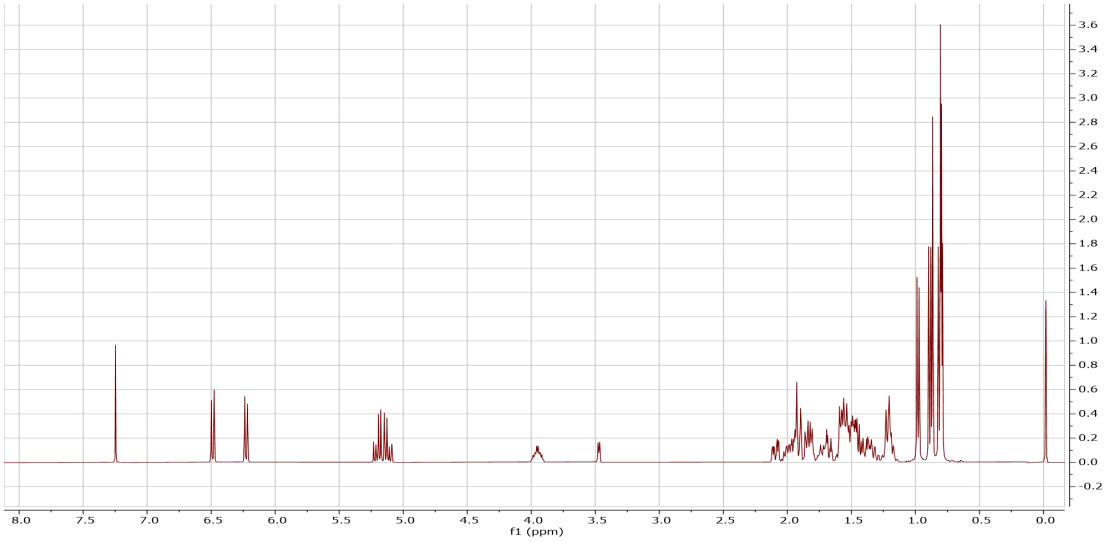

Figure S46. ^{1}H NMR spectrum (400 MHz) of compound **14** in $CDCl_3$.

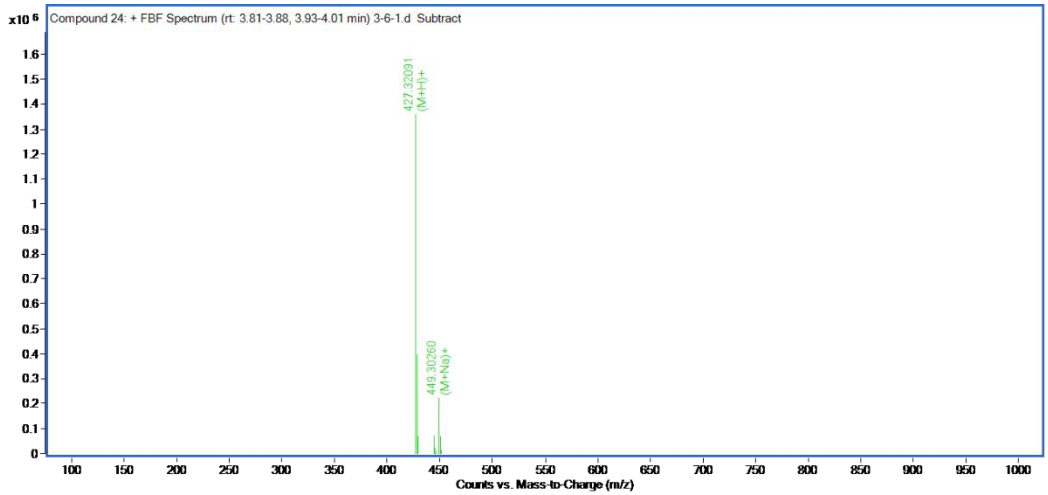

Figure S47. HRESIMS spectrum of compound **15**.

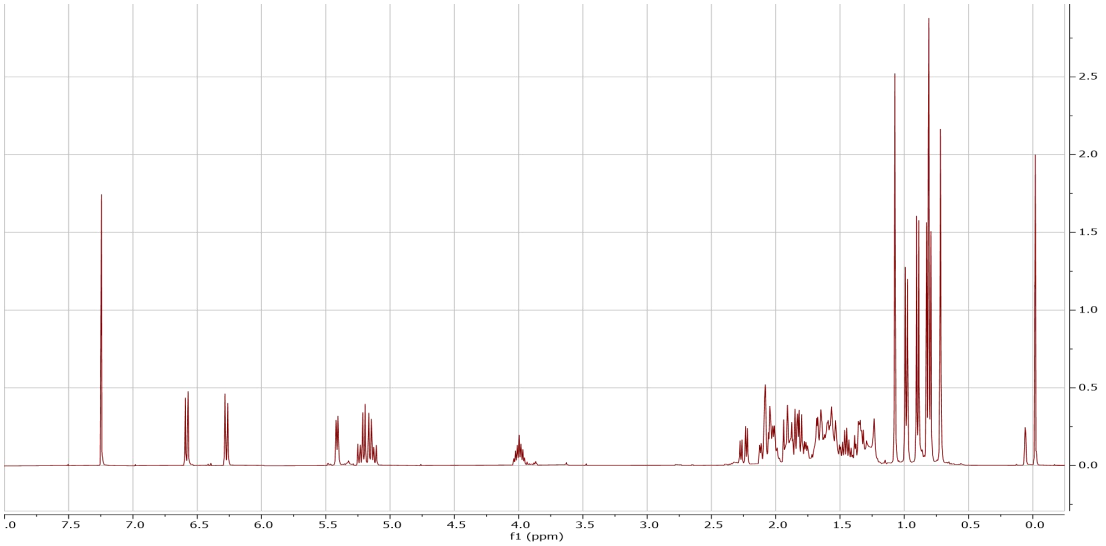

Figure S48. ^{1}H NMR spectrum (400 MHz) of compound **15** in $CDCl_3$.

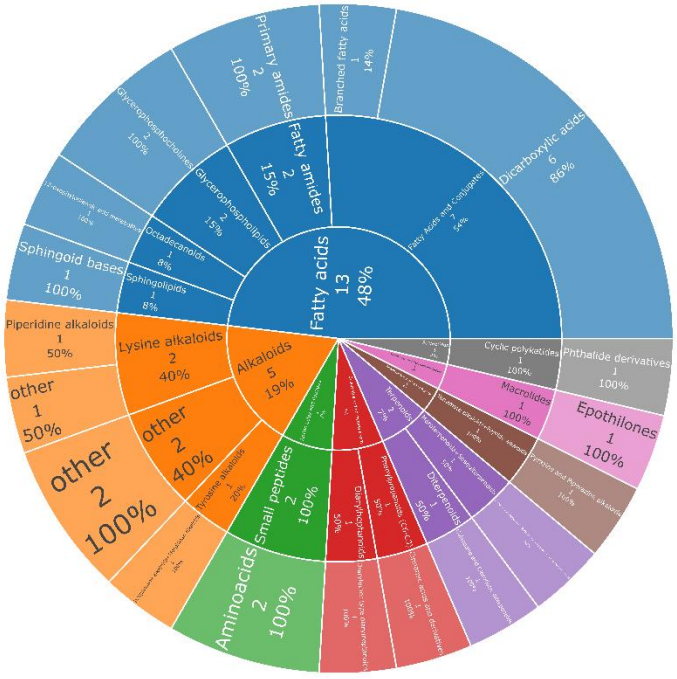

Figure S49. The proportion of HEDE marked peaks in various chemical classifications.

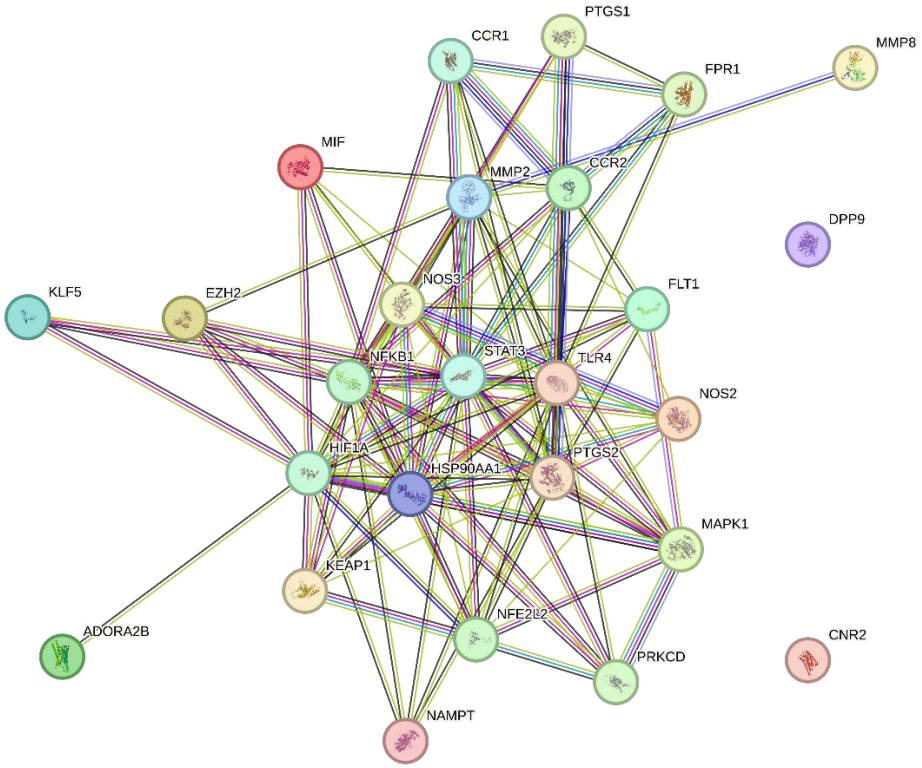

Figure S50. PPI analysis by STRING.